STUDYING LIQUID-PHASE HETEROGENEOUS CATALYSIS USING THE ATOMIC FORCE MICROSCOPE

by

MATTHEW J. YOUNG

B.S., Mississippi State University, 2011

AN ABSTRACT OF A DISSERTATION

submitted in partial fulfillment of the requirements for the degree

DOCTOR OF PHILOSOPHY

Department of Chemical Engineering
College of Engineering

KANSAS STATE UNIVERSITY
Manhattan, Kansas

2016

Abstract

Characterization of the interactions of hydrogen with catalytic metal surfaces and the mass transfer processes involved in heterogeneous catalysis are important for catalyst development. Although a range of technologies for studying catalytic surfaces exists, much of it relies on high-vacuum conditions that preclude in-situ research. In contrast, atomic force microscopy (AFM) provides an opportunity for direct observation of surfaces under or near actual reaction conditions. Tapping-mode AFM was explored here because it expands AFM beyond the usual topographic information toward speciation and other more subtle surface information. This work describes using phase-angle data from tapping-mode AFM to follow the interactions of hydrogen with palladium. Both gas-solid and liquid-solid interfaces were studied. Real-time AFM phase-angle data allowed for the observation of multiphase mass transfer to and from the surface of palladium at atmospheric pressure and room temperature without the need for complex sample preparation. The AFM observations were quantitatively benchmarked against and confirm mass transfer predictions based on bulk hydrogen diffusion estimates. Additionally, they support recent studies that demonstrate the existence of multiple hydrogen states during interactions with palladium surfaces.

STUDYING LIQUID-PHASE HETEROGENEOUS CATALYSIS USING THE ATOMIC FORCE MICROSCOPE

by

MATTHEW J. YOUNG

B.S., Mississippi State University, 2011

A DISSERTATION

submitted in partial fulfillment of the requirements for the degree

DOCTOR OF PHILOSOPHY

Department of Chemical Engineering
College of Engineering

KANSAS STATE UNIVERSITY
Manhattan, Kansas

2016

Approved by:

Major Professor
Dr. Peter H. Pfromm

Copyright

Abstract

Characterization of the interactions of hydrogen with catalytic metal surfaces and the mass transfer processes involved in heterogeneous catalysis are important for catalyst development. Although a range of technologies for studying catalytic surfaces exists, much of it relies on high-vacuum conditions that preclude in-situ research. In contrast, atomic force microscopy (AFM) provides an opportunity for direct observation of surfaces under or near actual reaction conditions. Tapping-mode AFM was explored here because it expands AFM beyond the usual topographic information toward speciation and other more subtle surface information. This work describes using phase-angle information from tapping-mode AFM to follow the interactions of hydrogen with palladium. Real-time AFM phase-angle information allowed for the observation of multiphase mass transfer to and from the surface of palladium at atmospheric pressure and room temperature without the need for complex sample preparation. The AFM observations were quantitatively benchmarked against and confirm mass transfer predictions based on bulk hydrogen diffusion estimates. Additionally, they support recent studies that demonstrate the existence of multiple hydrogen states during interactions with palladium surfaces.

Table of Contents

List of Figures

List of Tables

Acknowledgements

My deepest gratitude must be given to my Ph.D. advisor, Dr. Peter Pfromm, who has been very patient and encouraging throughout my studies. He has served as a model of scientific curiosity and personal fortitude. The many discussions we had during my time at Kansas State University were invaluable contributions to my research and to my personal development.

I would also like to thank my committee members. Dr. Mary Rezac provided constructive critiques of my presentations and publications as well as guidance on a number of topics. Dr. Bruce Law was especially generous in allowing the use of his laboratory and equipment and helpful in initiating the research. Dr. Keith Hohn and Dr. Christer Aakeröy were most gracious to serve on my committee and their contributions are greatly appreciated.

I also thank current and former members of the Rezac and Pfromm research group: Michael Heidlage, Yixiao Li, Jared Carson, Leslie Schulte, John Stanford, Michael Wales, Liz Boyer, Fan Zhang, Ronald Michalsky, Sebastian Wendel, and Alexandru Avram. All of them were great sources of friendship and support.

Special thanks must be given to the current and former staff members in the Department of Chemical Engineering for all their work that supported this research: Danita Deters, Karen Strathman, Debi Wahl, Dave Threewit, Cynthia Brott, Karey DeBardeleben, Pat Nelson, Florence Sperman, and Lauren Muse.

The love and encouragement of my parents, my brother Andrew, and my sister-in-law Cristel helped me throughout my education. In addition, I thank Nicole Cook for her enduring friendship, which has been a source of inspiration and encouragement.

This material is based upon work supported by National Science Foundation Grant: From Crops to Commuting: Integrating the Social, Technological, and Agricultural Aspects of Renewable and Sustainable Biorefining (I-STAR); NSF Award No.: DGE-0903701 and the National Institute of Food and Agriculture, U.S. Department of Agriculture, under Agreement No. 2011-67009-20055.

Dedication

To Mom, Dad, Andrew, Cristel, Ava, Keegan, and Isaac for their love and support.

1 Introduction

1.1 Research Motivation

More than 80% of all synthetic chemicals are produced using catalysis. Interactions of hydrogen with catalytic metal surfaces during heterogeneous catalysis are of great interest for a number of important processes including petrochemical processing, soybean oil hydrogenation,[1] pharmaceutical production,[2] fine chemical production,[2] and conversion of biomass to fuels and chemicals.[3] Adsorption of hydrogen on solid (metal) surfaces is the necessary first step for heterogeneous hydrogenation catalysis.[4-6] Of particular interest is therefore the availability of hydrogen on catalytic surfaces because it impacts productivity and selectivity.[1] Direct, real-time observation of the dynamic appearance and disappearance of hydrogen on the surface of a common catalytic material such as palladium (Pd) at ambient pressure either at a gas-solid or liquid-solid interface appears absent from the literature.

The efficiency of heterogeneous catalysis is constrained by mass-transfer limitations based on the limited solubility of gases like hydrogen in liquids. This leads to low conversion rates, undesirable product distribution, or even highly detrimental byproducts like coke.[7,8] Catalytic membrane reactors have been shown to improve reactor performance by allowing delivery of a gaseous reactant directly to the catalyst surface, avoiding hydrogen starvation of the catalyst surface.[1,9] Studies of catalytic membrane reactors have been conducted based on overall analysis of products and reactants, but the in-situ study of the catalytic surface at nanometer scale resolution as hydrogen is added and/or depleted was not possible due to the difficulty of probing liquid/solid interfaces.[10-11]

Despite being so commonly used in large-scale chemical processes and so thoroughly studied, the primary method of studying heterogeneous catalytic systems is mostly phenomenological.[12] This is due to the limitations of analytical technology to study liquid/solid interfaces at conditions near those often used for chemical reactions including temperatures above 100 °C and pressures of multiple atmospheres. Interest in in-situ and in-operando approaches to studying heterogeneous catalysis has increased with the sophistication of microscopy and spectroscopy techniques. Atomic force microscopy (AFM) allows for the study of surfaces at non-ideal conditions and under liquid without the need for extreme sample

preparation procedures. Furthermore, it has been demonstrated that AFM can be used to study surfaces of heterogeneous composition and differentiate between materials using the phase angle of the cantilever probe.[13-25] In this dissertation, the application of phase angle in AFM is investigated as a way to study the presence or absence of adsorbed hydrogen on a Pd surface dynamically.

1.2 Objectives of Research

1. Demonstrate the usefulness of phase-angle AFM (PA-AFM) for dynamic observation of hydrogen adsorption and desorption on Pd as a representative catalytic surface both at gas-solid and liquid-solid interfaces.

2. Record changes in phase angle observed in PA-AFM experiments following changes in applied gas species and compare to expected calculated hydrogen concentrations based on diffusion processes.

3. Link changes in phase angle to expected changes in the material properties of the Pd surface as hydrogen activity changes with time.

1.3 Outline of Dissertation

This dissertation is composed of chapters that present experimental results and discussions from scientific papers either published in peer-reviewed literature or are in preparation for publication. With the exception of introductory passages, those papers are reproduced with minor modifications as the relevant chapters. The details of the chapters are listed below.

Chapter 2 gives a description of AFM theory and practice as it relates to the hardware and software used in the present research. In particular, PA-AFM is discussed at length.

Chapter 3 is a published paper (with minor modifications) that reports the results of PA-AFM experiments with Pd-sputtered polycarbonate films exposed to hydrogen or nitrogen. Changes in the phase angle of the probe after switching from flowing hydrogen to flowing nitrogen were compared to expected changes in the availability of adsorbed hydrogen as predicted by Fickian diffusion of hydrogen through the Pd film.

Chapter 4 describes PA-AFM experiments with Pd-sputtered polycarbonate films with nitrogen or hydrogen supplied to a solid-liquid interface by diffusion through the solid.

Chapter 5 reports the results of PA-AFM experiments with Pd-sputtered polycarbonate films with nitrogen or hydrogen pressurized or flowing underneath a water-immersed sample. The scanning conditions used were different from those reported in Chapter 4.

Chapter 6 gives a series of recommendations for improvements and suggests future work to further the use of AFM for studying catalytic systems.

Chapter 7 presents the conclusions.

1.4 References

[1] Singh, D.; Rezac, M. E.; Pfromm, P. H. Partial Hydrogenation of Soybean Oil using Metal Decorated Integral-asymmetric Polymer Membranes: Effects of Morphology and Membrane Properties. *J. Membr. Sci.* **2010**, *348*, 99-108.

[2] Singh, U. K. ; Vannice, M. A. Kinetics of Liquid-phase Hydrogenation Reactions over Supported Metal Catalysts - A Review. *Appl. Catal., A* **2001**, *213*, 1-24.

[3] Zacher, A. H.; Olarte, M. V.; Santosa, D. M.; Elliott, D. C.; Jones, S. B. A Review and Perspective of Recent Bio-oil Hydrotreating Research. *Green Chem.* **2014**, *16*, 491-515.

[4] Mitsui, T.; Rose, M. K.; Fomin, E.; Ogletree, D. F.; Salmeron, M. Dissociative Hydrogen Adsorption on Palladium Requires Aggregates of Three or More Vacancies. *Nature* **2003**, *422*, 705-707.

[5] Wunder, R. W.; Cobes, J. W.; Phillips, J.; Radovic, L. R.; Lopez Peinado, A. J. Carrasco-Marin, F. Microcalorimetric Study of the Absorption of Hydrogen by Palladium Powders and Carbon-supported Palladium Particles. *Langmuir* **1993**, *9*, 984-992.

[6] Johnstone, R. A. W.; Wilby, A. H. Heterogeneous Catalytic Transfer Hydrogenation and Its Relation to Other Methods for Reduction of Organic Compounds. *Chem. Rev.* **1985**, *85*, 129-170.

[7] Guettel, R.; Kunz, U.; Turek, T. Reactors for Fischer-Tropsch synthesis. *Chem. Eng. Technol.* **2008**, *31*, 746–754.

[8] Veldsink, J. W. B.; Schoon, M. J.; Beenackers, N. H.; Antonie, A. C. M. Heterogeneous hydrogenation of vegetable oils: a literature review. *Catal. Rev. Sci. Eng.* **1997**, *39*:253–318.

[9] Singh, D.; Pfromm, P. H.; Rezac, M. E. Overcoming Mass-Transfer Limitations in Partial Hydrogenation of Soybean Oil Using Metal-Decorated Polymeric Membranes. *AIChE J.* **2011**, *57* (9), 2450-2457.

[10] Zaera, F. Probing Liquid/Solid Interfaces at the Molecular Level. *Chem. Rev.* **2012**, *112*, 2920-2986.

[11] Roobol, S. B.; Cañas-Ventura, M. E.; Bergman, M.; van Spronsen, M. A.; Onderwaater, W. G.; van der Tuijn, P. C.; Koehler, R.; Ofitserov, A.; van Baarle, G. J. C.; Frenken, J. W.

M. The ReactorAFM: Non-contact atomic force microscope operating under high-pressure and high-temperature catalytic conditions. *Rev. Sci. Instrum.* **2015**, *86*, 033706.

[12] Dudukovic, M. P.; Reaction engineering: Status and future challenges. *Chem. Eng. Sci.* **2010**, *65*, 3-11.

[13] James, P. J.; Antognozzi, M.; Tamayo, J.; McMaster, T. J.; Newton, J. M.; Miles, M. J. Interpretation of Contrast in Tapping Mode AFM and Shear Force Microscopy. A Study of Nafion. *Langmuir* **2001**, *17*, 349-360.

[14] Mclean, R. S.; Sauer, B. B. Tapping-Mode AFM Studies Using Phase Detection for Resolution of Nanophases in Segmented Polyurethanes and Other Block Copolymers. *Macromolecules* **1997**, *30*, 8314-8317.

[15] Magonov, S. N.; Elings, V.; Whangbo, M.-H. Phase Imaging and Stiffness in Tapping-mode Atomic Force Microscopy. *Surf. Sci.* **1997**, *375*, L385-L391.

[16] Schmitz, I.; Schreiner, M.; Friedbacher, G.; Grasserbauer, M. Phase Imaging as an Extension to Tapping Mode AFM for the Identification of Material Properties on Humidity-sensitive Surfaces. *Appl. Surf. Sci.* **1997**, *115*, 190-198.

[17] Bhushan, B.; Qi, J. Phase Contrast Imaging of Nanocomposites and Molecularly Thick Lubricant Films in Fagnetic Media. *Nanotechnology* **2003**, *14*, 886-895.

[18] Xu, Z. W.; Liang, Y. C.; Dong, S.; Cao, Y. Z.; Zhao, T. Q.; Wang, J. H.; Zhao, Q. L. Phase Contrast Imaging of SEBS Triblockcopolymer Studied by Carbon Nanotubes Probe. *Ultramicroscopy* **2005**, *105*, 72-78.

[19] Tamayo, J.; García, R. Relationship between Phase Shift and Energy Dissipation in Tapping-mode Scanning Force Microscopy. *Appl. Phys. Lett.* **1998**, *73*, 2926-2928.

[20] Behrend, O. P.; Odoni, L.; Loubet, J. L.; Burnham, N. A.; Phase imaging: Deep or superficial? *App. Phys. Lett.* **1999**, *75*, 2551-2553.

[21] Bar, G.; Thomann, Y.; Brandsch, R.; Cantow, H.-J.; Whangbo, H.-H.; Factors Affecting the height and Phase Images in Tapping Mode Atomic Force Microscopy. Study of Phase-Separated Polymer Blends of Poly(ethene-co-styrene) and Poly(2,6-dimethyl-1,4-phenylene oxide). *Langmuir* **1997**, *13*, 3807-3812.

[22] Martínez, N. F.; García, R. Measuring Phase Shifts and Energy Dissipation with Amplitude Modulation Atomic Force Microscopy. *Nanotechnology* **2006**, *17*, S167-S172.

[23] Zhao, Y.; Cheng, Q.; Qian, M.; Cantrell, J. H.;Phase image contrast mechanism in intermittent contact atomic force. *J. Appl. Phys.* **2010**, *108*, 094311.

[24] Melcher, J.; Carrasco, C.; Xu, X.; Carrascosa, J. L.; Gómez-Herrero, J.; de Pablo, P. J.; Raman, A.; Origins of phase contrast in the atomic force microscope in liquids. *P. Natl. Acad. Sci. USA* **2009**, *106* (33), 13655-13660.

[25] Payam, A. F.; Ramos, J. R.; Garcia, R.; Molecular and Nanoscale Compositional Contrast of Soft Matter in Liquid: Interplay between Elastic and Dissipative Interactions. *ACS Nano* **2012**, *6* (6), 4663-4670.

2 Background

2.1 Introduction to Atomic Force Microscopy

2.1.1 General Introduction to Atomic Force Microscopy

The atomic force microscope was conceived as a combination of two earlier scientific instruments: the scanning tunneling microscope (STM) and the stylus profilometer.[1] The intention was to produce a new instrument capable of non-destructive imaging of surfaces with atomic-scale resolution. Although the modern AFM has been expanded to a wide range of capabilities and imaging modes, the components of all AFMs are similar. These include a cantilever probe with a microfabricated tip, an x/y-position-controlled piezo scanner, a probe holder attached to a z-position-controlled piezo scanner, and a tip deflection detector. The sample is moved under the stationary probe in a raster pattern over a plane of a user-determined size. Topography data is collected by monitoring the motion of the cantilever tip as the probe moves across the sample surface.[2] Many systems, including the MFP-3D by Asylum Research used for this work, utilize a focused laser beam to monitor vertical movement of the tip.[3] The laser beam focuses on the center of the cantilever's mirror-finished back and is then deflected to a position-sensitive photodetector (Figure 2.1).

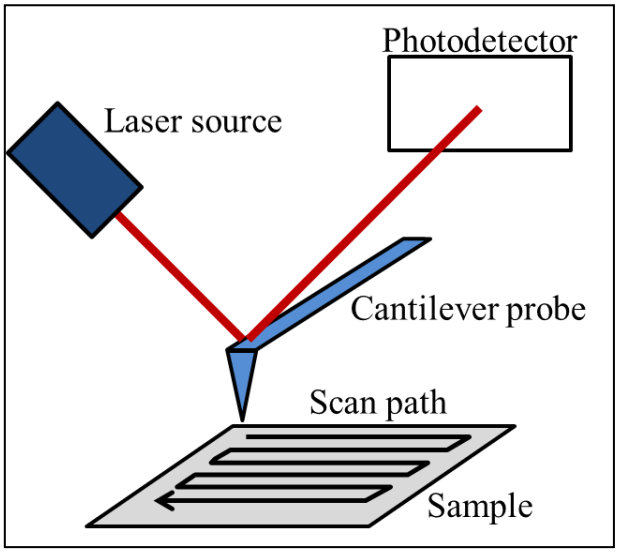

Figure 2.1 - Tracking of the AFM cantilever probe using laser-beam-deflection detection.

With the MFP-3D, the scan path is determined by a number of user-determined factors. These include size, rate, number of points, and number of lines. Image resolution is determined by size, number of points, and number of lines. The time required to perform a complete scan of the sample area is determined by the rate and number of lines. The scan size is entered as a single number from 100 nm to 90 μm and defines both the length and width of the scan area. . Scan rate determines the time required to scan one line across the sample and can range from 0.10 to 3.00 Hz. The number of points specifies the data points recorded per each line of scanning. The number of lines is how man lines constitute a scan image. The number of points and lines are required to be multiples of 32, but the manufacturer recommends that they be powers of two. Also, it is recommended that the numbers of points and lines be equal so that the images produced are grids of equally spaced data points.

Although the traditional AFM imaging mode only allowed for topography studies, modern AFM has expanded to acquire data via contact mode, alternating current (AC) mode, dual AC mode, non-contact mode, frictional force mode, piezo-response force microscopy, electric force microscopy, and magnetic force microscopy.[4] One factor in choosing an imaging mode is the nature of the sample. Unlike a number of high-resolution microscopy and spectroscopy techniques, AFM can be performed without vacuum and with only rudimentary sample preparation.[4] Tapping-mode AFM (TM-AFM) is particularly useful for producing high-resolution images of samples.[5]

In TM-AFM (also called AC mode, intermittent contact, or amplitude modulation AFM) the probe is oscillated at or near its resonant frequency (usually in the range of 50 to 350 kHz) and lightly contacts the scanned surface.[4] For electrically neutral, non-magnetic samples such as those used for this dissertation, TM-AFM is sensitive to stronger attractive forces than true non-contact mode, but not to the repulsive tip-surface forces measured in contact-mode imaging.[3,4] Additionally, TM-AFM causes reduced lateral forces on the sample compared to contact mode.[3] Getting high-quality images in TM-AFM requires finding the resonant frequency at which the cantilever is most responsive to excitation.[3] Modern AFM instruments include software with capabilities that simplify this process.

The principles for cantilever tuning are similar for probes in air and in liquid, but there are differences between the processes used. For probes in air, the MFP-3D uses an automatic tuning

procedure to determine the optimal drive amplitude and the resonant frequency. For probes in liquid, the resonant frequency of the undamped cantilever must first be determined. Afterwards, the resonant frequency of the fluid-damped cantilever is chosen based on which frequency peak is closest to the undamped frequency.

The lateral spatial resolution of an AFM is determined by the geometry of the probe tip.[6] In the experiments described in this dissertation, the probes had nominal tip sizes of 9 ± 2 nm (manufacturer's data). Therefore, the smallest possible distance between discernable features on AFM images was expected to be about 9 nm. Every scan performed had dimensions of 1.00×10^3 nm × 1.00×10^3 nm, therefore identifying a distance of 9 nm between features proved difficult. However, as shown in Figure 2.2, a 20-nm distance between two distinct Pd clusters is easily distinguishable. The z-axis resolution of an AFM is determined by the instrument noise and is typically within a sub-nm range.[7] In Figure 2.2, the root-mean-square (*RMS*) roughness (R_{RMS}) of the polyetherimide (PEI, Ultem-1000 purchased from General Electric (Huntersville, NC).) surface that was sputtered with Pd to produce a deliberately imperfect metal layer (Figure 2.2a) was 5.737 nm while the R_{RMS} of the polycarbonate film that was sputtered with Pd (Figure 2.2b) to produce a continuous metal layer was 2.913 nm. For comparison, the R_{RMS} of (001)-oriented Si has been reported as 0.07 nm.[8]

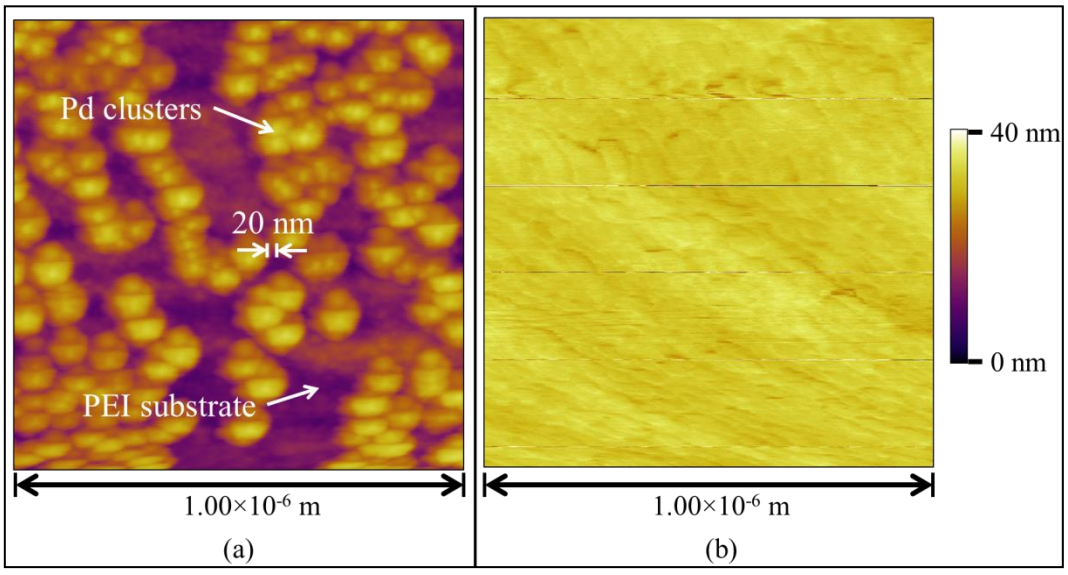

Figure 2.2 - Topography images of Pd sputtered surfaces. a) A PEI film sputtered with Pd for 9 s to produce a deliberately imperfect metal layer showing an estimated spatial resolution of 20 nm. The lightly shaded portions are Pd clusters of about 32 million Pd atoms (Pd clusters are about

150 nm in radius and about 20 nm tall and Pd's atomic radius is 0.137 nm; PC has an average chain *RMS* end-to-end length of about 70 nm[9]). b) A PC film sputtered with Pd for 45 s (standard preparation of Pd samples for phase angle measurements). The surface appears flat and uniform.

Figure 2.2b demonstrates that the standard sample preparation method used in this work produced a continuous uniform Pd surface as supported by the R_{RMS} values and the substantial literature on sputtering of metals on polymer films.[10,11]

The Asylum MFP-3D simultaneously collects four sets of data during scans: sample topography, probe oscillation amplitude, probe oscillation phase angle, and the distance between the probe cantilever and the sample (Z-sensor) (Figure 2.3).[12] These four data sets are stored as a single file for each scan of the sample area, but they can be accessed individually. Proprietary software produced by Asylum Research allows for these data files to be viewed and analyzed, but only as individual scans. This reflects the prevalent usage of AFM as an instrument for static studies of sample topography. Therefore, a method of sequentially linking the results of multiple scans over the same area over time was needed.

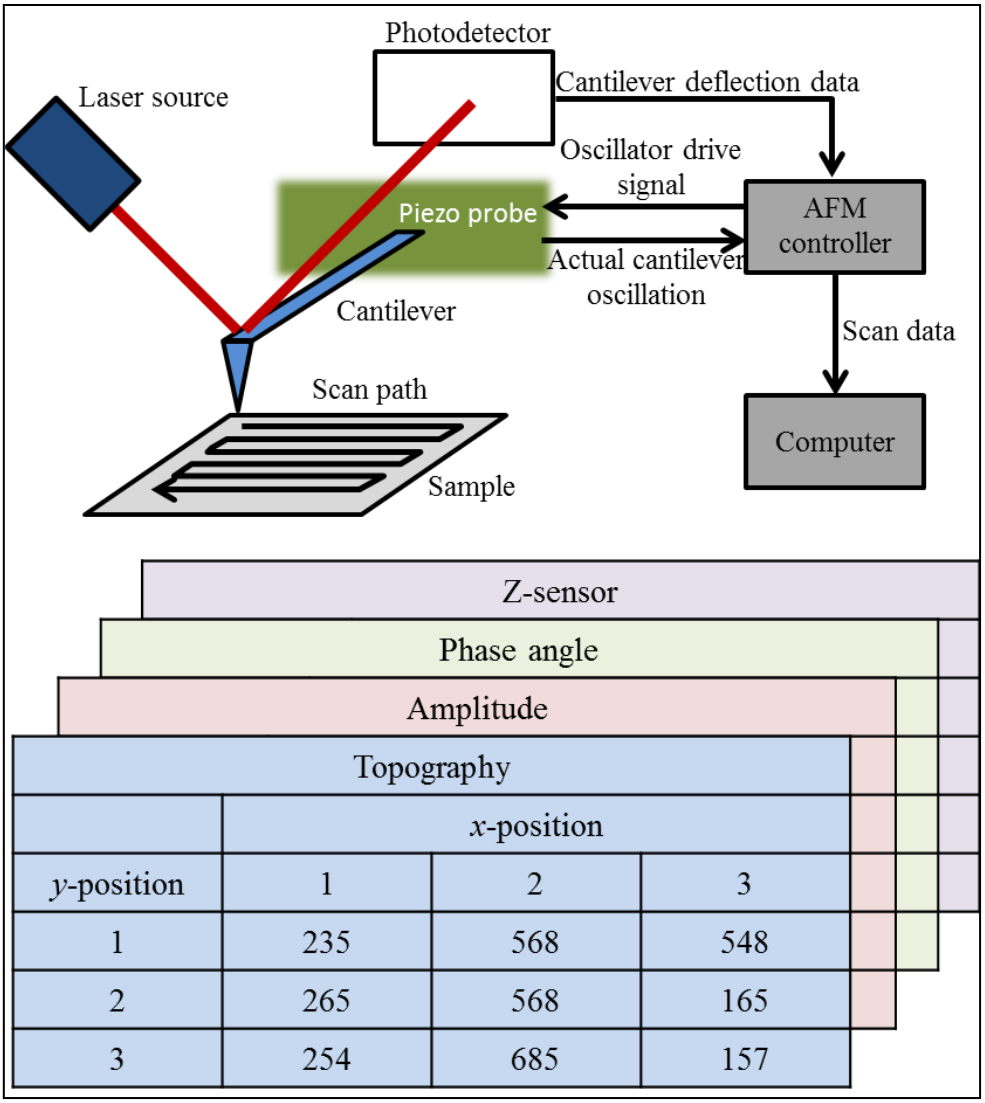

	x-position		
y-position	1	2	3
1	235	568	548
2	265	568	165
3	254	685	157

Figure 2.3 - Data collection by the AFM and resulting data sets.

If it is assumed that the scanned area is homogeneous (also see the discussion of Figure 2.5), then the phase angle can be considered only as a function of time and is independent of the probe's precise position (Figure 2.4). Each line of data points was averaged and treated as a single new data point. Each of these line-averaged data points can then be plotted against time. The phase angle vs. time plot shown in Figure 2.4 was chosen to represent phase-angle data for most of the experimentation discussed below.

Time and position	Topography	Amplitude	Phase angle	Z-sensor
Time = 0, (x,y) = (1,1)	123	158	845	845
Time = 1, (x,y) = (1,2)	241	534	548	125
Time = 2, (x,y) = (2,2)	235	568	548	456
Time = 3, (x,y) = (2,1)	265	568	165	156

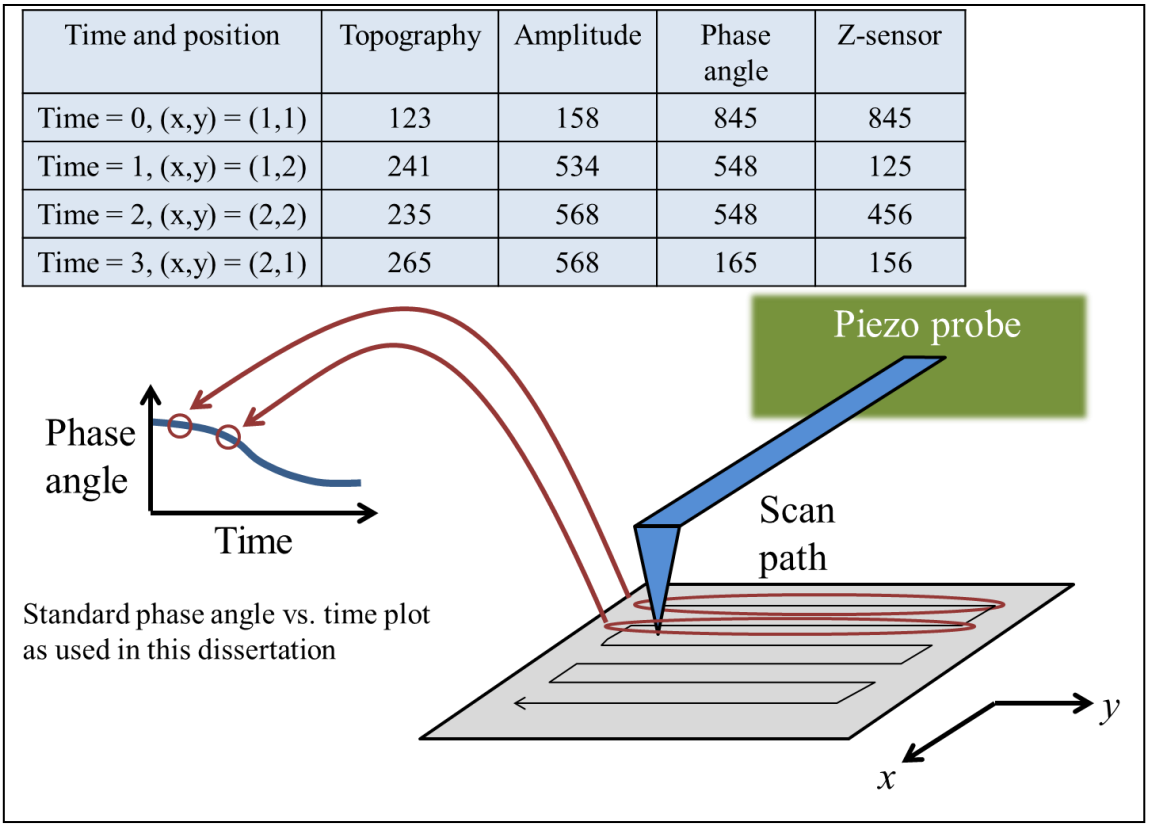

Figure 2.4 - Data acquisition by AFM and processing used to produce a phase angle vs. time plot from the same data.

Topography scans of the substrate PC and Pd-sputtered PC are shown in Figure 2.5 to demonstrate the homogeneity of the surface assumed above.

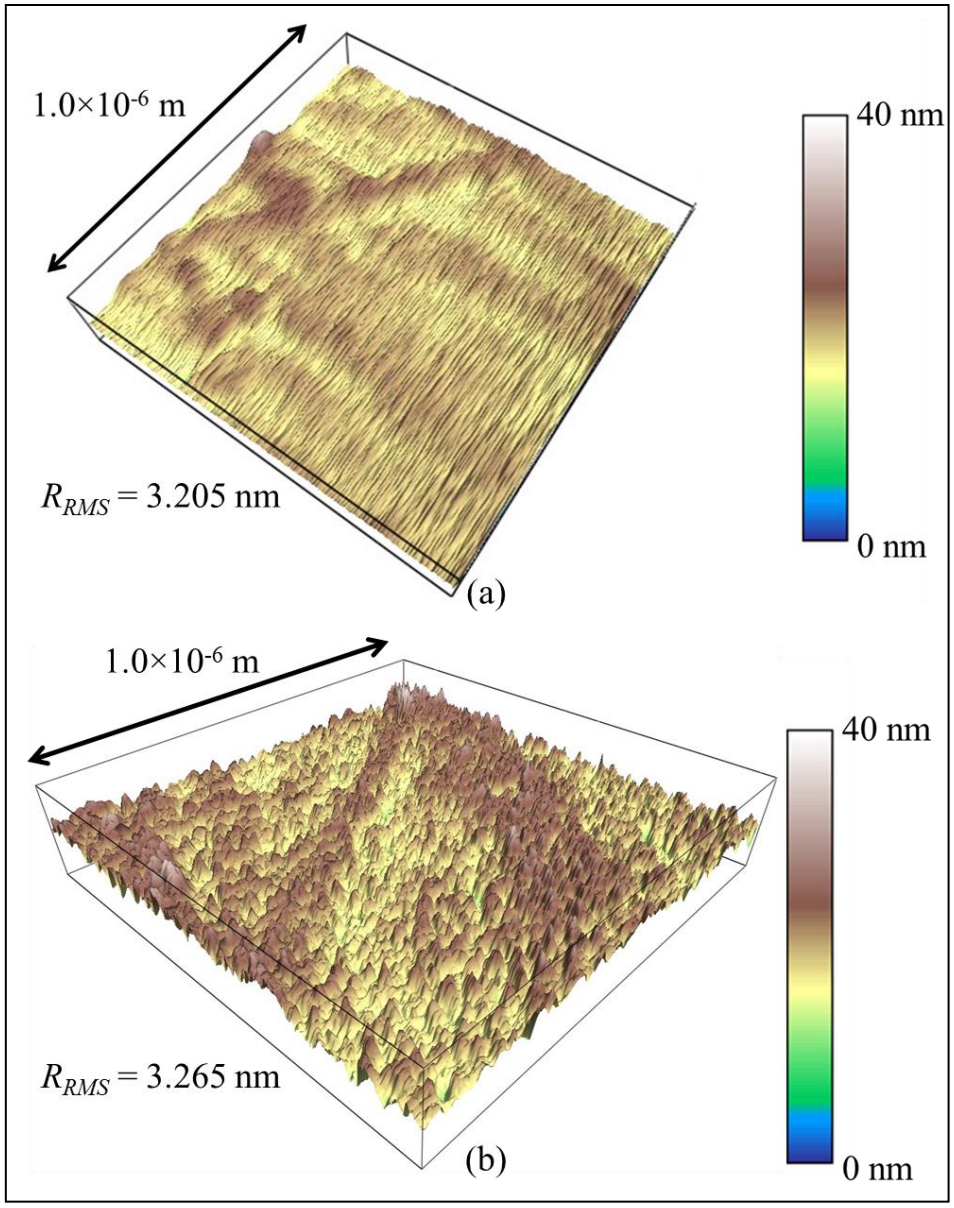

Figure 2.5 - Topography scans acquired by tapping-mode AFM of (a) unmodified PC and (b) Pd-sputtered PC (standard sputtering procedure, see subchapter 3.2).

Note that in Figure 2.5, the scale of the y-axis is large compared to Pd's atomic radius of 0.134 nm. The R_{RMS} of the extruded PC film scanned for Figure 2.5a was 3.205 nm. The R_{RMS} of the Pd-sputtered PC film in Figure 2.5b was 3.265 nm. The sputtering process did produce a slightly rougher surface than the unmodified PC film, but the Pd surface was still, on average, quite featureless. This is especially apparent when compared to the roughness of the sputtered PEI film in Figure 2.2a (R_{RMS} = 5.737 nm) reflecting its imperfect metal layer with significant

areas of exposed polymer. Therefore, for the unmodified and heavily sputtered polymer film samples used in this work, the assumption of surface homogeneity of the scan area appears reasonable.

2.1.2 Phase-angle Atomic Force Microscopy

2.1.2.1 At the Gas-solid Interface

Topography data are the primary focus of tapping-mode AFM, but cantilever phase-angle data (Figure 2.6) can be used to reveal further details about a sample.[13] Although phase-angle AFM was originally investigated as a qualitative approach to surface analysis (particularly for the biological sciences), there is also interest in its use for quantitative measurements.[3] Much research has been performed to determine the cause of phase-angle contrast in AFM.[14-16] A generally accepted theory is that the phase angle is related to changes in energy dissipation interactions between the probe and sample.[13,17,18] This can be considered qualitatively as the energy supplied to the probe's piezo element would be completely transmitted to the sample if the tip of the cantilever was to "stick" to the sample and rendered unable to oscillate further. In contrast, a perfectly elastic interaction between the tip and the sample would result in no loss in the energy of the cantilever.

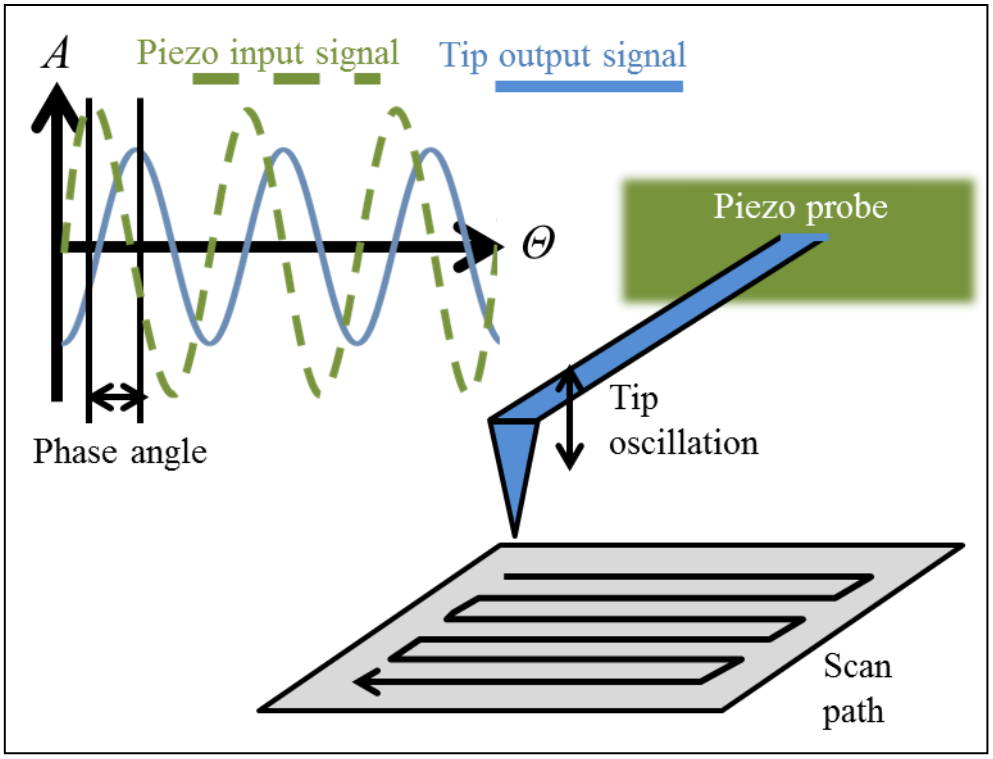

Figure 2.6 - The principle of phase angle in AFM cantilever oscillation.

Tamayo and García[19] proposed a model for the energy dissipated per cantilever oscillation:

$$E_{dis} = E_{ext} - E_{med} = \frac{\pi k A_t A_0 \sin(\varphi)}{Q} - \frac{\pi k A_t^2 \omega_t}{Q \omega_0} \qquad \text{Equation 2.1}$$

This equation expresses the energy dissipated by tip-sample interaction E_{dis} [eV] as the difference between the energy supplied externally to the probe E_{ext} [eV] and the hydrodynamic effects of the immersion medium around the cantilever E_{med} [eV]. Thus, for a cantilever probe with spring constant k [N/m], tapping amplitude A_t [nm], free amplitude A_0 [nm], driving frequency ω_t [kHz], natural resonance frequency ω_0 [kHz], quality factor Q, and phase angle φ [°], the energy dissipated can be easily calculated. According to this equation, energy input from the oscillator (E_{ext}) is dissipated either through the sample surface (E_{dis}) or through immersion medium around the probe (E_{med}).

The difference in dissipated energy between two different regions of an AFM scan can be also be calculated:

$$\Delta E_{dis} = E_{dis,2} - E_{dis,1} = \left(\frac{\pi k A_t A_0 \sin(\varphi)}{Q} - \frac{\pi k A_t^2 \omega_t}{Q \omega_0} \right)_2 - \left(\frac{\pi k A_t A_0 \sin(\varphi)}{Q} - \frac{\pi k A_t^2 \omega_t}{Q \omega_0} \right)_1$$

Equation 2.2

In tapping-mode AFM, ω_0, ω_t, A_0, and A_t remain constant for the duration of a scan. This allows Equation 2.2 to be simplified:

$$\Delta E_{dis} = \frac{\pi k A_t A_0}{Q} (\sin(\varphi_2) - \sin(\varphi_1))$$

Equation 2.3

This model originated from a study that compared the phase angles of deposited "Purple Membrane" (the crystalline form of the protein Bacteriorhodopsin) to those of the highly oriented pyrolytic graphite (HOPG) substrate.[19] As a reference, Tamayo and Garcia measured the force exerted between an AFM tip and each material by contacting the tip with the sample and subsequently retracting it. The resulting difference in the force curves between loading and unloading was interpreted as the energy dissipated by each material. The energy dispersion determined by force measurements compared favorably with those obtained from calculations using phase angle for each material. Furthermore, the phase angle over HOPG was always lower than that observed for Purple Membrane. Thus, it was concluded that stiffer materials exhibit larger AFM phase angles.

Similar results were obtained in a study of mica and polystyrene samples in the gas phase.[20] Once again, the stiffer material (mica) showed larger phase angles compared to the more compliant sample (polystyrene). The authors also discussed tip-sample separation distances as a factor in phase-angle results.

Phase-angle AFM has even been used to differentiate between two material phases of a polymer blend.[21] Here, blends of poly(ethene-co-styrene) (PES) and poly(2,6-dimethyl-1,4-phenylene oxide) (PPO) were studied. Again, it was concluded that the stiffer material (PPO) showed higher phase angles than the more compliant material (PES). In summary, it can be concluded from past gas-phase studies that phase angles are larger for stiffer materials (Figure 2.7). The results for Pd-sputtered PC films exposed to and then depleted of hydrogen shown in Chapter 3 are within expectations based on this observation.

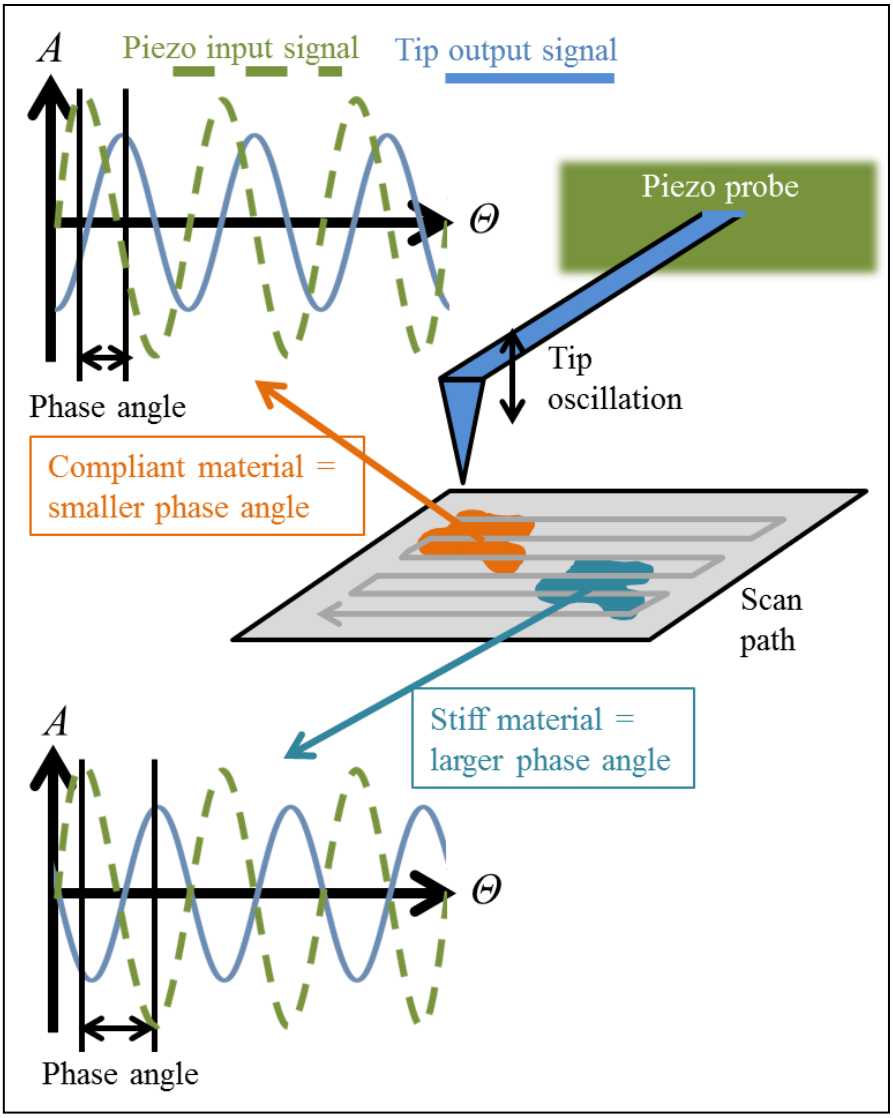

Figure 2.7 - The general behavior of AFM phase-angle data obtained for different material types in air.[19-21]

A more desirable interpretation of AFM phase-angle data is one that directly links phase angle to material properties. This approach was elusive due to the number of factors that affect phase angle including the ratio between probe excitation and resonance frequencies, sample elastic properties, the tip's radius, sample-tip friction, cantilever tilt angle, and various morphological and compositional contributions.[22] However, it has been found that phase angle shifts can be related to Young's modulus and Poisson's ratio for the tip and sample materials.[23] The Young's modulus (also known as the elastic modulus) of a material is the ratio of its tensile stress to its tensile strain due to elastic deformation. The Poisson's ratio is the negative of the

ratio of a material's transverse strain to its axial strain. This model was developed based on a collision between a tip of known radius *R* and the sample.

$$\Delta\Omega = (\varphi)_2 - (\varphi)_1 = \pi T\left[\left(\frac{1}{2t_0 + t_1}\right)_2 - \left(\frac{1}{2t_0 + t_1}\right)_1\right] \qquad \text{Equation 2.4}$$

Here, $\Delta\Omega$ is defined as the difference in phase angle between different points on a sample. T [ns] is the free-space oscillation period of the cantilever, t_0 [ns] is the time required for one complete free-space oscillation of the cantilever, and t_1 [ns] is the time required for the cantilever to move from the fully deflected position to maximum impact with the sample (also called the collision half-time). T and t_0 are calculated from values determined during the cantilever tuning process.

$$T = \frac{1}{\omega_0} \qquad \text{Equation 2.5}$$

$$t_0 = \frac{1}{\omega_0}\arcsin\left(\frac{z_0}{A_0}\right) \qquad \text{Equation 2.6}$$

z_0 [nm] is the distance between the tip of the non-deflected cantilever and the sample. This is determined from the ratio between set-point amplitude and the driving amplitude of the cantilever. The collision half-time, t_1, can be calculated using a number of experimental and calculated parameters for the system.[23]

$$t_1 = \int_0^{\delta_1}\left\{V_0^2 - 2\omega_t^2 z_0\delta - \omega^2\delta^2 + \frac{HR}{3m_c}\left[\frac{1}{a_0} - \frac{1}{(z_0 - z_c)}\right] + \frac{HR}{3m_c a_0^2}(\delta - z_0 + a_0 + z_c)\right.$$
$$\left. - \frac{16E^*\sqrt{R}}{15m_c}(\delta - z_0 + a_0 + z_c)^{5/2}\right\}^{-(1/2)} d\delta \qquad \text{Equation 2.7}$$

where V_0 [μm/s] is the initial tip-sample collision velocity, δ [nm] is the instantaneous penetration depth of the tip into the sample, δ_1 [nm] is the maximum penetration depth, a_0 [Å] is the van der Waal's radius, H is the Hamaker constant, R [nm] is the tip radius, m_c [kg] is the mass of the cantilever, and z_c [nm] is the tip-sample separation distance at which a strong

interaction force is encountered. Most importantly, E^* [Pa] is the reduced Young's modulus, which is derived from the Young's moduli and Poisson's ratios of the tip and sample.

$$\left(E^*\right)^{-1} = \left[\frac{\left(1-\upsilon_S^2\right)}{E_S} + \frac{\left(1-\upsilon_T^2\right)}{E_T}\right] \qquad \text{Equation 2.8}$$

Here, E [Pa] is the Young's modulus and υ is the Poisson's ratio with the subscripts S and T referring to the sample and tip, respectively. To calculate t_1, the initial tip-sample collision velocity, V_0, must be calculated, again based on known experimental and calculated parameters.

$$V_0^2 = 2\omega_t^2 z_0\delta + \omega_t^2\delta^2 - \frac{HR}{3m_c}\left[\frac{1}{a_0} - \frac{1}{\left(z_0 - z_c\right)}\right] - \frac{HR}{3m_c a_0^2}\left(\delta - z_0 + a_0 + z_c\right) + \frac{16E^*\sqrt{R}}{15m_c}\left(\delta - z_0 + a_0 + z_c\right)^{5/2} \qquad \text{Equation 2.9}$$

The solution to Equation 2.9 can also be used to estimate the maximum penetration depth, δ_1.

$$V_0 = \left(\frac{d\delta}{dt}\right)_0 \qquad \text{Equation 2.10}$$

These equations can be used to estimate the phase angle difference of varied materials in a heterogeneous sample. The general relationship to be derived from these equations is that larger differences in the reduced Young's modulus between two different materials result in larger phase angles and that stiffer samples exhibit larger phase angles.[22] This is considered for Pd-sputtered PC films immersed in water with hydrogen introduced to the samples as discussed in Chapter 5.

2.1.2.2 At the Liquid-solid Interface

When immersed in liquid, the energy dispersed by the probe into the medium was found to be at least two orders of magnitude greater compared to similar experiments under air.[24] The energy dispersed into the medium is about three times greater than the energy dispersed by tip-sample interactions.[24] Additionally, the relationship between the Young's modulus of the sample and the resulting phase angle was found to be inversed for a liquid-immersed sample.[25] Thus, an

increase in phase angle observed as an AFM probe in gas medium moves from a material with a low Young's modulus to one with a high Young's modulus would instead be detected as a decrease in phase angle when the same sample is scanned under water. The cause of this phenomenon is attributed to new channels of energy dissipation made available by the presence of liquid around the probe.[24,25]

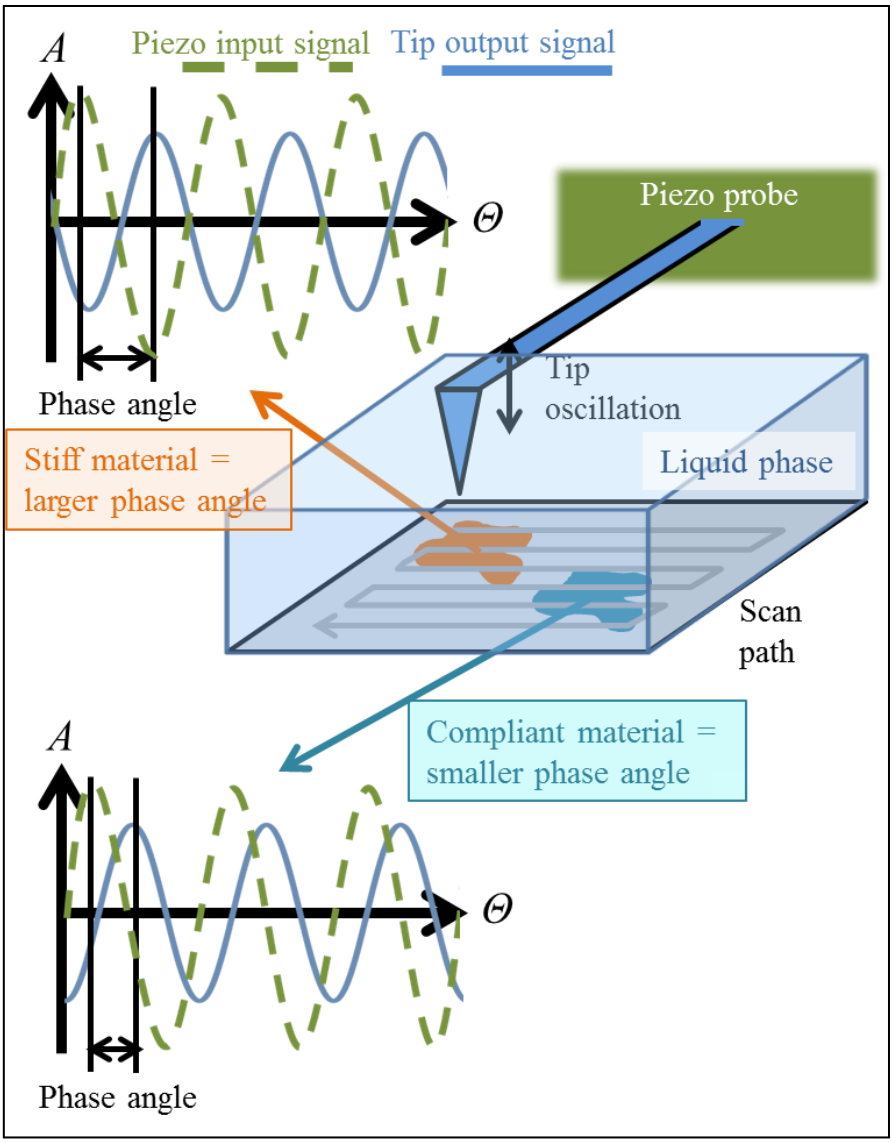

Figure 2.8 - The general behavior of AFM phase-angle data obtained for different material types in liquid.[24,25]

2.2 Material Science of Palladium

Palladium (Pd) is a silver-white metal that is solid at ambient conditions with a face-centered cubic crystal structure with a lattice parameter of 3.891 Å.[26] Its melting point and boiling point are 1552 °C and 3140 ± 1 °C, respectively.[27] At ambient conditions, Pd's density is 12.0000 g/cm^3 and its Brinell hardness is 37.300 MPa.[28] Pd films produced by magnetron sputter coating as used here have a polycrystalline structure with the (111) facet being the most commonly occurring at the surface of a sputtered film and a grain size between 15 and 30 nm.[29] At ambient conditions, Pd resists oxidation but will have an equilibrium surface coverage of adsorbed oxygen with a molar ratio of 0.25 O/Pd.[30] The Young's modulus and Poisson's ratio of Pd are 127 GPa and 0.39, respectively.[31,32] At ambient conditions, the surface of Pd is covered by a monolayer of chemisorbed oxygen.[33] Water was found to be absent from a Pd surface at temperatures above 200 K.[34]

2.3 Palladium/Hydrogen Interactions

The unique interactions of Pd and hydrogen have been the focus of extensive research.[35-38] Diatomic hydrogen molecules dissociate upon adsorption to Pd surfaces.[38] The adsorbed monoatomic hydrogen then can diffuse into the Pd crystal lattice to form palladium hydride (PdH).[39] Also, the adsorbed and absorbed hydrogen has been found to exist as protons (Figure 2.9).[39-41] As this process proceeds and the concentration of hydrogen in the bulk Pd increases, the lattice structure undergoes phase transitions defined by increases in the crystal lattice parameter.[42] Pd's lattice constant increases from 3.890 Å to 3.894 Å as it transitions to α-phase PdH.[42] At 20 °C and 1 atm of hydrogen, the maximum molar H/Pd ratio in the bulk α phase is 0.72.[42] At higher molar ratios, the α-phase PdH undergoes a phase transition to β-phase PdH, a highly distorted form of PdH with a lattice constant of 4.037 Å.[42] The maximum molar H/Pd ratio of β-phase PdH at 20 °C and 1 atm of hydrogen is 0.79.[42] This molar ratio is remarkable since the partial pressure of monoatomic hydrogen at 298 K and 1 bar is essentially negligible at 10^{-30} bar.[43] The full transition from pure Pd to β-phase PdH corresponds to an increase in the lattice constant of 3.78% and a volume increase of 11.8%.[42] Sputtered Pd films produced as samples for AFM experiments were calculated to have a thickness of 12 nm based on the parameters of the sputtering process.[44] A 3.78% increase in this thickness as the film transitions to PdH would cause the height of the sample to increase by 0.456 nm, which is below the vertical

resolution of the AFM setup. For a Pd film of about 12 nm thickness typical of the experiments performed here, the time from first contacting one side of the film with pure H_2 at ambient conditions to fully converting the sample to β-phase Pd can be estimated (by one sided diffusion into a semi-infinite slab) at 26 seconds.[45,46]

β-phase PdH has been found to have a Young's modulus and Poisson's ratio of 115 GPa and 0.40, respectively.[47] The differences in material properties of hydrogen-free and hydrogen-saturated Pd would lead to different phase angles during AFM based on the equations presented earlier. In air, as the Pd sample transitions from hydrogen-free to hydrogen-saturated, the AFM phase angle would be expected to increase.

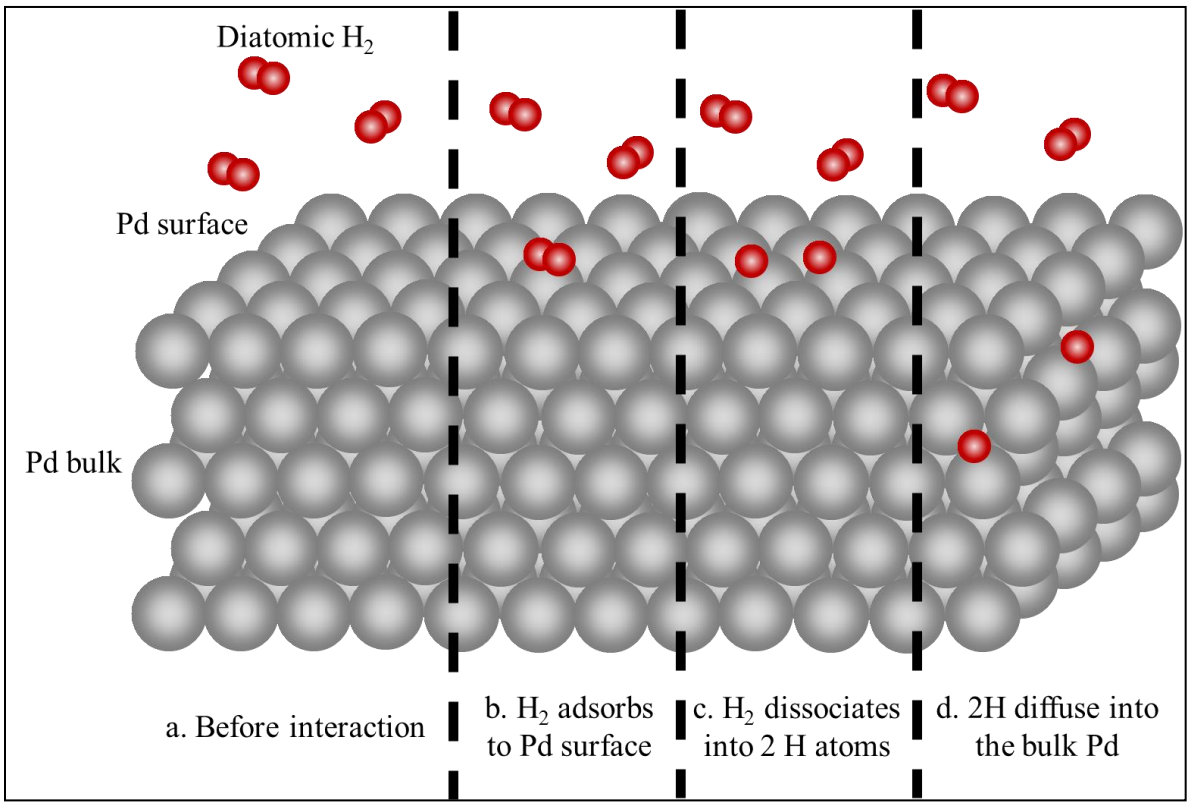

Figure 2.9 - Adsorption, dissociation, and diffusion of diatomic hydrogen into bulk Pd.

When hydrogen is introduced to a Pd surface with chemisorbed oxygen at room temperature, water is readily formed.[33,48] The reaction results in a decreased population of oxygen due to the increased presence of adsorbed hydrogen.[48] Over time, the oxygen is completely converted to gas-phase water and hydrogen is now adsorbed on the Pd surface.[49]

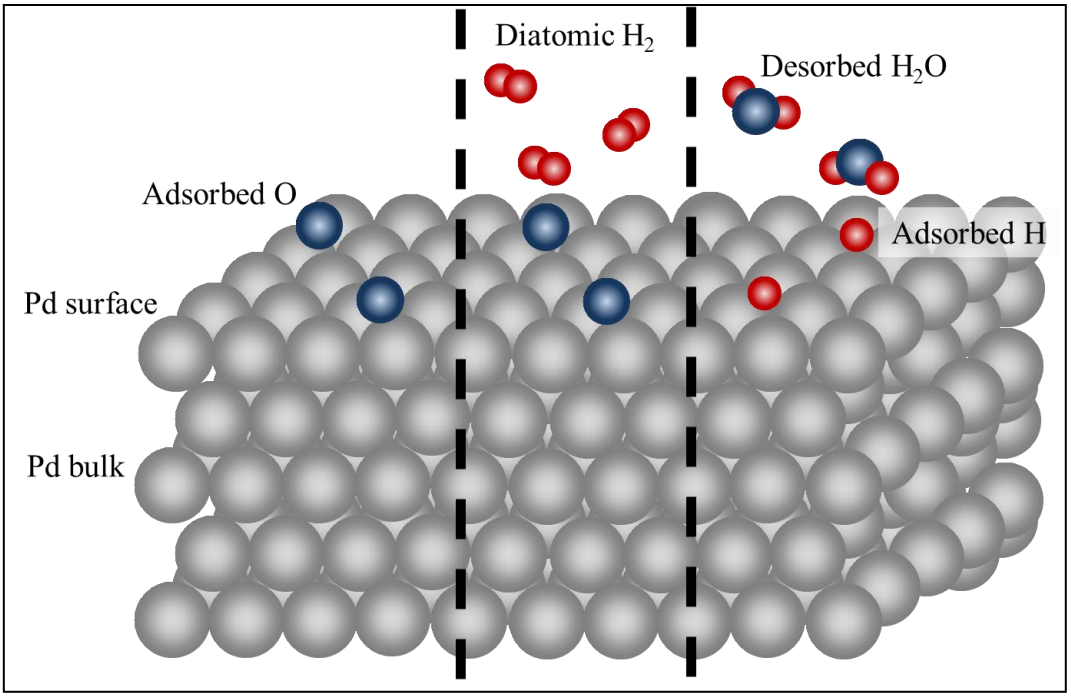

Figure 2.10 - The removal of adsorbed oxygen on a Pd surface using hydrogen to form water and adsorbed hydrogen.

Using ^{15}N nuclear reaction analysis (NRA) and thermal desorption spectroscopy (TDS) with surfaces labeled with isotopes (H and D), Ohno et al.[50] reported evidence of two different hydrogen populations at and near the Pd surface in the gas phase. The research indicated that the absorption process includes a stabilization step wherein monoatomic hydrogen occupies chemisorption wells prior to diffusion into the bulk.[50] Thus, hydrogen adsorption occurs more quickly than subsequent absorption of the monoatomic hydrogen. As the desorption process follows a kinetic process similar to the absorption process[42], the diffusion of hydrogen through the bulk Pd will be slow compared to the detachment of hydrogen off of the Pd surface. The diffusion process would still likely occur in a manner predicted by classical models, but the surface-bound hydrogen would depart in a less gradual manner once the bulk Pd is fully vacated. Investigations of the hydrogen presence on Pd surfaces, including the present one using AFM, would then expect to be subject to processes with easily calculable timescales while the surface concentration of hydrogen in a dynamic process would not be so easily predicted.

2.4 Estimates of the Diffusion of Hydrogen in Palladium, Polycarbonate, Water, and Composites

The diffusion of hydrogen at room temperature in PC, Pd, water, and composite systems is important to this work because the estimated times for the appearance or depletion of hydrogen from the probed interface were used to benchmark changes in phase angle. Diffusion estimate calculations were performed for the two experimental setups used in the different experiments performed. Although the estimates were based on the same equations, the differences in sample compositions, geometries, and gas supply methods between the two setups produced very different estimates for hydrogen diffusion.

2.4.1 Diffusion Coefficients, Sample Geometry, and Sources of Error

Diffusion calculations were made based on non-steady state, one-sided diffusion in a plane sheet with a uniform initial distribution. The mathematical solution for this system developed by Crank (Figure 2.11) was used.[51]

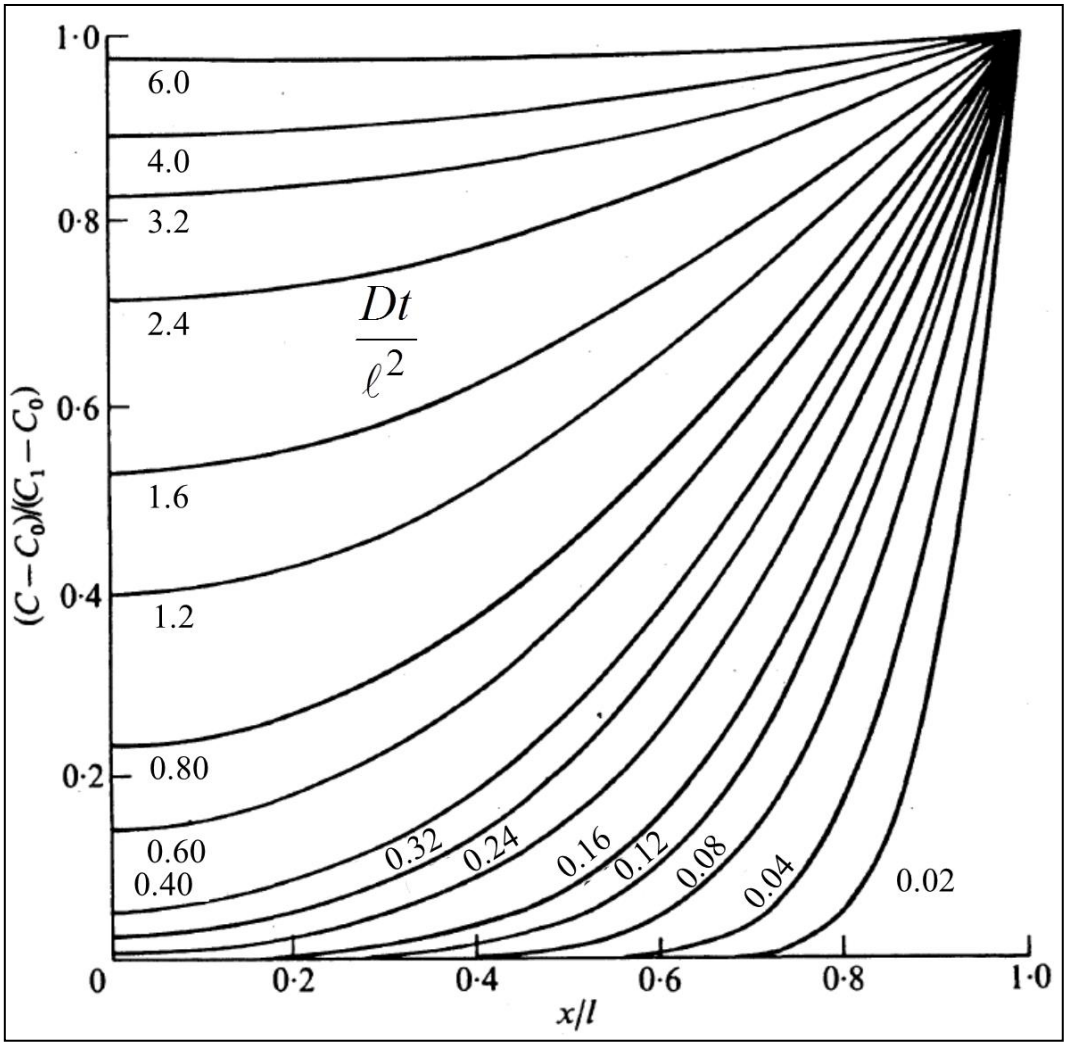

Figure 2.11 - Concentration distributions at various values of Dt/ℓ^2 in the sheet $0 < x < \ell$.[51] The values of Dt/ℓ^2 shown here are four times greater than used in the original version of this figure. These values are applicable to one-sided non-steady state diffusion in a plane sheet as opposed to the two-sided case upon which the original mathematical model was based.

If the dimensions of the plane sheet and the diffusion coefficient of the material are known, then Figure 2.11 can be used to determine the time required to achieve a particular concentration profile. D is the diffusion coefficient, t is time, ℓ is the thickness of the plane sheet, x is the position within the plane sheet, C is the concentration of the diffusing species at x, C_0 is the initial uniform concentration, and C_1 is the concentration at $x = \ell$. Two values of Dt/ℓ^2 are of particular interest: 0.24, which approximates when the diffusing species first appears at the side

opposite from which it was introduced, and 6.0, which approximates when the diffusing species has saturated the plane sheet.

For the experimental setups described in this dissertation, sources of error in the diffusion estimate include variation in the diffusion coefficient of PC due to the polymer film's thermal history, the thickness of the PC film, and the thickness of the Pd layer based on the sputter-deposition process. Reported diffusion coefficients for hydrogen in cast PC films at 25 °C include 4.6×10^{-6} cm^2/s[52] and 7.0×10^{-6} cm^2/s.[53] Additionally, a diffusion coefficient for helium (used as an approximation for hydrogen transport in polymers) in a melt-extruded PC film tested as received at 25 °C was 1.7×10^{-6} cm^2/s.[54] Based on these three values from literature, the diffusion coefficient of PC was $4.4 \pm 2.2 \times10^{-6}$ cm^2/s. The PC films used to prepare samples had a measured thickness of 260 ± 3.3 μm (standard deviation of 20 measurements made using a micrometer screw). Based on nominal parameters of the sputtering process and variations caused by manual control of the chamber pressure and the applied current, the thickness of the Pd layer was 12.0 ± 3.6 nm (estimated from the observed variations in gas chamber pressure and sputtering current).[44] The diffusion coefficients of hydrogen in Pd and water (assumed stagnant) were $2.8 \pm 0.2\times10^{-7}$ cm^2/s and $4.80 \pm 0.522\times10^{-5}$ cm^2/s, respectively.[55-57]

2.4.2 Diffusion Estimates for the Palladium-gas Interface (Chapter 3)

For AFM studies of the gas-immersed Pd surface, the model system used was a sputtered Pd layer (ℓ = 12.0 ± 3.6 nm) on a commercial compact disc (PC, ℓ = 1.2 mm). Nitrogen or hydrogen were supplied to the scanned area by flowing it over the sample (Figure 2.12).

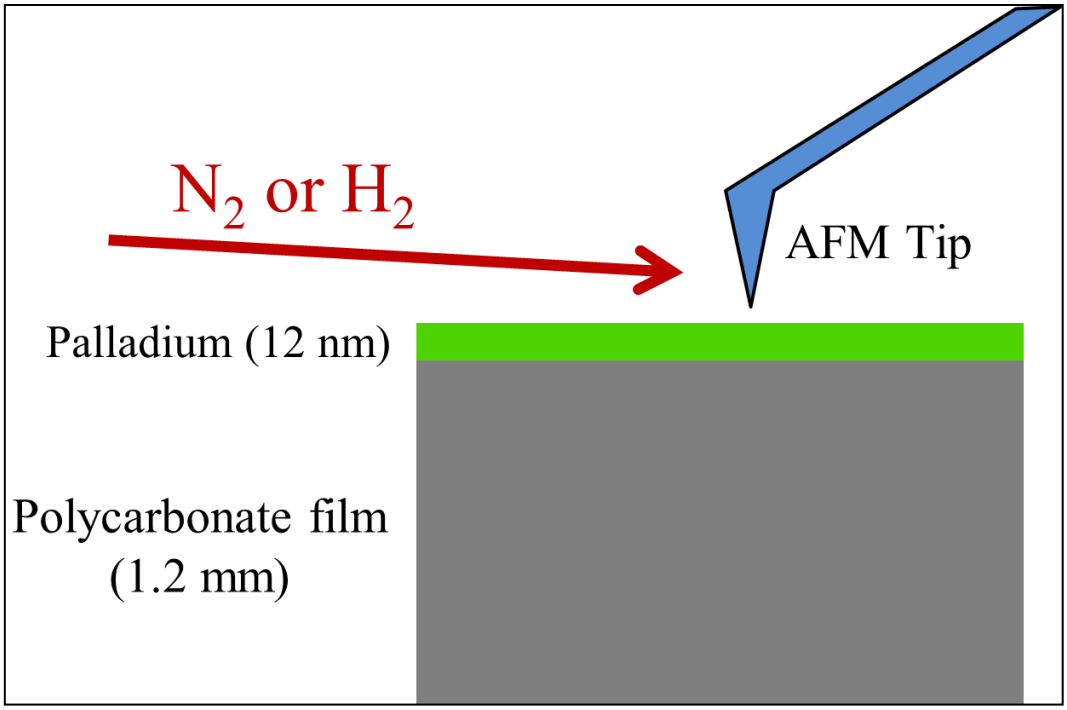

Figure 2.12 - Schematic of the model system used for studies of the Pd-gas interface. Nitrogen or hydrogen was flowing over the scanned area of the sputtered Pd film on a PC substrate.

Because high-purity gases were used, it was assumed that no diffusion limitations to mass transfer occurred in the gas phase above the Pd surface. The Pd surface was assumed to be essentially instantaneously saturated upon introduction of hydrogen flow. Based on the ranges of the sputtered Pd layer's thickness and the diffusion coefficient of Pd, the time required to saturate the entire Pd layer by one-sided non-steady state diffusion after the application of hydrogen to the surface was estimated to be 47 ± 28 s. Similarly, the time required to saturate the PC substrate by the same process was estimated to be $3.2 \pm 2.0 \times 10^4$ s (8.8 ± 5.6 hr). However, hydrogen was supplied to the Pd surface for only 300 s. While the Pd layer was almost certainly saturated with hydrogen, the PC substrate was relatively hydrogen-poor. Therefore, for hydrogen diffusion out of the sample (the process studied by AFM as discussed in Chapter 3), only the Pd layer was considered. The process for removal of hydrogen from the Pd layer was expected to be the reversal of the addition of hydrogen to the same system by diffusion, so the time required for complete depletion of hydrogen from the Pd layer after exposing the surface to nitrogen was estimated to be 47 ± 28 s.

2.4.3 Diffusion Estimates for the Palladium-water Interface (Chapter 5)

For AFM studies of the water-immersed Pd surface, the model system used was a sputtered Pd layer (ℓ = 12 ± 3.6 nm) on a melt-extruded PC film used as received (ℓ = 260 ± 3.3 μm). This composite sample was placed under a layer of degassed water (ℓ = 7 ± 1 mm). This water layer was covered by the probe holder of the AFM system, so diffusion of gases would only occur between the composite sample and water layers. Nitrogen or hydrogen was supplied to the scanned area by either pressurizing the space below the sample to 10 psig or by flowing the gas under the sample essentially at atmospheric pressure (Figure 2.13).

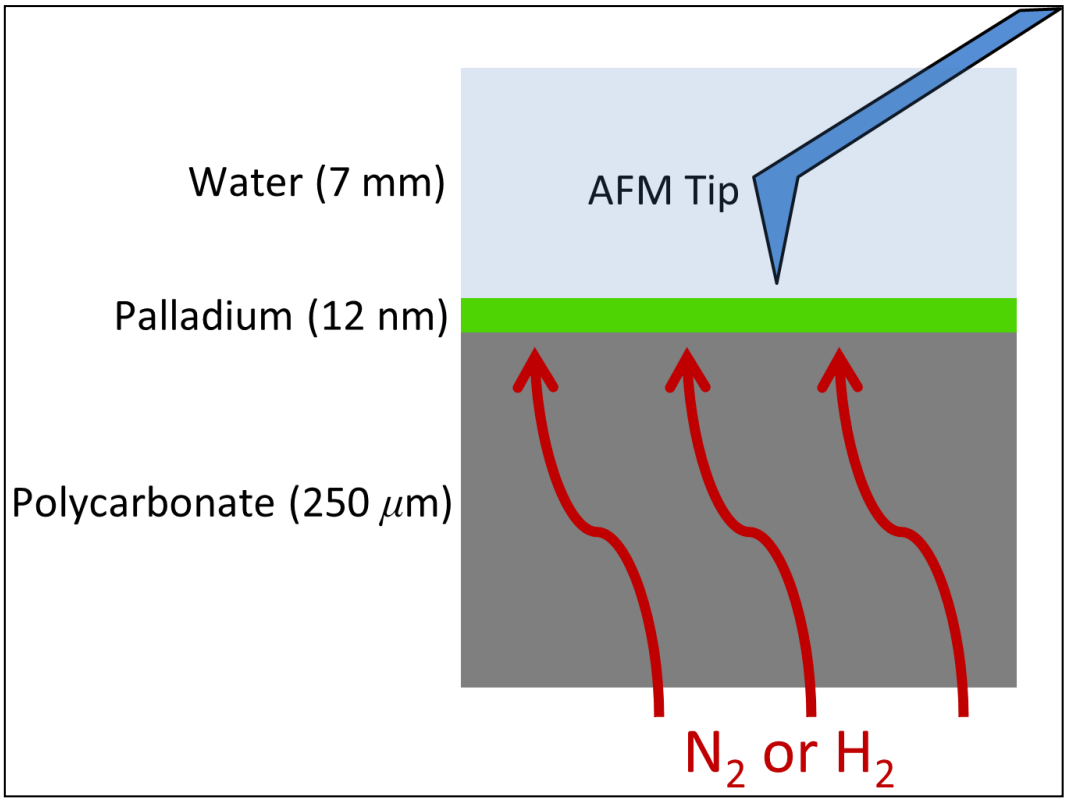

Figure 2.13 - Schematic of the model system used for studies of the Pd-gas interface. Nitrogen or hydrogen was either pressurized to 10 psig or flowing underneath the PC-Pd composite sample immersed in water.

Based on the ranges of the PC layer's thickness and diffusion coefficient, the time required for hydrogen to appear at at the Pd-water interface by one-sided non-steady state diffusion was estimated to be 61 ± 38 s. For this same process through the Pd layer based on the ranges of its thickness and diffusion coefficient, the time required for the appearance of hydrogen was

estimated to be $1.38 \pm 0.82 \times 10^{-6}$ s. The time for diffusion through the Pd layer can therefore be neglected.

For complete saturation of the PC layer with hydrogen, the time required was estimated to be $1.5 \pm 0.9 \times 10^{3}$ s (25 ± 15 min). Similarly, the time required for saturation of the Pd layer with hydrogen was between 47 ± 28 s (see subchapter 2.4.2). Estimating the time required for the appearance of hydrogen at the Pd-water interface and the saturation with hydrogen of the entire PC-Pd composite would be difficult due to the disparities between the diffusion coefficients and the thicknesses of the two materials. However, as demonstrated in the time estimates for the PC and Pd layers considered separately, the PC layer is the significant barrier to hydrogen transport to the Pd-water interface due to its thickness being several orders of magnitude greater than that of the Pd layer. Therefore, only the diffusion estimates for the PC layer was considered when benchmarking against changes in phase angle during the AFM experiments.

After the PC-Pd composite was saturated, hydrogen would still continue to diffuse into the water layer above the Pd surface (assuming the water layer is largely stagnant and convection can be neglected). However, the time required for the saturation of the water layer with hydrogen was 61,000 s (17 hr), which was far greater than the 34 min of hydrogen exposure to the underside of the PC-Pd composite. Thus, during the experiment, the water layer was still far from hydrogen saturation. When the gas under the PC-Pd composite was switched to nitrogen, hydrogen would diffuse from the PC and Pd layers into the nitrogen supply. Because of the dissolved hydrogen present in the water layer below its saturation level, the diffusion of hydrogen out of the PC-Pd composite will not be the reversal of the diffusion of hydrogen into the same system. In the actual system, a small amount of hydrogen would be available to adsorb from the water layer to the nearby Pd surface until all of the hydrogen has been depleted. This would lead to a significantly larger time required for hydrogen to be removed completely from the system compared to the one-sided diffusion estimate in which only the PC layer was considered. Thus, the introduction of hydrogen to the Pd-water interface and its subsequent removal would have different dynamics.

In some experiments, gas was supplied to the PC-Pd composite by pressurizing the space underneath the sample. Nitrogen and hydrogen were exchanged by pulse purging of one gas by the other. This was done by repeatedly opening and closing the valve at one end of the gas

supply multiple times for 10 s. The volume of the gas supply space under the sample was about 730 cm^3. The highest possible total volume of hydrogen in the saturated PC-Pd-water system was 0.16 cm^3 (STP) (based on the solubilities of hydrogen in PC, Pd, and water of 2.0×10^{-2} cm^3 (STP)/cm^3, 9.1 cm^3 (STP)/cm^3, and 1.9×10^{-2} cm^3 (STP)/cm^3, respectively. See Table 1). Because the volume of nitrogen under the sample was so much greater than the volume of hydrogen available to diffuse out of the PC, Pd, and water, there was always a sufficient driving force for this diffusion to occur. This is also true for the experiments in which flowing gas was used to supply nitrogen or hydrogen to the underside of the sample due the much faster diffusion in the gas phase compared to solids.

2.5 References

[1] Binnig, G.; Quate, C. F.; Gerber, Ch. Atomic Force Microscope. *Phys. Rev. Lett* **1986**, *56* (9), 930-933.

[2] Sugawara, Y. Atomic Force Microscopy. In *Roadmap of Scanning Probe Microscopy*; Morita, S., Ed.; Springer-Verlag: Berlin Heidelberg, 2007; pp 15-21.

[3] Morris, V. J.; Kirby, A. R.; Gunning, A. P. Atomic Force Microscopy for Biologists, 2nd Ed.; Imperial College Press: London, 2010.

[4] McBride, S. P. Surface Science Experiments Involving the Atomic Force Microscope. Ph.D. Thesis, Kansas State University, Manhattan, KS, 2012.

[5] Zaera, F. Probing Liquid/Solid Interfaces at the Molecular Level. *Chem. Rev.* **2012**, *112*, 2920-2986.

[6] Bhushan, B. Surface Roughness Analysis and Measurement Techniques. In *Modern Tribology Handbook Vol. 1*. (CRC Press, Boca Raton, SA, 2001), Chap. 2.

[7] Measuring Surface Roughness with Atomic Force Microscopy; Asylum Research. July 2013.

[8] Kamins, T. I.; Carr, E. C.; Williams, R. S.; Rosner, S. J. Deposition of three-dimensional Ge islands on Si(001) by chemical vapor deposition at atmospheric and reduced pressures. *J. Appl. Phys.* **1997**, *81*, 211-219.

[9] Kozlov, G. V.; Dolbin, I. V.; Shogenov, V. Kh.; Zaikov, G. E. Application of the Fractional Derivative Theory to the Estimation of the End-to-end Distance of Polycarbonate Chains. *J. Appl. Polym. Sci.* **2004**, *91* (6), 3765-3768.

[10] Salcedo, K. L.; Rodriguez, C. A.; Perez, F. A.; Riascos, H. Morphological Study of Palladium Thin Films Deposited by Sputtering. *J. Phys. Conf. Ser.* **2011**, *274*, 012120.

[11] Hofmann, S. Sputter Depth Profile Analysis of Interfaces. *Rep. Prog. Phys.* **1998**, *61*, 927-888.

[12] Fuierer, R. (Asylum Research, Procedural Operation 'Manualette' Beta Version 10, Based on software version 080501, 2008).

[13] James, P. J.; Antognozzi, M.; Tamayo, J.; McMaster, T. J.; Newton, J. M.; Miles, M. J. Interpretation of Contrast in Tapping Mode AFM and Shear Force Microscopy. A Study of Nafion. *Langmuir* **2001**, *17*, 349-360.

[14] Mclean, R. S.; Sauer, B. B. Tapping-Mode AFM Studies Using Phase Detection for Resolution of Nanophases in Segmented Polyurethanes and Other Block Copolymers. *Macromolecules* **1997**, *30*, 8314-8317.

[15] Magonov, S. N.; Elings, V.; Whangbo, M.-H. Phase Imaging and Stiffness in Tapping-mode Atomic Force Microscopy. *Surf. Sci.* **1997**, *375*, L385-L391.

[16] Schmitz, I.; Schreiner, M.; Friedbacher, G.; Grasserbauer, M. Phase Imaging as an Extension to Tapping Mode AFM for the Identification of Material Properties on Humidity-sensitive Surfaces. *Appl. Surf. Sci.* **1997**, *115*, 190-198.

[17] Bhushan, B.; Qi, J. Phase Contrast Imaging of Nanocomposites and Molecularly Thick Lubricant Films in Fagnetic Media. *Nanotechnology* **2003**, *14*, 886-895.

[18] Xu, Z. W.; Liang, Y. C.; Dong, S.; Cao, Y. Z.; Zhao, T. Q.; Wang, J. H.; Zhao, Q. L. Phase Contrast Imaging of SEBS Triblockcopolymer Studied by Carbon Nanotubes Probe. *Ultramicroscopy* **2005**, *105*, 72-78.

[19] Tamayo, J.; García, R. Relationship between Phase Shift and Energy Dissipation in Tapping-mode Scanning Force Microscopy. *Appl. Phys. Lett.* **1998**, *73*, 2926-2928.

[20] Behrend, O. P.; Odoni, L.; Loubet, J. L.; Burnham, N. A.; Phase imaging: Deep or superficial? *App. Phys. Lett.* **1999**, *75*, 2551-2553.

[21] Bar, G.; Thomann, Y.; Brandsch, R.; Cantow, H.-J.; Whangbo, H.-H.; Factors Affecting the height and Phase Images in Tapping Mode Atomic Force Microscopy. Study of Phase-Separated Polymer Blends of Poly(ethene-co-styrene) and Poly(2,6-dimethyl-1,4-phenylene oxide). *Langmuir* **1997**, *13*, 3807-3812.

[22] Martínez, N. F.; García, R. Measuring Phase Shifts and Energy Dissipation with Amplitude Modulation Atomic Force Microscopy. Nanotechnology 2006, 17, S167-S172.

[23] Zhao, Y.; Cheng, Q.; Qian, M.; Cantrell, J. H.;Phase image contrast mechanism in intermittent contact atomic force. *J. Appl. Phys.* **2010**, *108*, 094311.

[24] Melcher, J.; Carrasco, C.; Xu, X.; Carrascosa, J. L.; Gómez-Herrero, J.; de Pablo, P. J.; Raman, A.; Origins of phase contrast in the atomic force microscope in liquids. *P. Natl. Acad. Sci. USA* **2009**, *106* (33), 13655-13660.

[25] Payam, A. F.; Ramos, J. R.; Garcia, R.; Molecular and Nanoscale Compositional Contrast of Soft Matter in Liquid: Interplay between Elastic and Dissipative Interactions. *ACS Nano* **2012**, *6* (6), 4663-4670.

[26] Yaws, C.L. Yaws' Handbook of Properties of the Chemical Elements [Online]; Knovel, 2011; Ch. 74, pp 302-305. https://app.knovel.com/web/toc.v/cid:kpYHPCE007/viewerType:toc/root_slug:yaws-handbook-properties/url_slug:kt008XCBT4 (accessed 30 March 2016).

[27] *A Dictionary of Chemistry*, 6th Ed.; Daintith, J., Ed. Oxford University Press: Oxford, 2008; 397.

[28] Wunder, R. W.; Cobes, J. W.; Phillips, J.; Radovic, L. R.; Peinado, A. J. L.; Carrasco-Marin, F. Microcalorimetric Study of the Absorption of Hydrogen by Palladium Powders and Carbon-supported Palladium Particles. *Langmuir* **1993**, *9*, 984-992.

[29] Love, J. C.; Estroff, L. A.; Kriebel, J. K.; Nuzzo, R. G.; Whitesides, G. M. Self-assembled monolayers of thiolates on metals as a form of nanotechnology. *Chem. Rev.* **2005**, *105*, 1103-1169.

[30] Guo, X., Hoffman, A., and Yates, Jr., J.T. Adsorption kinetics and isotopic equilibration of oxygen adsorbed on the palladium(111) surface. *J. Chem. Phys.* **1989**, *90*, 5787-5792.

[31] Finot, E.; Fabre, A.; Passian, A.; Thundat, T.; Dynamic and Static Manifestation of Molecular Absorption in Thin Films Probed by a Microcantilever. *Phys. Rev. App.* **2014**, *1*, 024001-1-024001-5.

[32] Gercek, H.; Poisson's ratio values for rocks. *Int. J. Rock Mech. Min.* **2007**, *44*, 1-13.

[33] Petersson, L.-G.; Dannetun, H. M.; Lundström, I.; The Water-forming Reaction on Palladium. *Surf. Sci.* **1985**, *161*, 77-100.

[34] Gates, J. A. Kesmodel, L. L.; Methanol Adsorption and Decomposition on Clean and Oxidized Palladium (111). *J. Catal.* **1983**, *83* (2), 437-445.

[35] Flanagan, T. B. and Oates, W. A. The Palladium-Hydrogen System. *Annu. Rev. Mater. Sci.* **1991**, *21*, 269-304.

[36] Darling, A. S. The Diffusion of Hydrogen through Palladium. *Platinum Metals Rev.* **1958**, *2* (1), 16-22.

[37] Baber, A. E., Tierney, H. L., Lawton, T. J., Sykes, E. C. H. An Atomic-Scale View of Palladium Alloys and their Abilityto Dissociate Molecular Hydrogen, *ChemCatChem* **2011**, *3*, 607-614.

[38] Jewell, L. L. and David, B. H. Review of absorption and adsorption in the hydrogen-palladium system. *Appl. Catal. A-Gen.* **2006**, *310*, 1-15.

[39] Conrad, H.; Ertl, G.; Latta, E. E. Adsorption of hydrogen on palladium single crystal surfaces. *Surf. Sci.* **1974**, *40* (2), 435-446.

[40] Eastman, D. E.; Cashion, J. K.; Switendick, A. C. Photoemission studies of energy levels in the palladium-hydrogen system. *Phys. Rev. Lett.* **1971**, *27* (1), 35-38.

[41] Peisl, J. Lattice Distortion, Elastic Interaction, and Phase Transitions of Hydrogen in Metal. In *Advances in Solid State Physics*; Grosse, P., Ed.; Friedr. Vieweg & Sohn Verlagsgesellschaft mbH: Braunschweig, 1984; Vol. 24, pp 45-72.

[42] Wicke, E.; Brodowsky, H. Hydrogen in Palladium and Palladium Alloys. In *Hydrogen in Metals II*; Alefeld, G., Völkl, J., Eds.; Topics in Applied Physics; Springer-Verlag: Berlin, 1978; Vol. 29, pp 73-155.

[43] Oates, W. A. , Flanagan, T. The Reaction of Hydrogen Atoms with Palladium and its Alloys. *Can. J. Chem.* **1975**, *53* (5), 694-701.

[44] *Operating Instructions for Denton Vacuum, LLC DESK II Cold Sputter/Etch Unit and Carbon Evaporation Accessory*; Denton Vacuum, LLC: Moorestown, NJ, 1998.

[45] Hironori U.; Tatsuo N.; Isamu U. Electrochemical Measurements of Single Particles of Pd and LaNi5 with a Microelectrode Technique. *J. Electroanal. Chem.* **1995**, *396*, 169-173.

[46] Brass, A. M.; Collet-Lacoste, J. The Influence of Surface on the Permeation of Hydrogen in Iron and Palladium. In *Proceedings of the Symposium on Electrochemical Surface Science of Hydrogen Adsorption and Absorption*; Jerkiewicz, G., Marcus, P., Eds.; The Electrochemical Society, Inc.: Pennington, NJ, 1997; pp 200-210.

[47] Wei, C.; Kong, F. T.; Gong, H. R.; Phase stability and elastic property of PdH and PdCuH phases. *Int. J. Hydrogen Energ.* **2013**, *38*, 16485-16494.

[48] Oh, C.; Hong, K. S.; Lee, S. G.; Park, C.-H.; Yu, I.; Catalytic oxidation of hydrogen at nanocrystalline palladium surfaces. *J. Phys.: Condens. Matter* **2006**, *18*, 3335-3341.

[49] Dus, R.; Nowicka, E.; Wolfram, Z.; Influence of Oxygen or Methane Preadsorption on Low-Temperature Atomic Deuterium Emission from Palladium Deuteride. *Langmuir* **1998**, *14*, 4545-4551.

[50] Ohno, S.; Wilde, M.; Fukutani, K.; Novel insight into the hydrogen absorption mechanism at the Pd(110) surface. *J. Chem. Phys.* **2014**, *140*, 134705.

[51] Crank, J. The Mathematics of Diffusion; Oxford University Press: Oxford, U.K., 1975; pp 45-68.

[52] Koros, W. J.; Chan, A. H.; Paul, D. R. Sorption and transport of various gases in polycarbonate. *J. Membr. Sci.* **1997**, *2* (2), 165-190.

[53] Gusev, A. A.; Suter, U. W.; Moll, D. J. Relationship between Helium Transport and Molecular Motions in a Glassy Polycarbonate. *Macromolecules* **1995**, *28*, 2582-2584.

[54] Costello, L. M.; Koros, W. J. Effect of Structure on the Temperature Dependence of Gas Transport and Sorption in a Series of Polycarbonates. *J. Polym. Sci.* **1994**, *32* (4), 701-713.

[55] Hironori U.; Tatsuo N.; Isamu U. Electrochemical Measurements of Single Particles of Pd and LaNi5 with a Microelectrode Technique. *J. Electroanal. Chem.* **1995**, *396*, 169-173.

[56] Collet-Lacoste, J. The Influence of Surface on the Permeation of Hydrogen in Iron and Palladium. In *Proceedings of the Symposium on Electrochemical Surface Science of Hydrogen Adsorption and Absorption*; Jerkiewicz, G., Marcus, P., Eds.; The Electrochemical Society, Inc.: Pennington, NJ, 1997; pp 200-210.

[57] Mazarei, A. F.; Sandall, O. C. Diffusion Coefficients for Helium, Hydrogen, and Carbon Dioxide in Water at 25°C. *AIChE J.* **1980**, *26* (1), 154-157.

3 Analysis of Atomic Force Microscopy Phase-angle Data to Dynamically Detect Hydrogen Adsorbed on Palladium from the Gas Phase under Ambient Conditions[1]

3.1 Introduction

Characterization of the interactions of hydrogen with catalytic metal surfaces and the mass transfer processes involved in heterogeneous catalysis are important for catalyst development. Although a range of technologies for studying catalytic surfaces exists, much of it relies on high-vacuum conditions that preclude in-situ research. In contrast, atomic force microscopy (AFM) provides an opportunity for direct observation of surfaces under or near actual reaction conditions. Tapping-mode AFM was explored here because it expands AFM beyond the usual topographic information toward speciation and other more subtle surface information. This work describes using phase-angle data from tapping-mode AFM to follow the interactions of hydrogen with palladium, polycarbonate, and iron. Real-time AFM phase-angle data allowed for the observation of multiphase mass transfer to and from the surface of palladium at atmospheric pressure and room temperature without the need for complex sample preparation. The AFM observations are quantitatively benchmarked against and confirm mass transfer predictions based on bulk hydrogen diffusion data. Additionally, they support recent studies that demonstrate the existence of multiple hydrogen states during interactions with palladium surfaces.

More than 80% of all synthetic chemicals are produced using catalysis.[1] Interactions of hydrogen with catalytic metal surfaces during heterogeneous catalysis are of great interest for a number of important processes including petrochemical processing,[1] soybean oil hydrogenation,[2] pharmaceutical production,[3] fine chemical production,[3] and lately conversion of biomass to fuels and chemicals.[4] Adsorption of hydrogen on solid (metal) surfaces is the necessary first step for heterogeneous hydrogenation catalysis.[5,-7] Of particular interest is therefore the availability of hydrogen on catalytic surfaces because it impacts productivity and selectivity.[2] Direct, real-time

[1] The majority of the material in this chapter has been published in: Young, M. J., Pfromm, P. H., Rezac, M. E., Law, B. M., "Analysis of Atomic Force Microscopy Phase Data To Dynamically Detect Adsorbed Hydrogen under Ambient Conditions", *Langmuir,* **2014,** *30* (40), 11906-11912.

observation of the dynamic appearance and disappearance of hydrogen on a palladium (Pd) surface at ambient pressure is absent from the literature.

Atomic force microscopy (AFM) can be performed without vacuum and with only rudimentary sample preparation. Tapping-mode AFM is particularly useful for producing high-resolution images. Topography data are the primary focus of tapping-mode AFM, but cantilever phase-angle data (Figure 3.1) can be used to study the chemical nature of surfaces.[8]

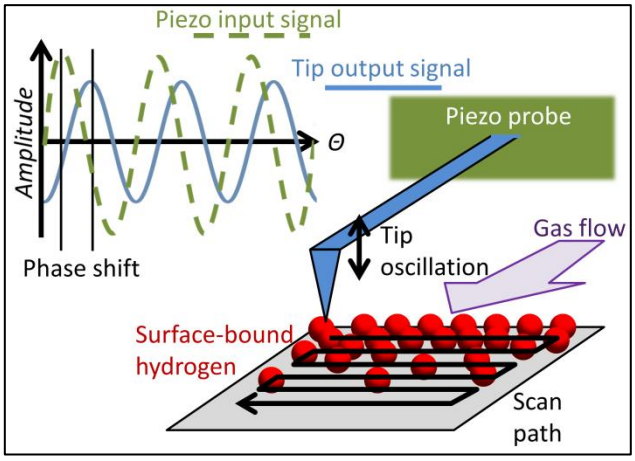

Figure 3.1 - Schematic of phase-angle AFM for the detection of surface-bound hydrogen.

A smaller phase angle indicates repulsive forces between the tip and sample, while a larger phase angle indicates an attractive force.[9,10] Phase-angle data have been used to distinguish between solid surface materials such as tribofilms formed as a result of wear, and distinct areas of an immiscible polymer blend.[11,12] Much research has been done to determine what affects phase angle in AFM.[13-15] A generally accepted theory is that the phase angle is related to changes in energy dissipation interactions between the probe and sample.[9,10,16,17] Tamayo and García[9] proposed a model for the energy dissipated per cantilever oscillation

$$E_{dis} = E_{ext} - E_{med} = \frac{\pi k A_t A_0 \sin(\varphi)}{Q} - \frac{\pi k A_t^{\,2} \omega_t}{Q \omega_0} \qquad \text{Equation 3.1}$$

This equation is based on the energy dissipated by probe-sample interaction (E_{dis}) [eV] as the difference between the energy supplied externally to the probe (E_{ext}) [eV] and the hydrodynamic effects of the medium acting on the probe (E_{med}) [eV]. Thus, for a cantilever probe with spring constant k [N/m], tapping amplitude A_t [nm], free amplitude A_0 [nm], driving

frequency ω_t [kHz], natural resonance frequency ω_0 [kHz], quality factor Q, and phase angle φ [°], the energy dissipated can be easily calculated. The difference in dissipated energy between two regions of an AFM scan can be also be calculated:

$$\Delta E_{dis} = E_{dis,2} - E_{dis,1} = \left(\frac{\pi k A_t A_0 \sin(\varphi)}{Q} - \frac{\pi k A_t^2 \omega_t}{Q\omega_0} \right)_2 - \left(\frac{\pi k A_t A_0 \sin(\varphi)}{Q} - \frac{\pi k A_t^2 \omega_t}{Q\omega_0} \right)_1$$

Equation 3.2

In tapping-mode AFM, ω_0, ω_t, A_0, and A_t remain constant for the duration of a scan. This allows eq (2) to be simplified:

$$\Delta E_{dis} = \frac{\pi k A_t A_0}{Q} (\sin(\varphi_2) - \sin(\varphi_1))$$

Equation 3.3

Measurement and analysis of ΔE_{dis} can provide insight into the degree to which the surface is attractive or repulsive. This information can assist in speciation on the basis of differences in material properties.

It is demonstrated here that AFM phase-angle data can be used to observe the dynamic adsorption and desorption of hydrogen on a catalytic Pd surface at room temperature and atmospheric pressure. This capability may allow further insights into the mass transfer and kinetics of heterogeneous catalyzed reactions and improved design of conventional catalysts and membranes.

A more desirable interpretation of AFM phase-angle data is one that directly links it to material properties. This approach was elusive due to the number of factors that affect phase angle including the ratio between probe excitation and resonance frequencies, sample elastic properties, the tip's radius, sample-tip friction, cantilever tilt angle, and various morphological and compositional contributions.[18] However, it has been found that changes in phase angle can be related to Young's modulus and Poisson's ratio for the tip and sample materials.[19] This model was developed based on a collision between a tip of known radius R and the sample.

$$\Delta\Omega = (\varphi)_2 - (\varphi)_1 = \pi T \left[\left(\frac{1}{2t_0 + t_1} \right)_2 - \left(\frac{1}{2t_0 + t_1} \right)_1 \right]$$

Equation 3.4

Here, $\Delta\Omega$ is defined as the difference in phase angle between different points on a sample. T [ns] is the free-space oscillation period of the cantilever, t_0 [ns] is the time required for one complete free-space oscillation of the cantilever, and t_1 [ns] is the time required for the cantilever to move from the fully deflected position to maximum impact with the sample (also called the collision half-time). T and t_0 are calculated from values determined during the cantilever tuning process.

$$T = \frac{1}{\omega_0} \qquad \text{Equation 3.5}$$

$$t_0 = \frac{1}{\omega_0}\arcsin\left(\frac{z_0}{A_0}\right) \qquad \text{Equation 3.6}$$

z_0 [nm] is the distance between the tip of the non-deflected cantilever and the sample. This is determined from the ratio between set-point amplitude and the driving amplitude of the cantilever. The collision half-time, t_1, can be calculated using a number of experimental and calculated parameters for the system.[23]

$$t_1 = \int_0^{\delta_1} \left\{ V_0^2 - 2\omega_t^2 z_0 \delta - \omega^2 \delta^2 + \frac{HR}{3m_c}\left[\frac{1}{a_0} - \frac{1}{(z_0 - z_c)}\right] + \frac{HR}{3m_c a_0^2}(\delta - z_0 + a_0 + z_c) - \frac{16E^*\sqrt{R}}{15m_c}(\delta - z_0 + a_0 + z_c)^{5/2} \right\}^{-(1/2)} d\delta \qquad \text{Equation 3.7}$$

where V_0 [μm/s] is the initial tip-sample collision velocity, δ [nm] is the instantaneous penetration depth of the tip into the sample, δ_1 [nm] is the maximum penetration depth, a_0 [Å] is the van der Waal's radius, H is the Hamaker constant, R [nm] is the tip radius, m_c [kg] is the mass of the cantilever, and z_c [nm] is the tip-sample separation distance at which strong interaction force is encountered. Most importantly, E^* [Pa] is the reduced Young's modulus, which is derived from the Young's moduli and Poisson's ratios of the tip and sample.

$$\left(E^*\right)^{-1} = \left[\frac{\left(1-\upsilon_S^2\right)}{E_S} + \frac{\left(1-\upsilon_T^2\right)}{E_T}\right] \qquad \text{Equation 3.8}$$

Here, E [Pa] is the Young's modulus and υ is the Poisson's ratio with the subscripts S and T referring to the sample and tip, respectively. To calculate t_1, the initial tip-sample collision velocity, V_0, must be calculated, again based on known experimental and calculated parameters.

$$V_0^2 = 2\omega_t^2 z_0 \delta + \omega_t^2 \delta^2 - \frac{HR}{3m_c}\left[\frac{1}{a_0} - \frac{1}{(z_0 - z_c)}\right] - \frac{HR}{3m_c a_0^2}(\delta - z_0 + a_0 + z_c) + \frac{16E^*\sqrt{R}}{15m_c}(\delta - z_0 + a_0 + z_c)^{5/2} \quad \text{Equation 3.9}$$

The solution to Equation 3.9 can also be used to estimate the maximum penetration depth, δ_1.

$$V_0 = \left(\frac{d\delta}{dt}\right)_0 \quad \text{Equation 3.10}$$

These equations can be used to estimate the difference in phase angle of varied materials in a heterogeneous sample. The general relationship to be derived from these equations is that larger differences in the reduced Young's modulus result in larger phase angles and that stiffer samples exhibit smaller phase angles.[19]

3.2 Experimental Setup and Procedure

The AFM instrument was an Asylum Research MFP-3D instrument operated in AC mode using WaveMetrics Igor Pro version 5.0.5.7. Olympus AC240TS-R3 cantilever probes (tetrahedral geometry with a radius of ~9 ± 2 nm) were used throughout. Ethanol (Sigma-Aldrich, ACS reagent, ≥99.5 wt%), toluene (Fisher Scientific, Certified ACS, 99.9 wt% assay), and chloroform (Fisher Scientific, Certified ACS, 99.9 wt% assay) were used as cleaning agents. A polycarbonate desiccator (Nalgene, Rochester, NY) evacuated by a direct drive vacuum pump (Thermo Electron Corp., Waltham, MA) was used to dry probes and samples. Static charge on samples and probes was removed by exposure for 10 s to a 500 μCi polonium-210 source (NRD LLC, model 3C500) immediately prior to imaging.[20] Polycarbonate (PC) samples were cut from commercial compact discs.[21] Some samples were then used to prepare sputter-coated PC samples. These samples were sputtered using a 99.95 wt% Pd sputter target (Ted Pella, Redding, CA) using a DESK II magnetron sputter coater (Denton Vacuum, Moorestown, NJ) for 45 s with a current of 45 mA in a 100 mTorr ambient air atmosphere. The iron (Fe) surface was a 99.5

wt% Fe sputter target (as supplied by Ted Pella). Hydrogen and nitrogen at nominal purities of 99.999 vol% were supplied by Matheson Tri-Gas (Manhattan, KS). The gas flow was adjusted using Swagelok 316 stainless steel valves and tubing (Kansas Valve and Fitting, Kansas City, KS).

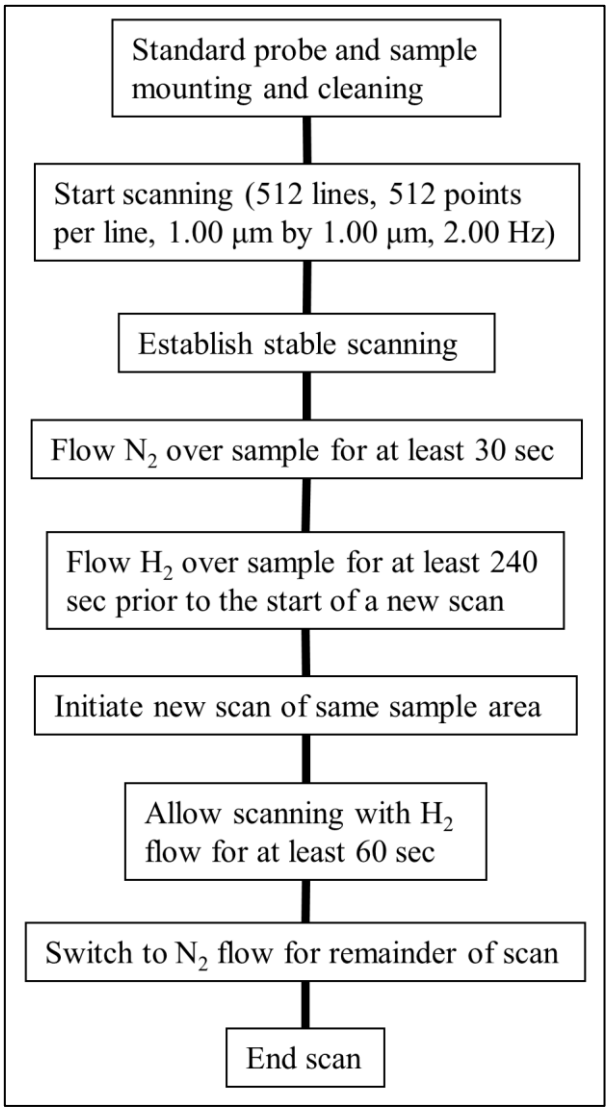

Figure 3.2 - The experimental procedure used for gas-phase AFM experiments.

Figure 3.2 shows the experimental procedure used. At the start of each experiment, the cantilever probe was installed in its holder, rinsed successively with ethanol, toluene, and chloroform, dried under a stream of ultra-high-purity nitrogen for 30 s, and placed in the evacuated desiccator for at least 10 min. Unmodified and sputter-coated PC samples and the Fe sputter target were rinsed with ethanol only, dried under ultra-high-purity nitrogen for 30

seconds, and placed in the evacuated desiccator for at least 10 min. The probe and sample were then installed in the AFM setup. The probe-tracking laser was focused on the probe tip such that the optical signal was maximized with zero deflection indicated. The probe's tapping-mode frequency (always 5% less than the resonant frequency) and drive amplitude were tuned automatically using an IGOR Pro procedure without making contact with the sample. The probe was then lowered to the sample surface until contact was achieved. The scanning set-point voltage and integral gain were determined through multiple quick scans to confirm proper raster scan responses. The dimensions of the scanned area were 1.00 μm × 1.00 μm. Scans were performed with 512 lines and 512 points per line at a scan rate of 2.00 Hz (4 min 16 s per complete scan of the area). Nitrogen was blown over the sample at a rate of 20 mL/s (ambient conditions) through 1/16-in. outside diameter, 0.014-in. wall thickness stainless steel tubing placed perpendicular to the raster scan motions (Figure 3.3) for at least 30 s while scanning proceeded.

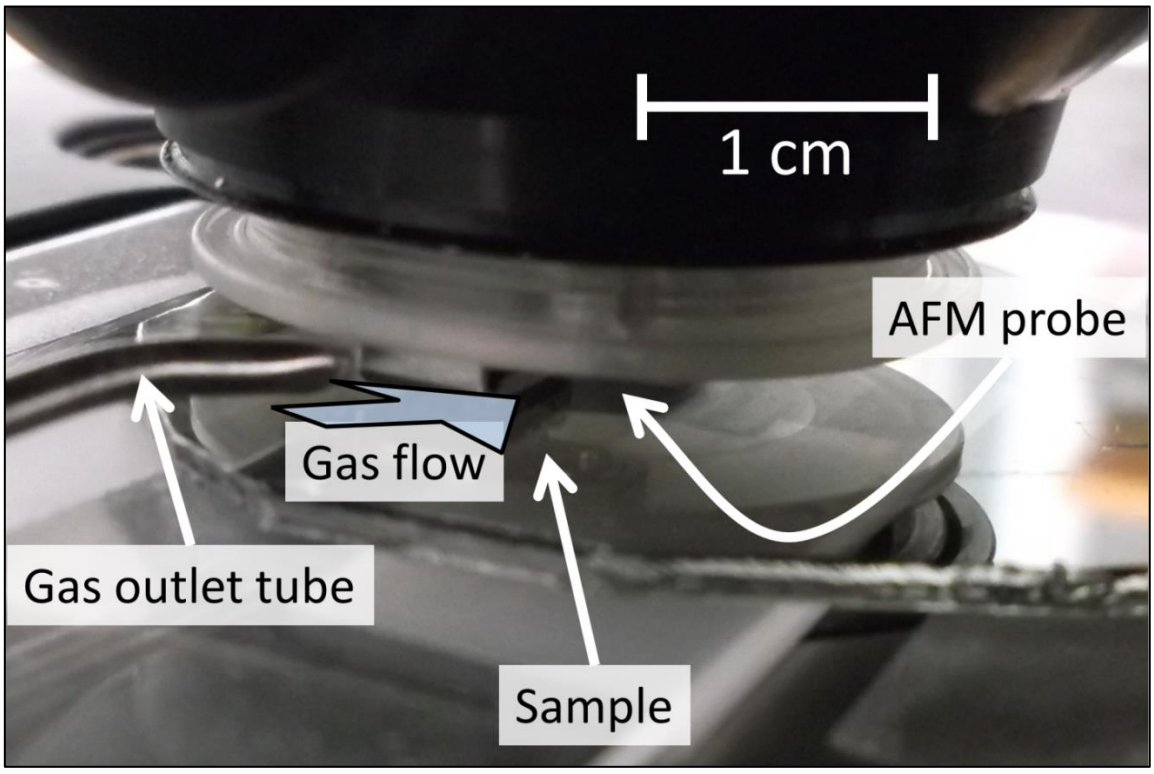

Figure 3.3 - The AFM setup with a Pd sputter-coated PC sample, a gas flow line, and an AFM probe.

The gas flow was then switched to hydrogen (by turning three-way valve V5 shown in Figure 3.4) at a rate of 45 mL/s (under ambient conditions) for at least 30 s before the start of a new scan of the sample area. After a certain period of time had passed during the scan, gas flow was switched to nitrogen to explore the change in signal detected by AFM.

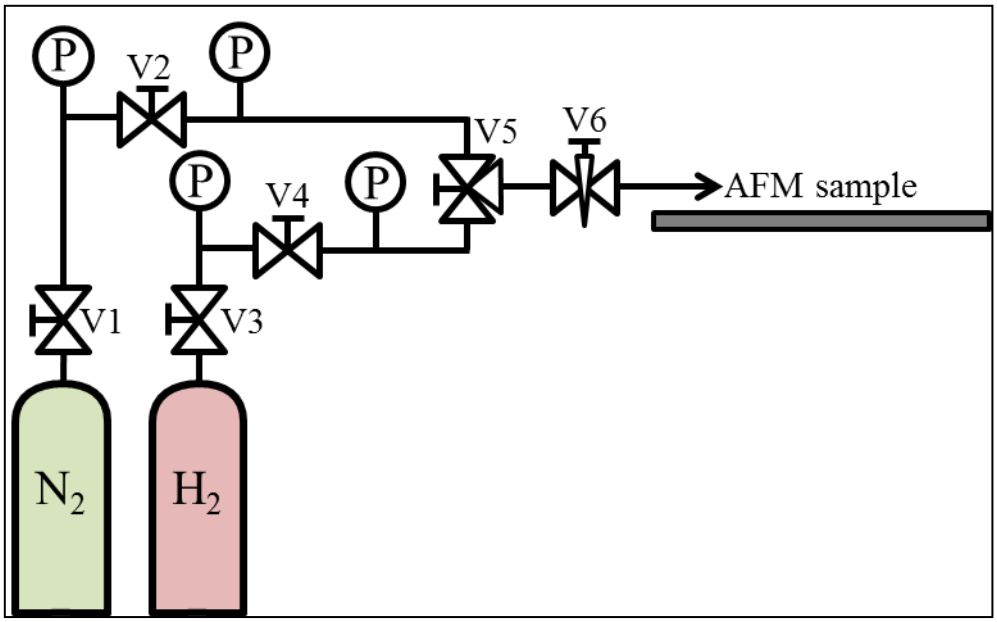

Figure 3.4 - Schematic of the system used to supply flowing gas to the surface of the sample being probed by AFM.

3.3 Results and Discussion

Under ambient conditions, hydrogen has been shown to interact with Pd to form palladium hydride (PdH) by dissociative chemisorption on the Pd.[22,23] The resulting hydrogen ions diffuse into the Pd lattice until reaching equilibrium concentrations of adsorbed and absorbed hydrogen.[24,25] Adsorption of hydrogen onto Fe, in contrast, is limited to low equilibrium surface coverage.[26] Similar low equilibrium hydrogen adsorption is expected for the glassy polymer PC. PC and Fe as non-interacting reference materials and Pd as an interacting material were used to demonstrate phase-angle AFM to detect hydrogen on catalytic surfaces.

Here, the surface of a Pd layer with an estimated total thickness of 12 ± 3.6 nm (based on sputtering parameters[27]) was observed by AFM. Assuming a constant diffusion coefficient of hydrogen[28,29] in Pd of $(2.8 \pm 0.2)\times10^{-7}$ cm^2/s (25 °C), it can be estimated[30] that exposure of the Pd layer to pure hydrogen at atmospheric pressure and room temperature for ~90 s should suffice

for saturation of the Pd with hydrogen (assuming one-sided diffusion into a semi-infinite Pd layer). PC sputter-coated with Pd was exposed to hydrogen at 28 °C and 1 atm for ~4 min (duration of one complete AFM scan of the sample area, 1.00 μm^2). The expected Pd layer volume expansion (perpendicular to the substrate) due to hydrogen absorption at ~3% (~0.36 nm)[24] is undetectable in the topography image. The hydrogen stream blanketing the Pd surface was then exchanged for nitrogen, and it was expected that hydrogen would desorb from the Pd surface until all adsorbed and absorbed hydrogen had vacated the Pd. Complete removal of hydrogen was estimated to take 47 ± 28 s [based on bulk diffusion data (see subchapter 2.4.2)].

As expected, the topographic image in Figure 3.5 shows no detectable change when the gas flow was switched from hydrogen to nitrogen. The topography was generally flat within a 15 nm range with a root-mean-square (*RMS*) roughness (R_{RMS}) of 2.549 nm. The phase angle of the Pd surface after switching from hydrogen to nitrogen exhibited a gradual increase that correlates with an increasingly attractive interaction[9,10] that is attributed to dominant long-range (noncontact) attractive forces between a probe and a stiff material.[31] For this system specifically, the dispersive energy difference was calculated using Equation 3.3.

For this system specifically, the dispersive energy difference was calculated using Equation 3.3 with k = 12.5 eV nm^{-2} (2.00 N m^{-1}), A_t = 6.042 nm, A_0 = 29.99 nm, and Q = 139.84. The arithmetic means of the phase-angle data of the first 60 s and the final 60 s of the scan were 4.28° and 44.9°, respectively, which led to a ΔE_{dis} of 32.1 eV. AFM phase-angle studies of Pd surfaces with and without hydrogen appear to be absent from the literature. Increased attractive forces between the aluminum coating of the cantilever probe's tip and the hydrogen-vacated Pd surface may be reasonable for metal-metal interactions.

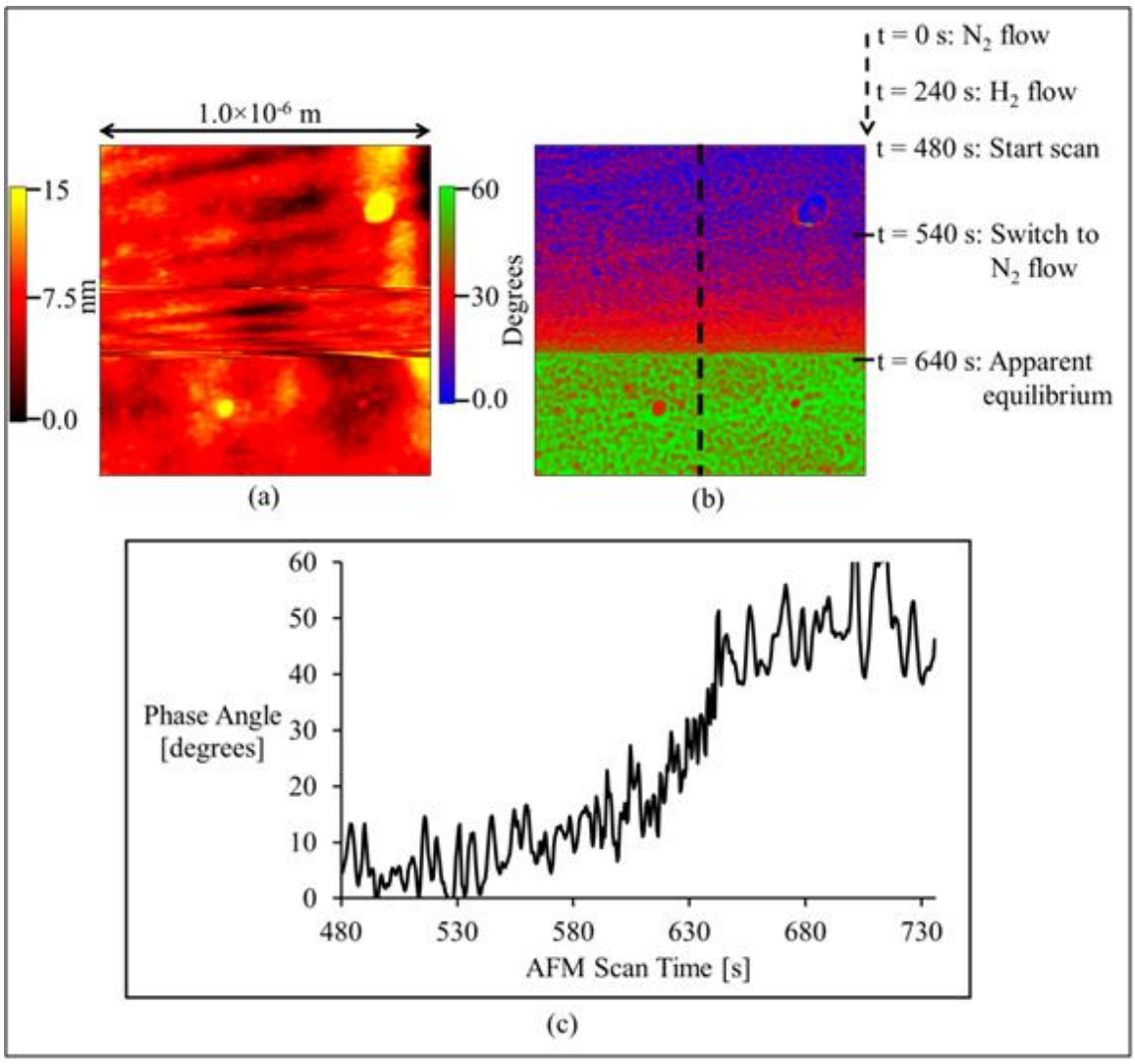

Figure 3.5 - Tapping-mode images of a PC surface sputter-coated with Pd: (a) topography image (R_{RMS} = 2.549 nm), (b) phase-angle image, and (c) phase-angle data along the dotted line in panel b. The scan was initiated with hydrogen gas flowing over the sample before switching to a nitrogen flow at t ~540 s. The gradual phase-angle shift from ~540 s to ~640 s indicates a diminishing amount of adsorbed hydrogen coinciding with a decreased level of hydrogen in the bulk culminating in a hydrogen-vacated surface and bulk material at ~640 s.

The phase angle stabilized about 100 s after the switch from hydrogen to nitrogen, which correlates well with the diffusion-based calculated time for hydrogen removal (above). This agreement between the diffusion-based calculation and the observed change from a lower to higher phase angle provides validation of the AFM approach for the observation of both the presence and absence and the kinetics of hydrogen on a Pd surface under ambient conditions.

Additional figures showing topography, phase angle, and phase-angle vs. time plots for similarly prepared Pd sputter-coated PC samples are available in Appendix 8 to demonstrate reproducibility.

Figure 3.6 summarizes the key steps of the experiment showing an idealized schematic of the adsorbed hydrogen surface concentration, concentration profiles of hydrogen in the polycrystalline Pd film [calculated (see above)], and the AFM phase angle. Analysis of the images indicates a surprising disagreement between the surface hydrogen presence as measured by phase-angle AFM (and depicted in the surface schematic) and that predicted by the bulk diffusion of hydrogen and shown in the concentration profile curves. Specifically, the bulk hydrogen concentration represents a classic single-sided diffusion from a substrate (with negligible mass transfer limitations in the gas phase). In this purely diffusive case, the surface concentration would be expected to equal the concentration at $x = 0$ on the concentration profile, decreasing rapidly with time. In contrast, the phase-angle AFM results indicate that the surface concentration of hydrogen remains largely unchanged until ~135 s into the scan and then depopulates almost instantaneously. These observations are consistent with studies by Ohno et al.[32] that document the presence of multiple populations of hydrogen upon interaction with Pd. Further discussion of this concept follows.

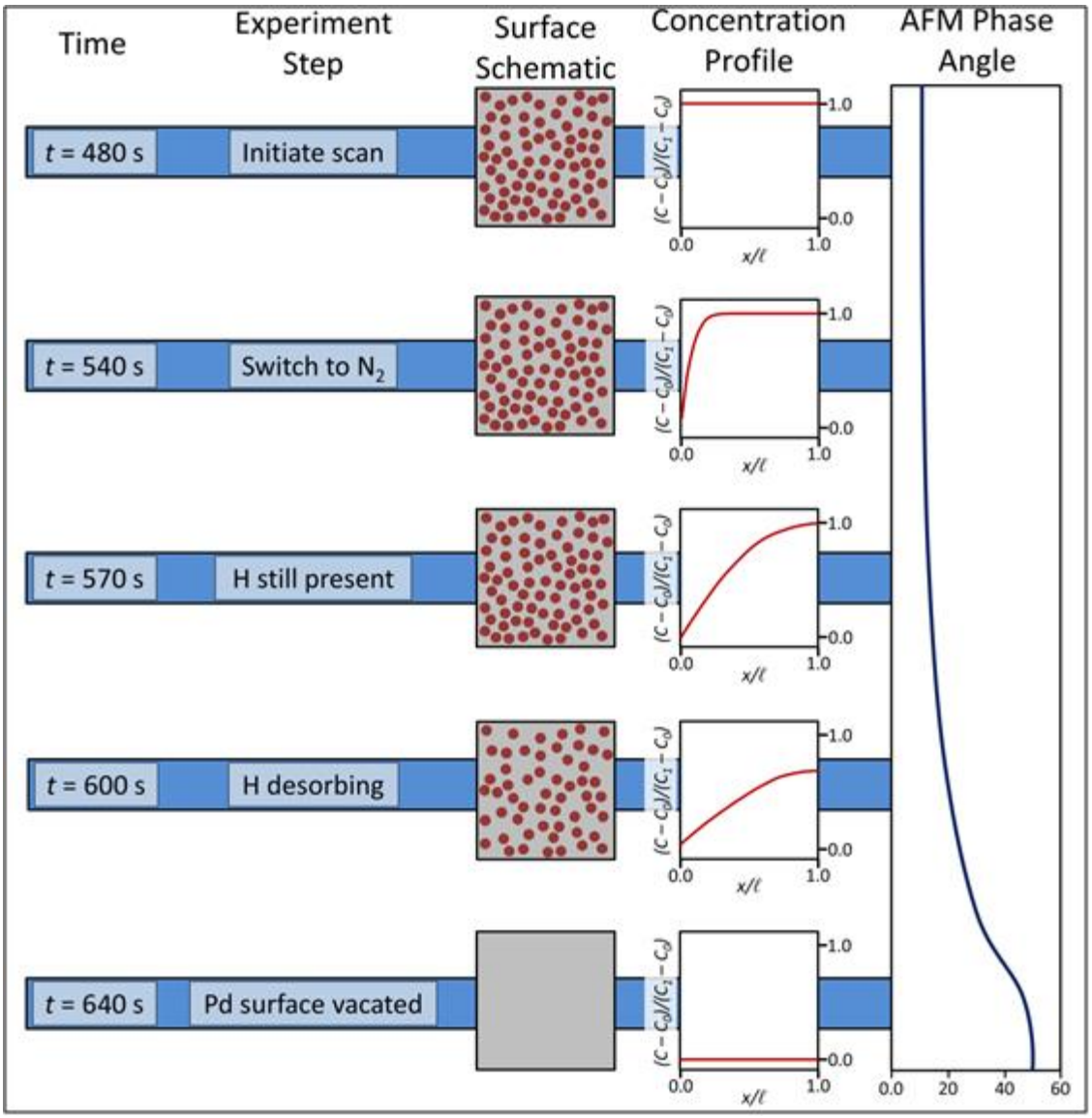

Figure 3.6 - Summarized interpretation of results shown in Figure 3.5. Schematics of the idealized surface, a concentration profile of hydrogen in the polycrystalline Pd film, and the AFM phase angle with corresponding time and experiment steps are shown. The step change in phase angle correlates with the rapid depletion of chemisorbed hydrogen. For the surface schematic, the red dots represent hydrogen ions. For the concentration profile, C is the concentration of hydrogen at x, C_0 is the initial concentration, C_1 is the surface concentration, and x is the depth within the Pd film of thickness l. $x = 0$ represents the gas-solid interface.

For verification of the connection between phase angle and surface composition, two non-hydrogen interacting materials, PC and Fe, were also studied. The topography, phase angle, and

phase angle vs. time plots of PC and Fe surfaces (Figure 3.7 and Figure 3.8, respectively) showed no significant changes in phase angle when the hydrogen flow was switched to nitrogen. This is expected as both materials interact weakly with hydrogen under ambient conditions.

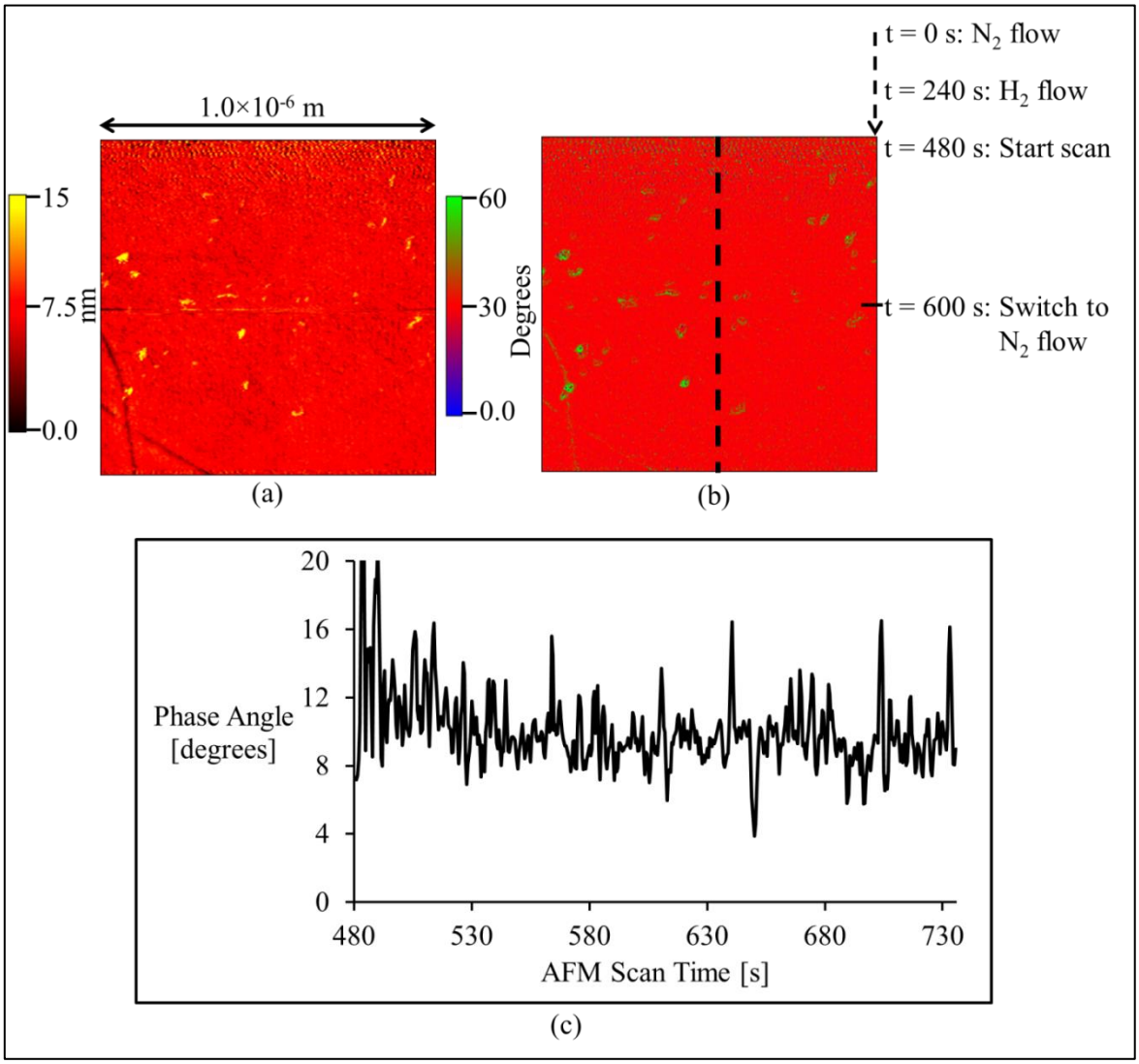

Figure 3.7 - Tapping-mode images of an unmodified PC surface: (a) topography image (R_{RMS} = 1.237 nm), (b) phase-angle image, and (c) phase-angle data along the dotted line in panel b. The gas flow was switched from hydrogen to nitrogen at ~600 s. As expected, exposure to nitrogen or hydrogen did not impact the phase angle because both gases interact weakly with PC.

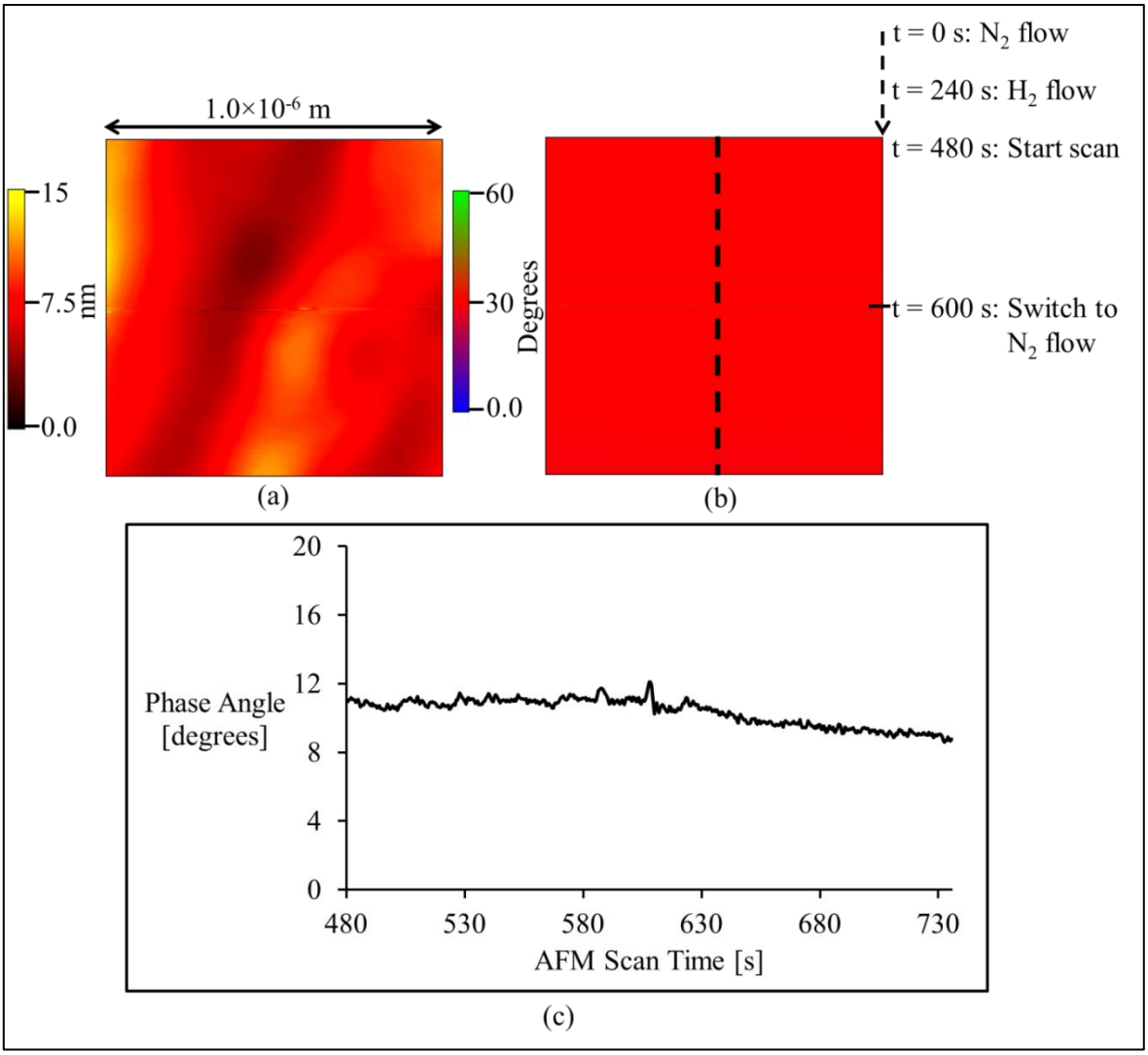

Figure 3.8 - Tapping-mode images of an Fe sputter target surface: (a) topography image (R_{RMS} = 1.940 nm), (b) phase-angle image, and (c) line section of phase-angle data along the dotted line in panel b. The scan was initiated at the top with hydrogen gas flowing over the sample. The gas flow was switched to nitrogen at ~600 s. As expected, exposure to nitrogen or hydrogen did not impact the phase angle because both gases interact weakly with Fe.

One striking feature of the Pd phase-angle image is the presence of a rapid shift in phase angle at ~640 s. The step change likely indicates that the surface is finally free of hydrogen, which can be discerned by the phase-angle data. The virtual step change of the AFM phase-angle (Figure 3.5b) may complement recent work to elucidate the still ill-defined physical processes during sorption of hydrogen from the gas phase into Pd. Using ^{15}N nuclear reaction

analysis (NRA) and thermal desorption spectroscopy (TDS) with surfaces labeled with isotopes (H and D), Ohno et al.[32] report evidence of two different hydrogen populations at or near the Pd surface.

If distinct populations of hydrogen exist in the hydrogen-saturated state of Pd, then hydrogen would be expected to vacate Pd in a non-uniform fashion. This may explain the classical diffusion of hydrogen from the bulk on one hand [with the time scale matching diffusion-based calculations (see above)] while a certain more strongly bound hydrogen population does not depart the surface until the bulk population has been decimated almost completely (step change in the phase angle occurring at ~640 s). It has been established that there are three populations of hydrogen involved in interactions with Pd.[33-35] The first and energetically most stable population is hydrogen ions chemisorbed on the surface. The second and less stable population is near-surface hydrogen, with hydrogen in bulk Pd being the least stable population. Our data provide direct support for these concepts. Specifically, the phase-angle image and phase angle vs. time plot presented in Figure 3.5 and physical interpretation in Figure 3.6 provide direct support for the fact that there are at least two populations of hydrogen: more loosely bound hydrogen in the bulk and strongly bound surface hydrogen that remains until the bulk population is almost completely depleted. Thus, the simple and accessible AFM technique described here allows insights into the intricate interactions of hydrogen and Pd.

3.4 Conclusions

Phase-angle data from AFM imaging of Pd surfaces detects the presence and disappearance of hydrogen in real time, at atmospheric pressure, and at room temperature when the surface is alternatingly exposed to hydrogen or nitrogen. The experimental results correlate well with calculations based on diffusion of hydrogen in Pd. AFM phase-angle data offer an additional approach to the challenge of studying heterogeneous catalysis at metal surfaces both in real time and near common operating conditions. A case study shows a potential parallel of results from the rather accessible technique described here with sophisticated measurements on the fundamentals of the interaction of hydrogen with Pd reported recently.

3.5 References

[1] Ross, J. R. H.; *Heterogeneous Catalysis: Fundamentals and Applications*; Elsevier: Oxford, U.K., 2011; p 172.

[2] Singh, D.; Rezac, M. E.; Pfromm, P. H. Partial Hydrogenation of Soybean Oil using Metal Decorated Integral-asymmetric Polymer Membranes: Effects of Morphology and Membrane Properties. *J. Membr. Sci.* **2010**, *348*, 99-108.

[3] Singh, U. K. ; Vannice, M. A. Kinetics of Liquid-phase Hydrogenation Reactions over Supported Metal Catalysts - A Review. *Appl. Catal., A* **2001**, *213*, 1-24.

[4] Zacher, A. H.; Olarte, M. V.; Santosa, D. M.; Elliott, D. C.; Jones, S. B. A Review and Perspective of Recent Bio-oil Hydrotreating Research. *Green Chem.* **2014**, *16*, 491-515.

[5] Mitsui, T.; Rose, M. K.; Fomin, E.; Ogletree, D. F.; Salmeron, M. Dissociative Hydrogen Adsorption on Palladium Requires Aggregates of Three or More Vacancies. *Nature* **2003**, *422*, 705-707.

[6] Wunder, R. W.; Cobes, J. W.; Phillips, J.; Radovic, L. R.; Lopez Peinado, A. J. Carrasco-Marin, F. Microcalorimetric Study of the Absorption of Hydrogen by Palladium Powders and Carbon-supported Palladium Particles. *Langmuir* **1993**, *9*, 984-992.

[7] Johnstone, R. A. W.; Wilby, A. H. Heterogeneous Catalytic Transfer Hydrogenation and Its Relation to Other Methods for Reduction of Organic Compounds. *Chem. Rev.* **1985**, *85*, 129-170.

[8] James, P. J.; Antognozzi, M.; Tamayo, J.; McMaster, T. J.; Newton, J. M.; Miles, M. J. Interpretation of Contrast in Tapping Mode AFM and Shear Force Microscopy. A Study of Nafion. *Langmuir* **2001**, *17*, 349-360.

[9] Tamayo, J.; García, R. Relationship between Phase Shift and Energy Dissipation in Tapping-mode Scanning Force Microscopy. *Appl. Phys. Lett.* **1998**, *73*, 2926-2928.

[10] Martínez, N. F.; García, R. Measuring Phase Shifts and Energy Dissipation with Amplitude Modulation Atomic Force Microscopy. *Nanotechnology* **2006**, *17*, S167-S172.

[11] Ahn, H.-S.; Chizhik, S. S.; Dubravin, A. M.; Kazachenko, V. P.; Popov, V. V. Application of Phase Contrast Imaging Atomic Force Microscopy to Tribofilms on DLC Coatings. *Wear* **2001**, *249*, 617-625.

[12] Stehlin, F.; Diot, F.; Agnieszka, G.; Dirani, A.; Salaun, M.; Zelsmann, M. Soppera, O. Local Reorganization of Diblock Copolymer Domains in Directed Self-Assembly Monitored by in Situ High-Temperature AFM. *Langmuir* **2013**, *29*, 12796-12803.

[13] Mclean, R. S.; Sauer, B. B. Tapping-Mode AFM Studies Using Phase Detection for Resolution of Nanophases in Segmented Polyurethanes and Other Block Copolymers. *Macromolecules* **1997**, *30*, 8314-8317.

[14] Magonov, S. N.; Elings, V.; Whangbo, M.-H. Phase Imaging and Stiffness in Tapping-mode Atomic Force Microscopy. *Surf. Sci.* **1997**, *375*, L385-L391.

[15] Schmitz, I.; Schreiner, M.; Friedbacher, G.; Grasserbauer, M. Phase Imaging as an Extension to Tapping Mode AFM for the Identification of Material Properties on Humidity-sensitive Surfaces. *Appl. Surf. Sci.* **1997**, *115*, 190-198.

[16] Bhushan, B.; Qi, J. Phase Contrast Imaging of Nanocomposites and Molecularly Thick Lubricant Films in Fagnetic Media. *Nanotechnology* **2003**, *14*, 886-895.

[17] Xu, Z. W.; Liang, Y. C.; Dong, S.; Cao, Y. Z.; Zhao, T. Q.; Wang, J. H.; Zhao, Q. L. Phase Contrast Imaging of SEBS Triblockcopolymer Studied by Carbon Nanotubes Probe. *Ultramicroscopy* **2005**, *105*, 72-78.

[18] Martínez, N. F.; García, R. Measuring Phase Shifts and Energy Dissipation with Amplitude Modulation Atomic Force Microscopy. *Nanotechnology* **2006**, *17*, S167-S172.

[19] Zhao, Y.; Cheng, Q.; Qian, M.; Cantrell, J. H.;Phase image contrast mechanism in intermittent contact atomic force. *J. Appl. Phys.* **2010**, *108*, 094311.

[20] McBride, S. P. Surface Science Experiments Involving the Atomic Force Microscope. Ph.D. Thesis, Kansas State University, Manhattan, KS, 2012.

[21] Bañuls, M.-J.; García-Piñón, F.; Puchades, R.; Maquieira, Á. Chemical Derivatization of Compact Disc Polycarbonate Surfaces for SNPs detection. *Bioconjugate Chem.* **2008**, *19*, 665-672.

[22] Nowakowski, R.; Dus, R. Atomic Force Microscopy Studies of Thin Pd Film Response to Palladium Hydride Formation and Its Reaction with Oxygen. *Langmuir* **2003**, *19*, 6750-6758.

[23] Johansson, M.; Skúlason, E.; Nielsen, G., Murphy, S.; Nielsen, R. M.; Chorkendorff, I. Hydrogen Adsorption on Palladium and Palladium Hydride at 1 bar. *Surf. Sci.* **2010**, *604*, 718-729.

[24] Wicke, E.; Brodowsky, H. Hydrogen in Palladium and Palladium Alloys. In *Hydrogen in Metals II*; Alefeld, G., Völkl, J., Eds.; Topics in Applied Physics; Springer-Verlag: Berlin, 1978; Vol. 29, pp 73-155.

[25] Ackerman, F. J.; Koskinas, G. J. Permeation of Hydrogen and Deuterium Through Palladium-Silver Alloys. *J. Chem. Eng. Data* **1972**, *17* (1), 51-55.

[26] Weatherbee, G. D.; Rankin, J. L.; Bartholomew, C. H. Activated Adsorption of H_2 on Iron: Effects of Support, Potassium Promoter, and Pretreatment. *Appl. Catal.* **1984**, *11* (1), 73-84.

[27] Operating Instructions for Denton Vacuum, LLC DESK II Cold Sputter/Etch Unit and Carbon Evaporation Accessory; Denton Vacuum, LLC: Moorestown, NJ, 1998.

[28] Hironori U.; Tatsuo N.; Isamu U. Electrochemical Measurements of Single Particles of Pd and $LaNi_5$ with a Microelectrode Technique. *J. Electroanal. Chem.* **1995**, *396*, 169-173.

[29] Brass, A. M.; Collet-Lacoste, J. The Influence of Surface on the Permeation of Hydrogen in Iron and Palladium. In *Proceedings of the Symposium on Electrochemical Surface Science of Hydrogen Adsorption and Absorption*; Jerkiewicz, G., Marcus, P., Eds.; The Electrochemical Society, Inc.: Pennington, NJ, 1997; pp 200-210.

[30] Crank, J. The Mathematics of Diffusion; Oxford University Press: Oxford, U.K., 1975; pp 45-68.

[31] García, R.; San Paulo, A. Attractive and Repulsive Tip-Sample Interaction Regimes in Tapping-mode Atomic Force Microscopy. *Phys. Rev. B: Condens. Matter Mater. Phys.* **1999**, *60* (7), 4961-4967.

[32] Ohno, S.; Wilde, M.; Fukutani, K. Novel insight into the hydrogen absorption mechanism at the Pd(110) surface. *J. Chem. Phys.* **2014**, *140*, 134705.

[33] Conrad, H.; Ertl, G.; Latta, E. E. Adsorption of hydrogen on palladium single crystal surfaces. *Surf. Sci.* **1974**, *41* (2), 435-446.

[34] Dong, W.; Ledentu, V.; Sautet, Ph.; Eichler, A.; Hafner, J. Hydrogen adsorption on palladium: A comparative theoretical study of different surfaces. *Surf. Sci.* **1998**, *411* (1-2), 123-136.

[35] Ferrin, P.; Kandoi, S.; Nilekar, A. U.; Mavrikakis, M. Hydrogen adsorption, absorption and diffusion on and in transition metal surfaces: A DFT study. *Surf. Sci.* **2012**, *606* (7-8), 679-689.

4 Experimental Procedures for Dynamic Detection of Hydrogen at Liquid-Palladium Interfaces

4.1 Introduction

The challenge of investigating dynamic processes at liquid-solid interfaces at realistic conditions is significant.[1] AFM was chosen to study hydrogen adsorption and desorption on Pd for its ability to study liquid-immersed surfaces without extreme preparation conditions or experimental conditions. However, the use of AFM for dynamic processes (particularly that study hydrogen adsorption and desorption) is not discussed in the literature. This required the development of new experimental procedures that allow for dynamic studies of diffusion processes by AFM. The procedure initially used often produced results that did not meet criteria for a successful experiment (discussed later in this subchapter). A number of changes were made to the procedure to produce data that were more reliable. These changes and their effects on the quality of the results will be discussed with the aim of aiding future researchers.

The different experiment procedures possessed a number of common attributes among them (AFM setup, application of liquid between the sample and cantilever probe, and the introduction of gas to the sample's surface via diffusion from the opposite side), the differences do require detailed explanation with their results be considered as groups of experiment types. The four different aspects that defined the under-liquid AFM experiments and the number of times each unique procedure was used are detailed in Figure 4.1 . The common attributes of all the under-liquid AFM experiments are described in subchapter 4.3.1, the gas-supply aperture size is discussed in subchapter 4.3.2, the scan speed is discussed in subchapter 4.3.3, the gas purge is discussed in subchapter 4.3.4, and the gas sequence is discussed in subchapter 4.3.5.

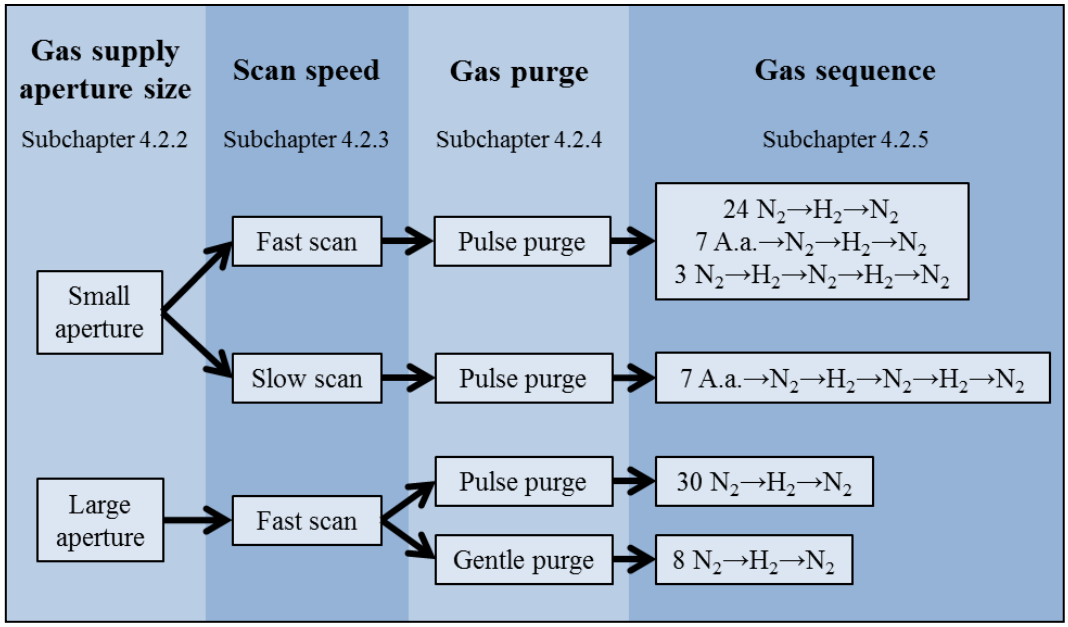

Figure 4.1 - Number of under-liquid AFM experiments performed using each procedure defined by the four different aspects. The subchapter in which each experimental aspect is discussed is also indicated.

4.2 Criteria for Assessing Scan Quality

Two criteria were used to assess the reasonableness of an experiment's results: a smooth phase angle vs. time curve (Figure 4.2) and a relative conformity to the calculated and physically reasonable time scale of the diffusion process.

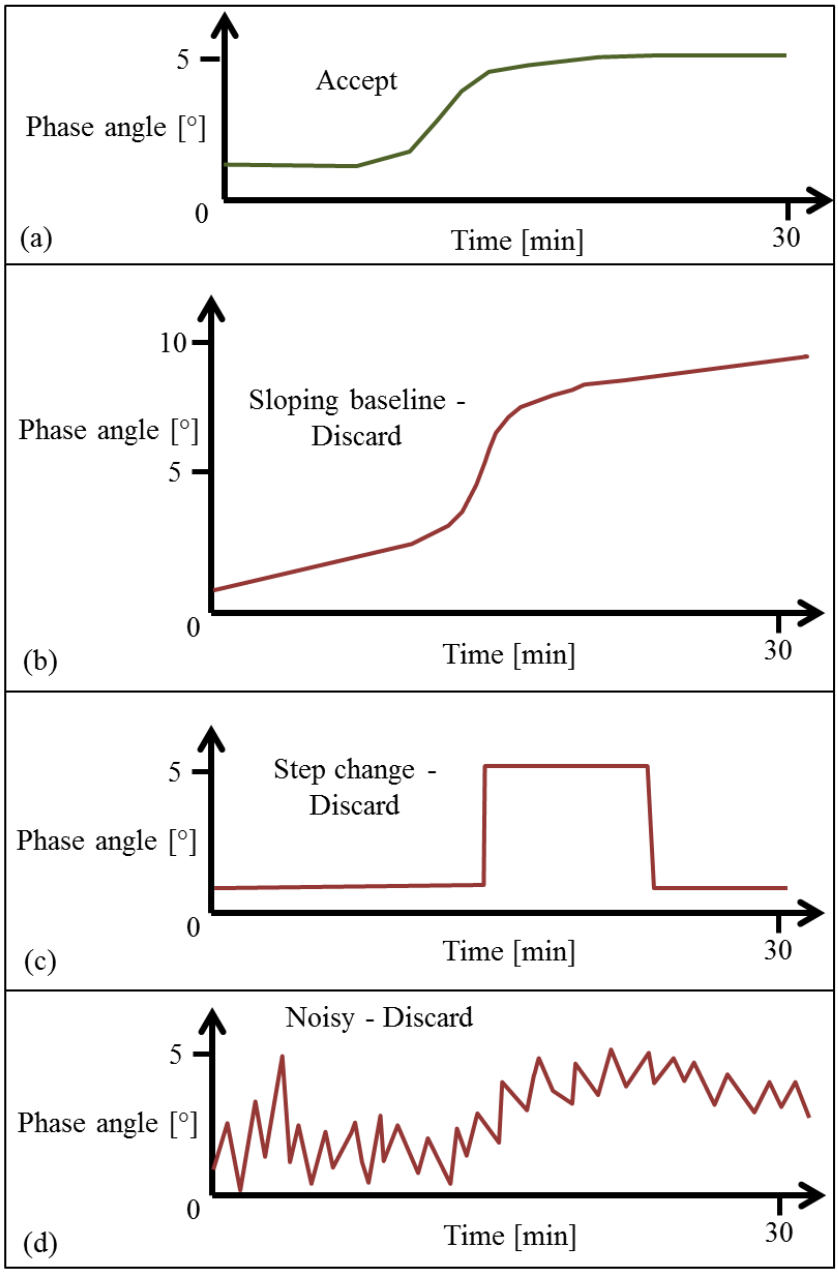

Figure 4.2 - (a) A reasonable linear graph of the phase-angle data from an under-liquid AFM experiment compared to three graphs showing features of questionable scans. These disqualifying features include (b) a sloping baseline that persists when no changes were expected for phase angle, (c) a step change in phase angle especially when not synchronous with an event in the experimental procedure, and (d) sustained noisiness of the phase angle that was on a similar order of magnitude as the overall range of phase-angle results.

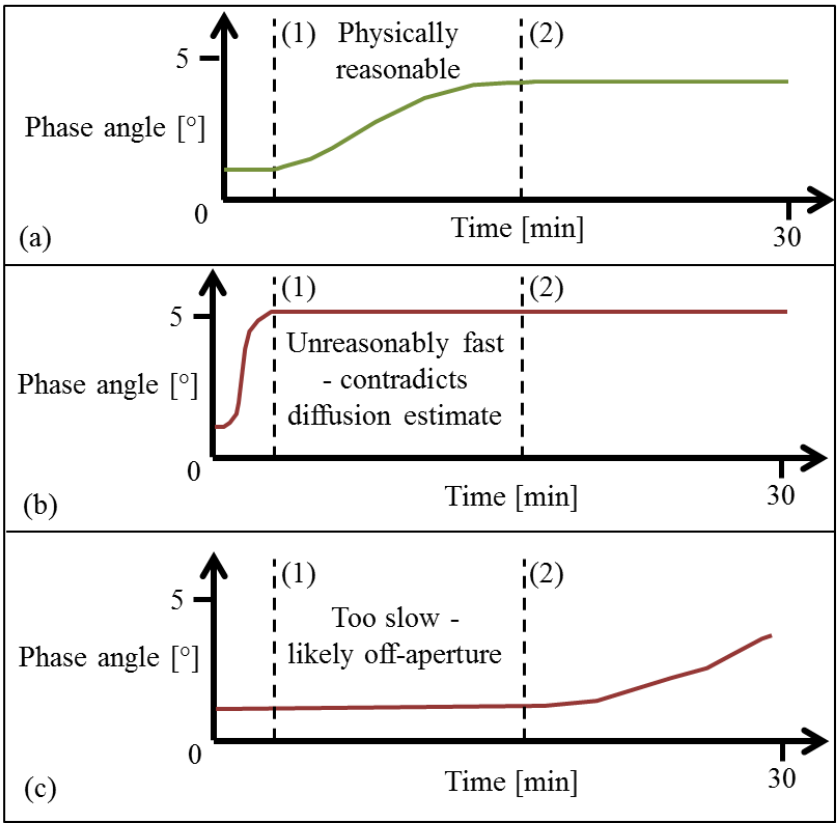

Figure 4.3 - (a) Phase-angle AFM results showing a change in phase angle starting at the estimated time for hydrogen to appear on the surface at (1) until reaching an apparent equilibrium at the estimated time for reaching the maximum concentration of hydrogen on the surface at (2). Disqualifying features for the time scale of phase-angle behavior include changes that are (b) too fast and (c) too slow compared to the diffusion estimates.

The requirement for a smooth data curve was based on the assumption that the surface is homogeneous. Thus, although the probe is constantly changing its position, changes in phase angle were the result of the diffusion of hydrogen to the scanned area. Changes in the surface concentration of hydrogen that lead to changes in the phase angle should be gradual. Obvious questionable features in the phase-angle data such as a sloping baseline, a step change, and a noisy curve are automatically disqualified from the experimental results. The time-scale requirement was based on a calculated hydrogen diffusion time using Fick's second law (subchapter 2.4.3 and Chapter 5). The calculation used thicknesses of the polycarbonate (PC) film, deposited Pd film, and the immersion water layer. If changes in the phase angle occurred at a time about an order of magnitude different from the calculated result, it could be due to defects

in the sample or misalignment of the AFM probe over the gas supply aperture (discussed in subchapter 4.3.2). This also includes results that showed no changes in phase angle. Not only do these issues invalidate the diffusion model used, but also it would be difficult to assess the reasonableness of the acquired results based on the dimensions of the actual sample.

The criteria used to assess scan quality can be summarized:

1. The line-averaged phase angle vs. time curve was smooth
    a. No obviously sloping baseline
    b. No step changes
    c. Noise is negligible compared to the phase angle range
2. Changes in phase angle occurred on a time scale within an order of magnitude of the diffusion estimate
    a. Not too fast, which may imply a defect in the sample
    b. Not too slow, which may imply the probe is not directly above the gas supply aperture

4.3 Experimental Procedures

4.3.1 The Common Features of all Under-liquid AFM Experiments

At least 30 min prior to starting the experiment, the sample was installed in the sample holder (Figure 4.4) using a thin layer of LocTite Quick Set epoxy (Henkel Corp., Rocky Hill, CT 06067) applied to the top of the sample holder where the underside of the PC film would be placed.

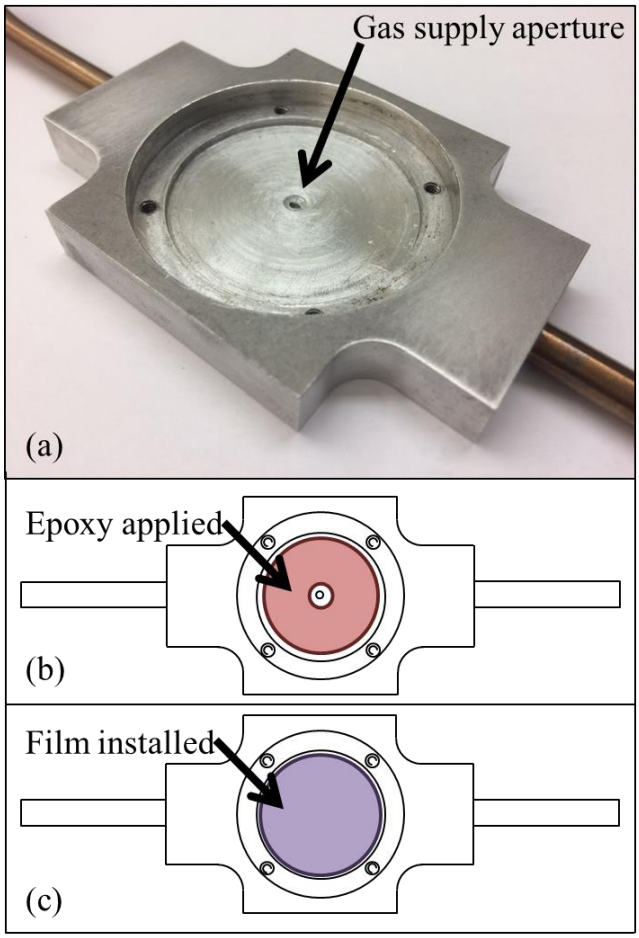

Figure 4.4 - Installation of a polymer film in the sample holder. (a) The clean sample holder surface (b) is coated with a thin layer of epoxy with a hole left around the gas supply aperture and (c) the polymer film is placed on the epoxy.

The area of the film over the small opening in the center of the sample holder was kept free of adhesive. At the start of each experiment, the cantilever probe was installed in its holder, rinsed successively with ethanol, toluene, and chloroform, and dried under a stream of ultra-high purity nitrogen for about 30 s. The AFM probe holder was then installed in the AFM head. The sample was then rinsed with ethanol only and dried under a stream of ultra-high purity nitrogen for about 30 s. The sample holder was then placed on the center of the AFM base and the AFM head with the installed probe holder and probe placed carefully so that the probe was aimed over the small aperture in the sample holder.

Degassed HPLC water was then added over the top of the sample to a depth of roughly 7 mm using the glass syringe. The water layer filled the gap between sample surface and the AFM

probe holder completely. The probe-tracking laser was focused on the probe tip such that the optical signal was maximized with zero deflection indicated. The probe's thermal resonance frequency, drive frequency, and drive amplitude were determined using built-in procedures in IGOR Pro. The AFM head was then lowered until contact between the sample and the probe was achieved. Scanning set-point voltage and integral gain were determined through multiple quick scans to confirm proper topography trace/retrace correlation (Figure 4.5). The set-point voltage is inversely related to the force applied by the probe on the sample while the integral gain relates to the responsiveness of the probe to changes in the surface.[2]

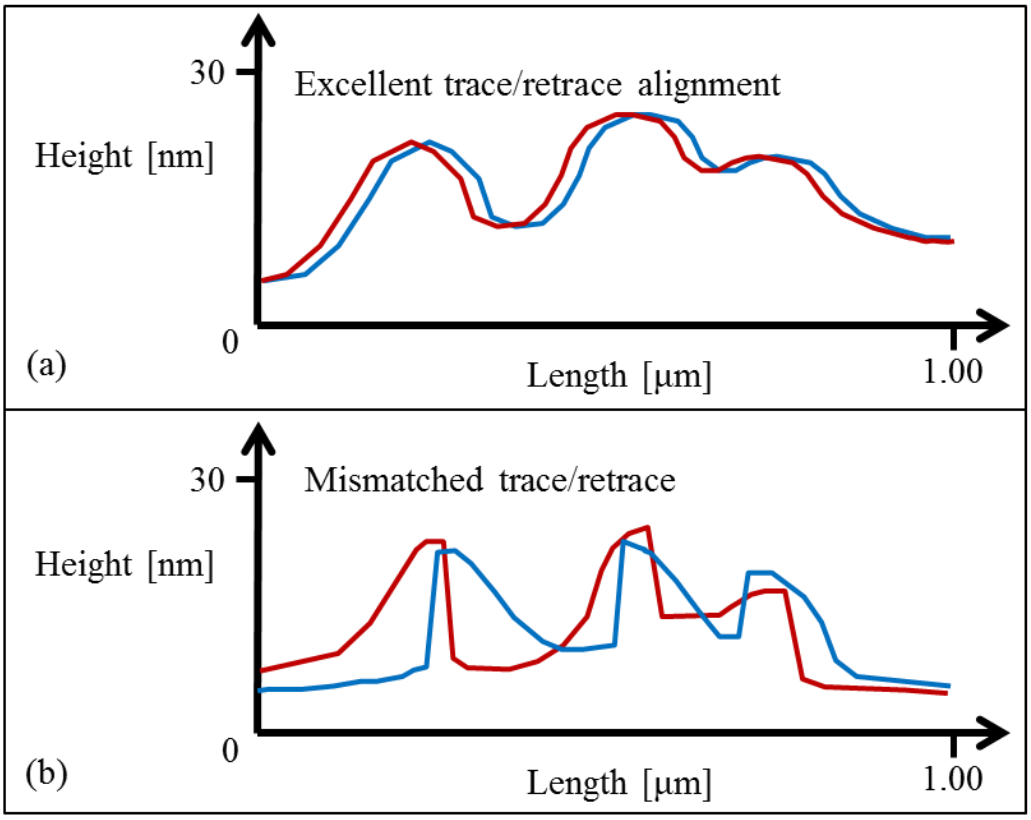

Figure 4.5 - Conceptual trace and retrace data for one AFM scan line. (a) Excellent correlation between trace and retrace indicates proper tracking of the sample surface and (b) poor correlation requires adjustment of the scan settings.

Trace and retrace refer to the first and second lines of scanning the probe follows before moving to a new position. The trace and retrace are always performed over the same position but with opposite directions of scanning. An acceptable scan will exhibit a close alignment

between the trace (the red line in Figure 4.5) and the retrace (the blue line in Figure 4.5). Agreement between the trace and retrace indicates that the probe is accurately tracking the surface. Misalignment of the trace and retrace can usually be corrected by adjusting the set-point voltage. Finding a set-point voltage that results in an acceptable trace-retrace correlation does not follow a guaranteed procedure, but can be done within 10 min of scanning.

4.3.2 Gas Supply Aperture Size

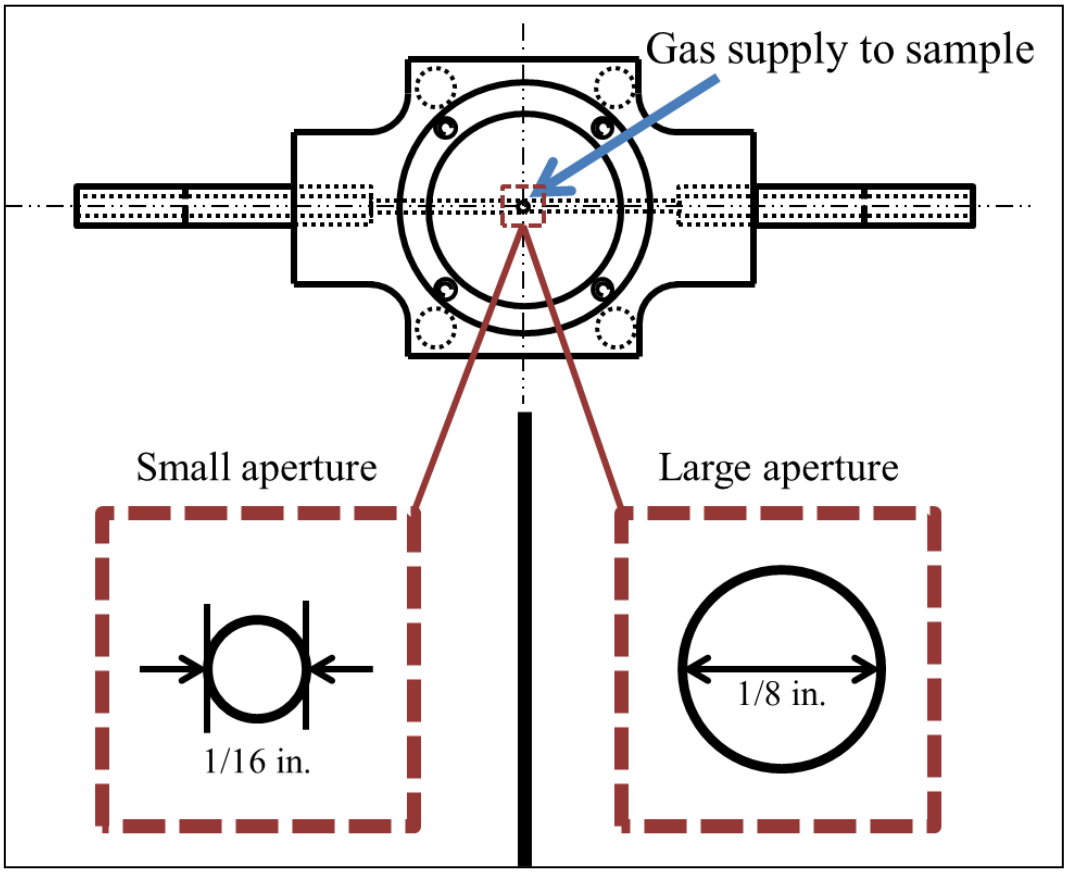

Figure 4.6 - Two sizes of aperture between the gas supply and the AFM sample. Note that the size of the scan area (1.00 μm × 1.00 μm) is too small to be visible on the scale of this illustration.

Hydrogen was supplied to the underside of the sample through an aperture in the sample holder. Measuring the effect of hydrogen concentration on the sample surface using phase angle required that the AFM probe scan over that aperture. Aiming the AFM probe at an area above the open gas supply was not trivial since no system to monitor the relative position of the probe

and sample was available. The probe had to be visually aligned with the aperture although the AFM head obscures the sample surface. Naturally, a larger aperture would alleviate this problem. However, deformation of the sample due to the applied gas pressure would be increased due to the larger unsupported area of the sample.

During the earlier AFM experiments under liquid, the diameter of the gas supply aperture in the sample holder was 1/16 in. (Figure 4.6), large enough to reasonably aim the AFM probe's tip over the aperture. Initially, no results were produced that indicated bad aiming of the probe over the gas supply aperture. However, as more experiments were conducted, a number of the experiments had unexpectedly flat phase-angle results during the allotted scan time. It was reasoned that this could be due to a misalignment of the AFM probe tip with the gas supply aperture of the sample holder (Figure 4.7). According to Fick's second law in one dimension, the time required for hydrogen to diffuse through the sample is related to the square of the sample's thickness. For example, it is estimated that a misalignment of the probe from the gas supply aperture by 1 mm on a sample with a thickness of 0.25 nm increases the time scale of hydrogen diffusion to increase by a factor of about 16. Thus, even a slightly off-aperture probe can increase the likelihood that the scanned area will not achieve equilibrium hydrogen concentration during a single experiment. The gas supply aperture in the sample holder was then doubled in diameter to 1/8 in. to decrease the probability of misaligning the probe.

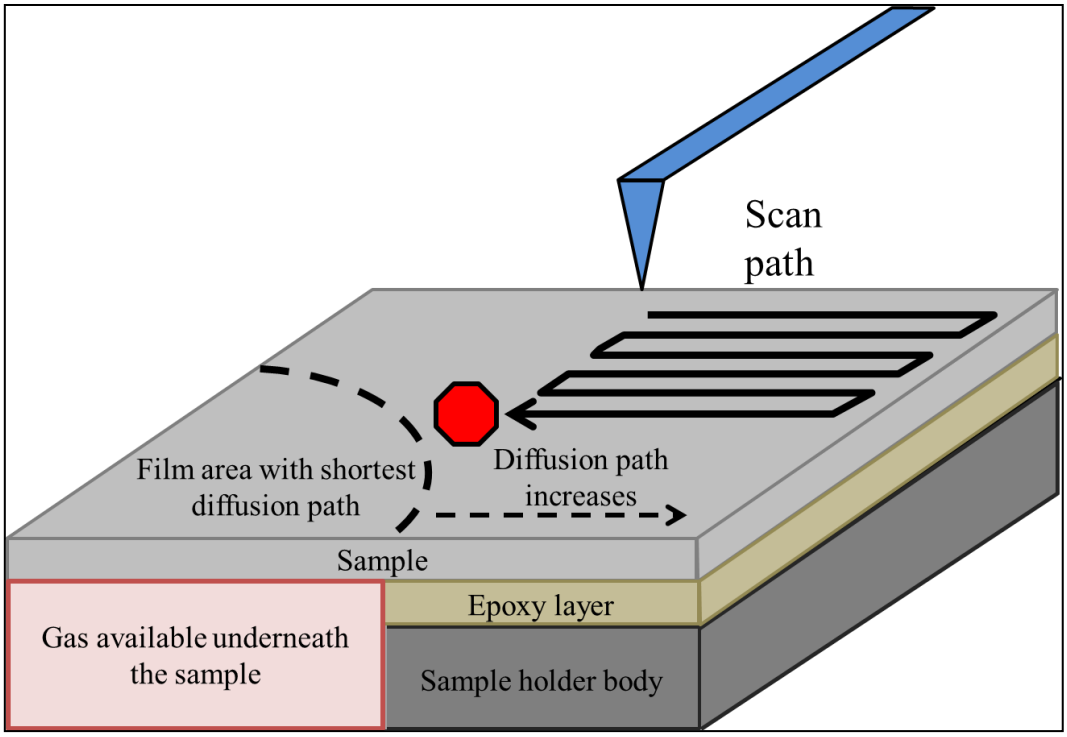

Figure 4.7 - Off-aperture AFM scan. The gas supply aperture and the scan area are not to scale.

Although experiments using the smaller gas-supply aperture often showed results that did not meet the criteria for a good scan, they were at least generally within a reasonable range of phase-angle values of about 5° (Figure 4.8). Doubling the diameter of the gas supply aperture appeared to cause more instability, even for experiments with unmodified PC sample (Figure 4.9). Similarly, the Pd-sputtered PC film experiments with significant phase-angle results were greatly outnumbered by those that did not meet the criteria for good scans (Figure 4.10).

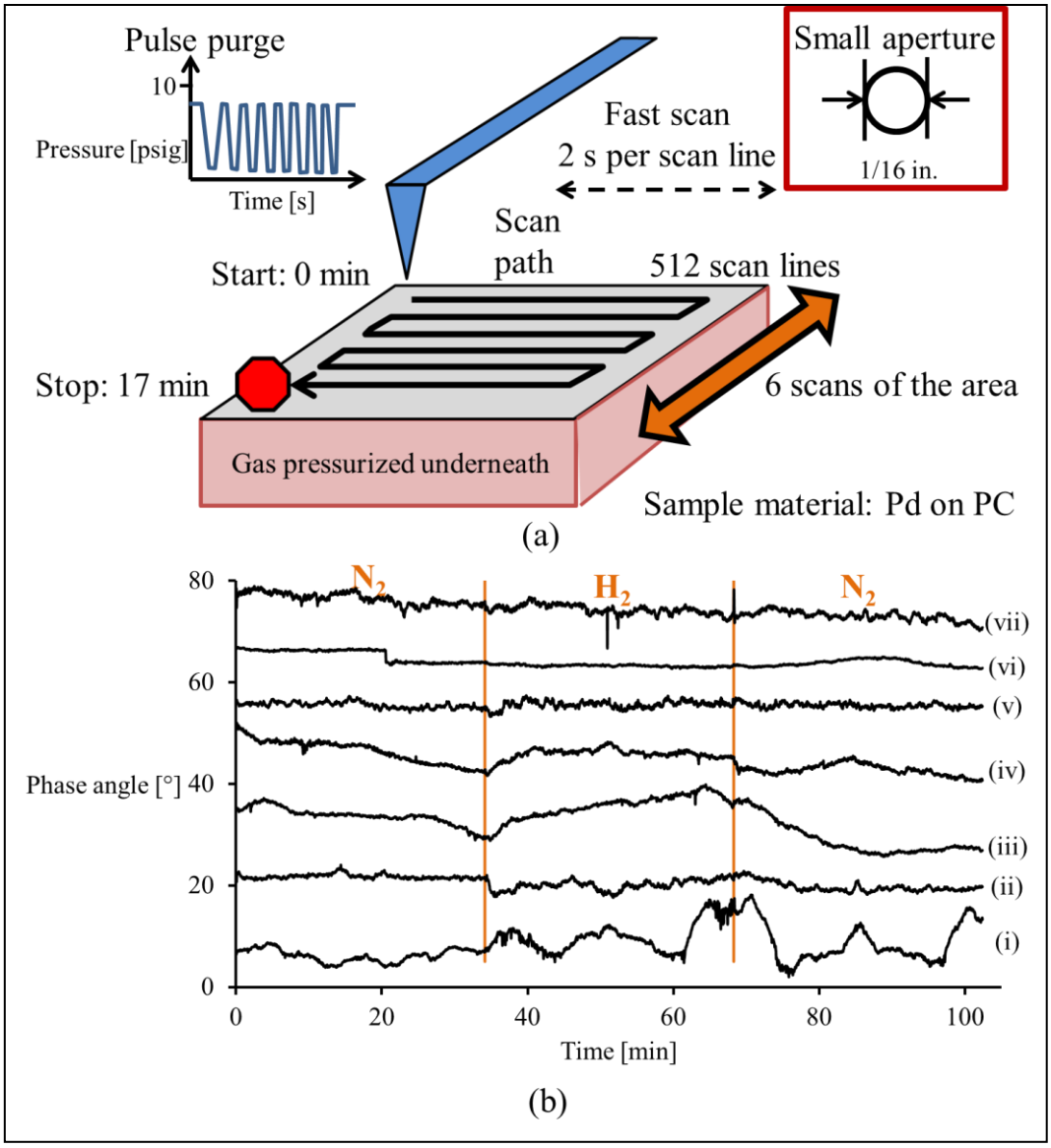

Figure 4.8 - (a) Setup for AFM experiments using pulse purge, small gas-supply aperture, fast scan, and N2→H2→N2 gas sequence and (b) the resulting phase angles. The surface material for all of these experiments was Pd-sputtered PC. The experiments' results were generally featureless, although (iii) and (iv) did show changes in phase angle that resembled expectations.

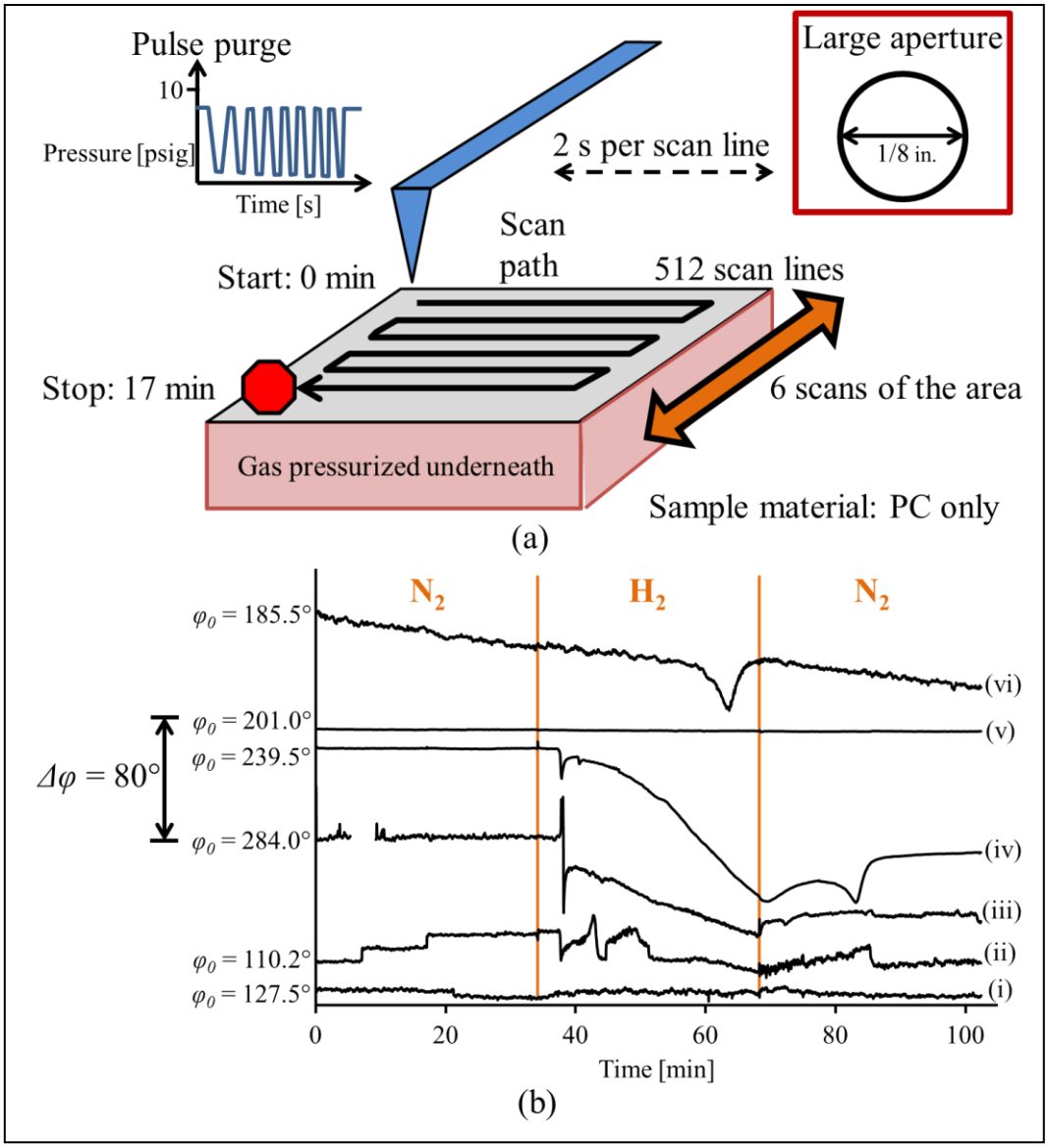

Figure 4.9 - (a) Setup for AFM experiments using pulse purge, large gas-supply aperture, fast scan, and N2→H2→N2 gas sequence and (b) the resulting phase angles. The surface material for all of these experiments was un-modified PC. Only experiment (v) had the featureless response expected for an unmodified PC sample. (i) is similarly featureless, but it is disqualified by the step change that occurred about 21 min into the scan.

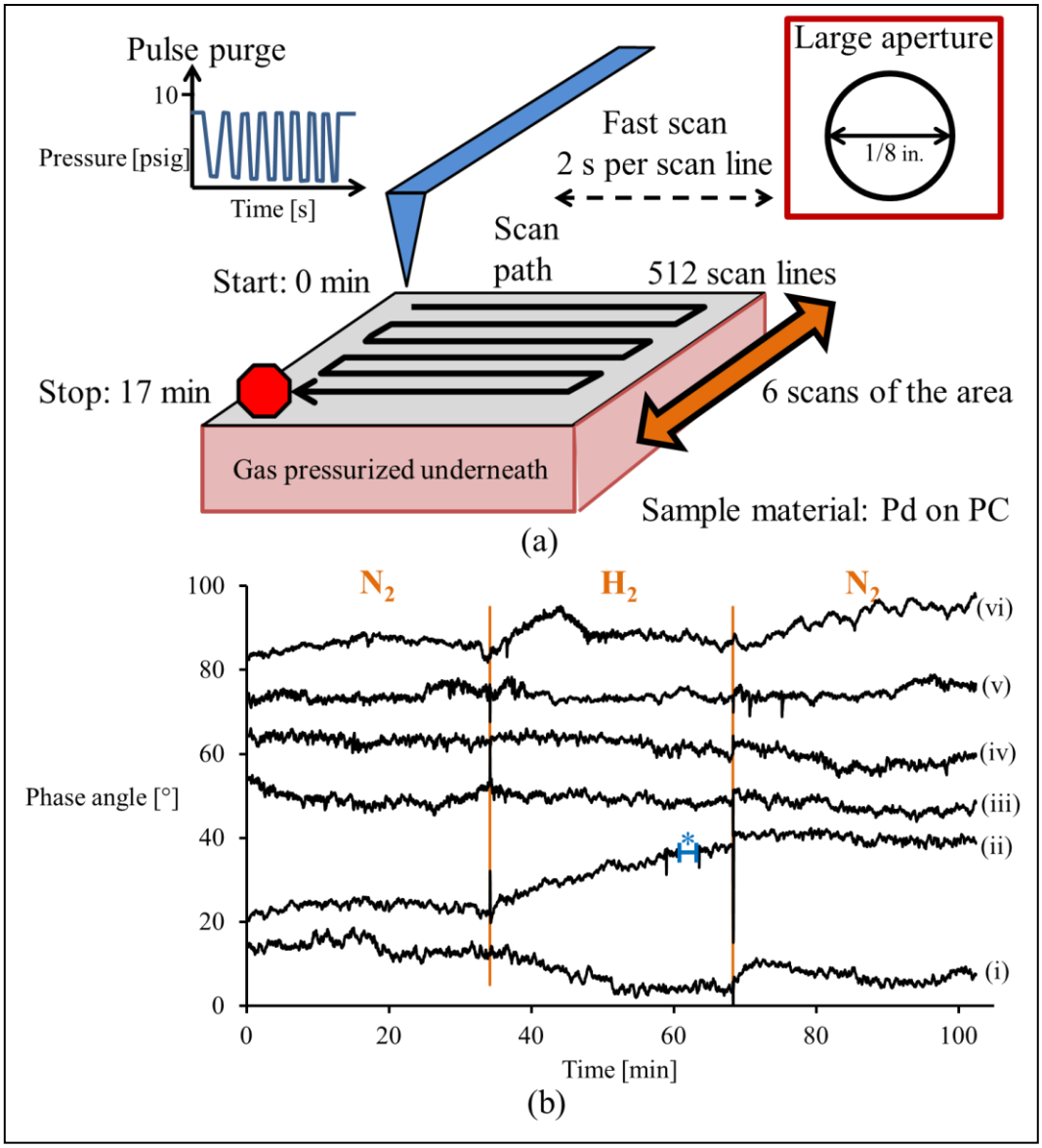

Figure 4.10 - (a) Setup for AFM experiments using pulse purge, large gas-supply aperture, fast scan, and N2→H2→N2 gas sequence and (b) the resulting phase angles. The surface material for all of these experiments was Pd-sputtered PC. Experiment (ii) showed changes in phase angle that were within estimates, but the portion of its curve marked by the blue asterisk was a large spike in phase angle that obscured the other curves.

4.3.3 Scan Speed

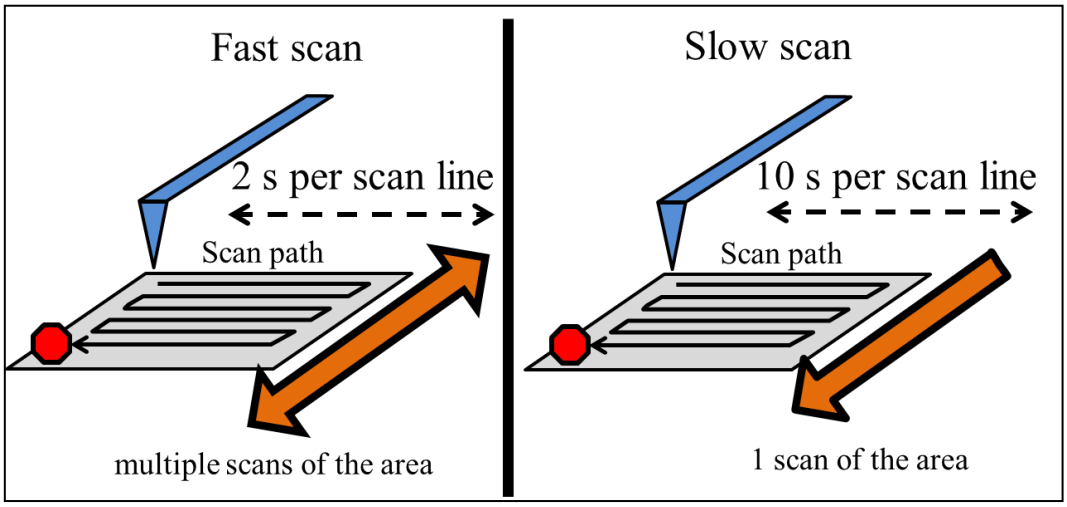

Figure 4.11 - The two scan speeds used.

Two scan speeds were used in the experiments (Figure 4.11). It was found by multiple under-liquid experiments that the scanning speed needed to be decreased from the speed used for under-air experiments to acquire satisfactory results. This is most likely an effect of the higher viscosity of the liquid phase on the AFM probe's movement. A rate of 0.50 Hz (i.e., 2 s to complete one line of the total scan) or lower led to better agreement between the trace and retrace. 0.50 Hz, the faster of the two scan rates, was used for the earlier experiments.

Each gas was available to the sample for two complete scans of the sample area with 512 lines of scanning and 512 points per line at 0.50 Hz. A total scan of the area lasted 17 min 4 s, so each gas was supplied to the sample for 34 min 8 s. The AFM base's positioner would reverse the direction at the end of each scan so that the same area was being probed in all scans.

After a number of experiments with questionable results, the possibility that changing direction between scans negatively affected the results was considered. Therefore, a second method was devised that would allow for nearly equal length of time for each gas to be present under the sample during a single scan. The rate of scanning was decreased to 0.10 Hz (10 s to scan a single line) and the number of points and lines in the scan were increased to 1024 each. Now the time required for the total scan was 2 hr 50 min 40 s. For the first 7 min, only ambient air was present under the sample. Afterwards, the gas under the sample was switched every 33 min.

Changing the scan speed did not completely eliminate phase-angle results that failed to meet the criteria for reasonable scans. However, while the fast-scan experiments showed a variety of problems including baseline shifts and noise (Figure 4.12), the slow-scan experiments showed the most significant results with decreased instability (Figure 4.13). For a number of slow-scan experiments, changes in phase angle commenced when the gas supply was switched. Furthermore, not only would phase angle increase when hydrogen was introduced, but the phase angle decreased when the supplied gas was switched back to hydrogen. This repeatability of the phase angle changes occurred on a time scale that was comparable to the calculations from Fick's second law of diffusion. Overall, the use of slow scans as opposed to fast scans seemed to be the cause of the greatest increase in scan quality. These results are discussed in greater detail in Chapter 5.

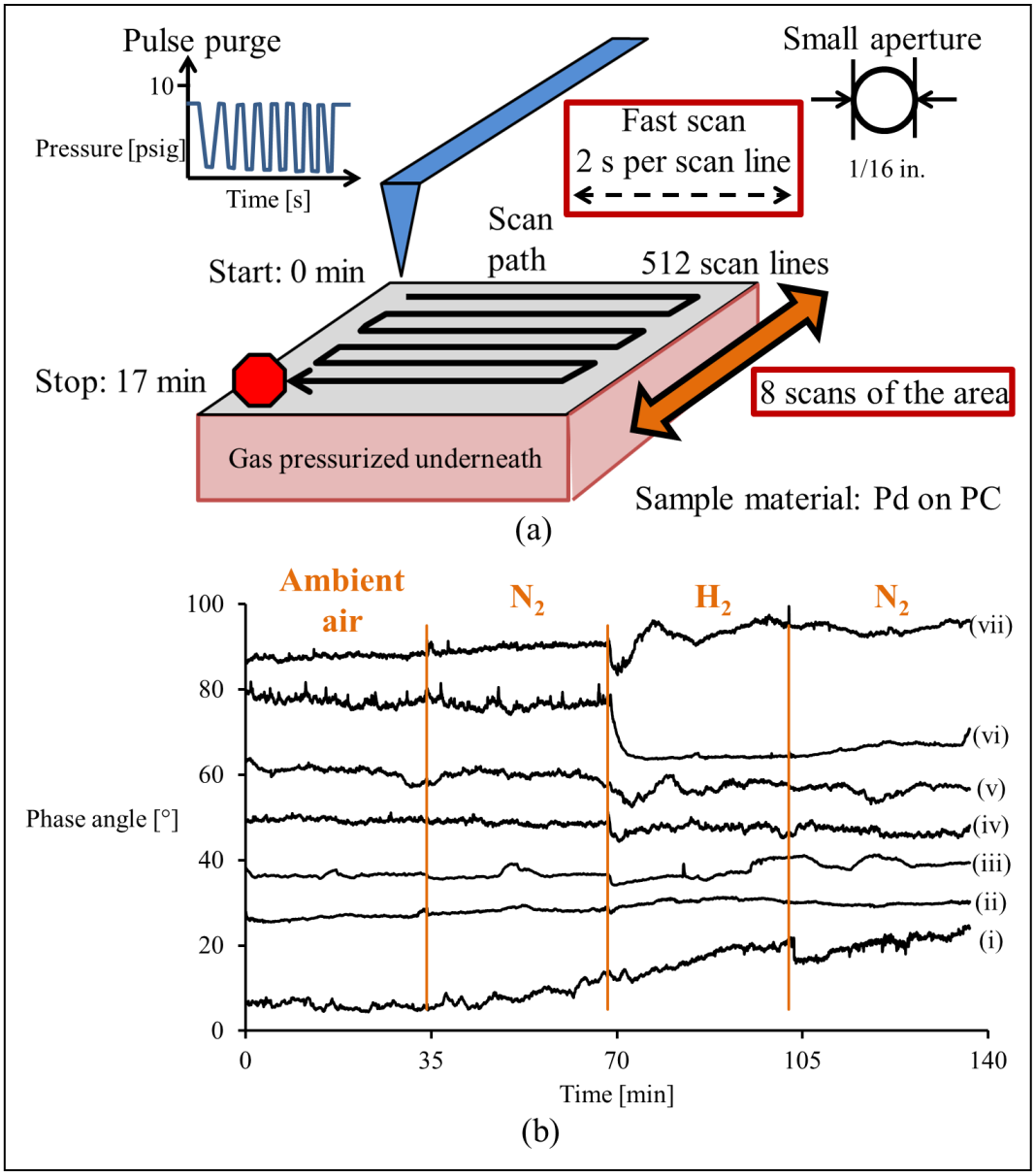

Figure 4.12 - (a) Setup for AFM experiments using pulse purge, small gas-supply aperture, fast scan, and ambient air→N2→H2→N2 gas sequence and (b) the resulting phase angles. The surface material for all of these experiments was Pd-sputtered PC. Experiments (ii), (iii), (iv), and (v) were generally featureless. (i) showed changes in phase angle in the expected direction although the baseline is shifting after 45 min of scanning. (vi) showed a phase-angle change immediately after switching from nitrogen to hydrogen that was in the opposite direction expected for under-liquid experiments. (vii) did show the expected increase in phase angle after switching to hydrogen, but with some erratic behavior.

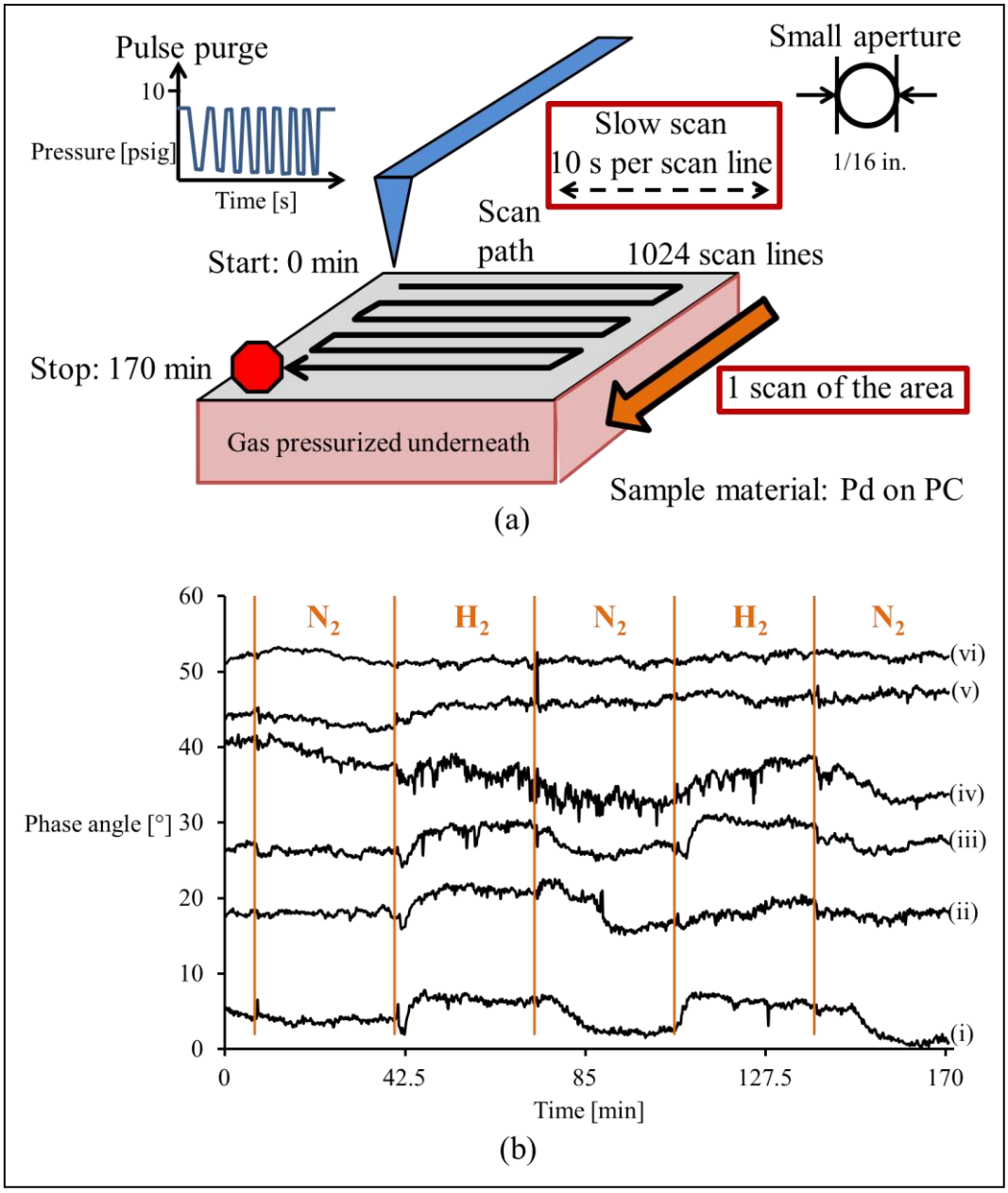

Figure 4.13 - (a) Setup for AFM experiments using pulse purge, small gas-supply aperture, fast scan, and ambient air→N2→H2→N2→H_2→N_2 gas sequence and (b) the resulting phase angles. The surface material for all of these experiments was Pd-sputtered PC. These experiments yielded the most scans with promising phase-angle data. (i) and (iii) are the most interesting as they demonstrate changes in phase angle synchronous with switches in gas that are reversible throughout the experiments. (ii) is similar, although the increase in phase angle is less pronounced during the second hydrogen segment. (iv) showed some responses by the phase

angle to gas switching, but there is a sloping baseline in the early portion. (v) and (vi) were generally featureless.

4.3.4 Gas Purge

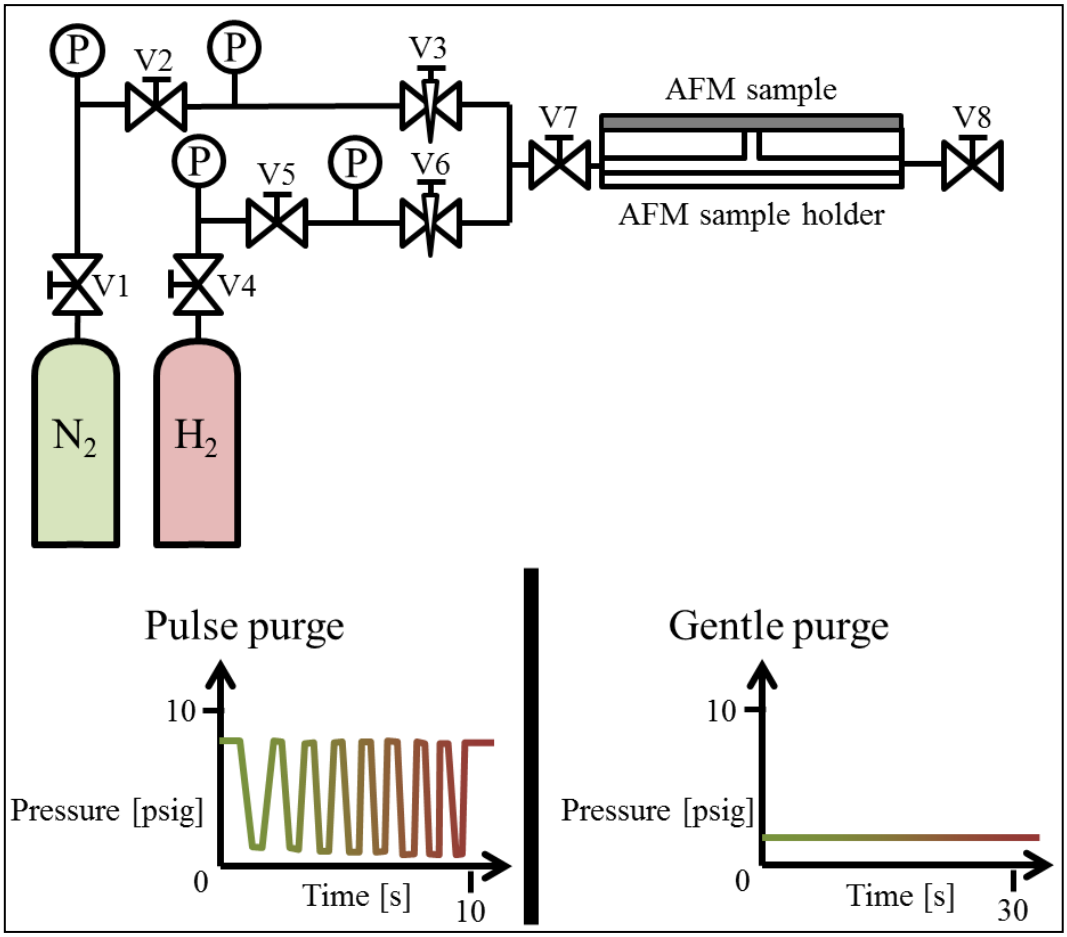

Figure 4.14 - The two procedures to switch the gas during AFM experiments.

The gas provided to the underside of the sample was changed by two different methods (Figure 4.14). The pulse purge procedure (Figure 4.14, bottom left) supplied gas by pressurizing the space between the gas cylinders and ball valve V8. During gas switching, ball valve V8 was quickly opened and closed about 15 times in 10 s allowing the new gas to depressurize and re-pressurize until high gas purity under the sample was achieved.

The gentle purge procedure (Figure 4.14, bottom right) was intended to decrease potential volatility in the experimental results from movement of the sample caused by the pulse purge.

Instead of pressurizing the gas under the sample, ball valve V8 was kept open so that a small flow of gas was detected (estimated to be 0.25 ml/s using a water displacement method). This ensured that 1 atm of gas was available to the underside of the sample and decreased the likelihood of the sample deforming due to the gas pressure. The gas supply to the AFM sample holder was changed upstream and the new gas flow allowed high gas purity to be achieved.

Changing the gas purge procedure did not appear to increase the stability of the phase-angle results. Comparison of data from experiments using pulse purge (Figure 4.15) and gentle purge (Figure 4.16) showed that both methods had results that failed to meet the criteria for good scans. The pulse purge experiments tended to have greater noise, but also failed to show changes on a reasonable time scale. One of the experiments with unmodified PC was particularly extreme with step changes and noise which is far from the nearly featureless results expected due to PC's relative non-interaction with hydrogen. The gentle purge showed one featureless phase-angle result for an experiment with unmodified PC, but other experiments showed baseline shifts and noise. Thus, the purge procedure does not seem to strongly impact the quality of phase-angle results.

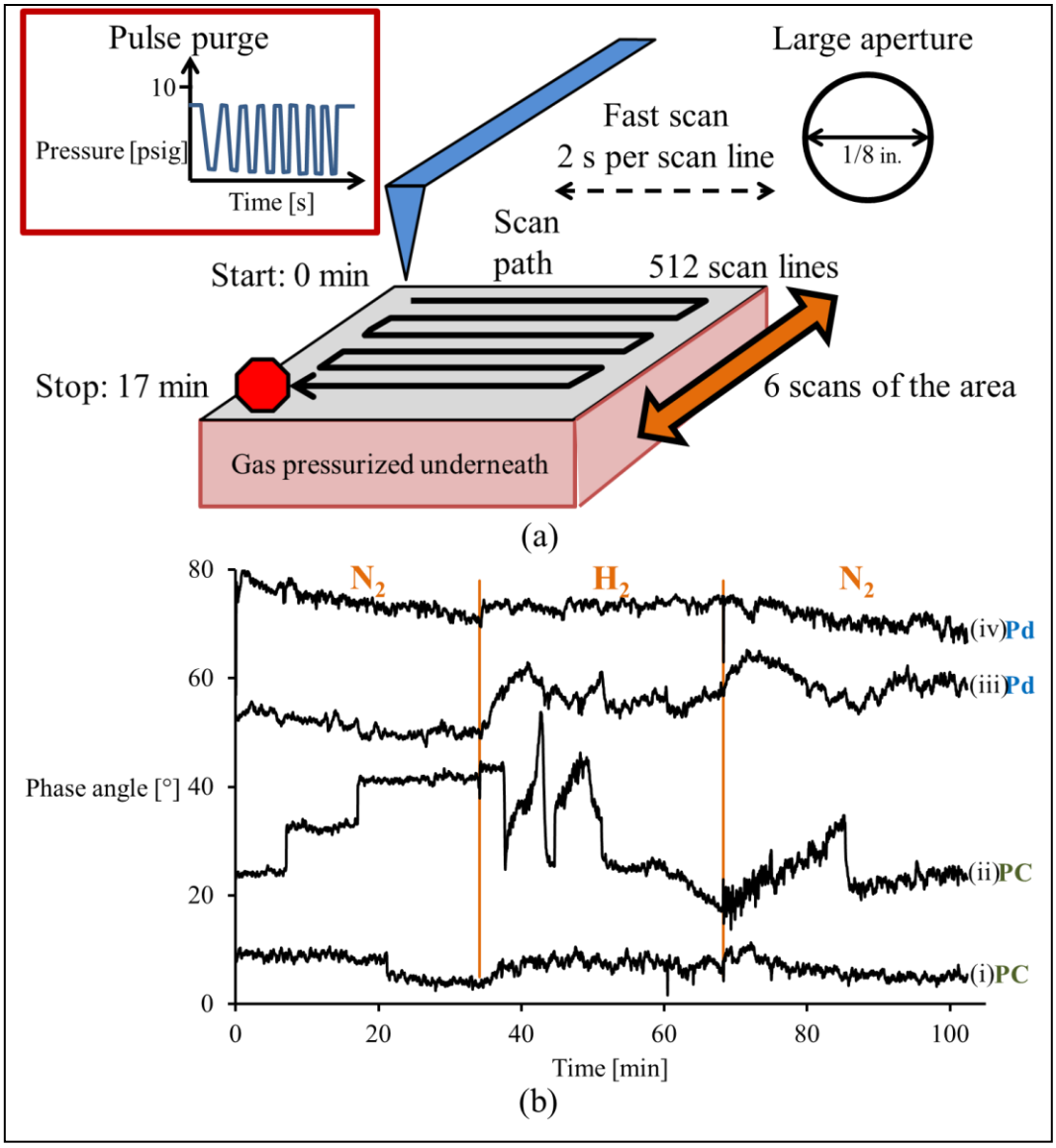

Figure 4.15 - (a) Experimental procedure used (pulse purge, large gas-supply aperture, fast scan, $N_2 \rightarrow H_2 \rightarrow N_2$) and (b) the resulting phase angles. The surface material (Pd or PC) of the sample is labeled to the right. Unmodified PC experiments (i) and (ii) demonstrated step changes while Pd experiment (iv) was generally featureless. (iii) did show some changes in phase angle, but they are not uniform within each gas segment.

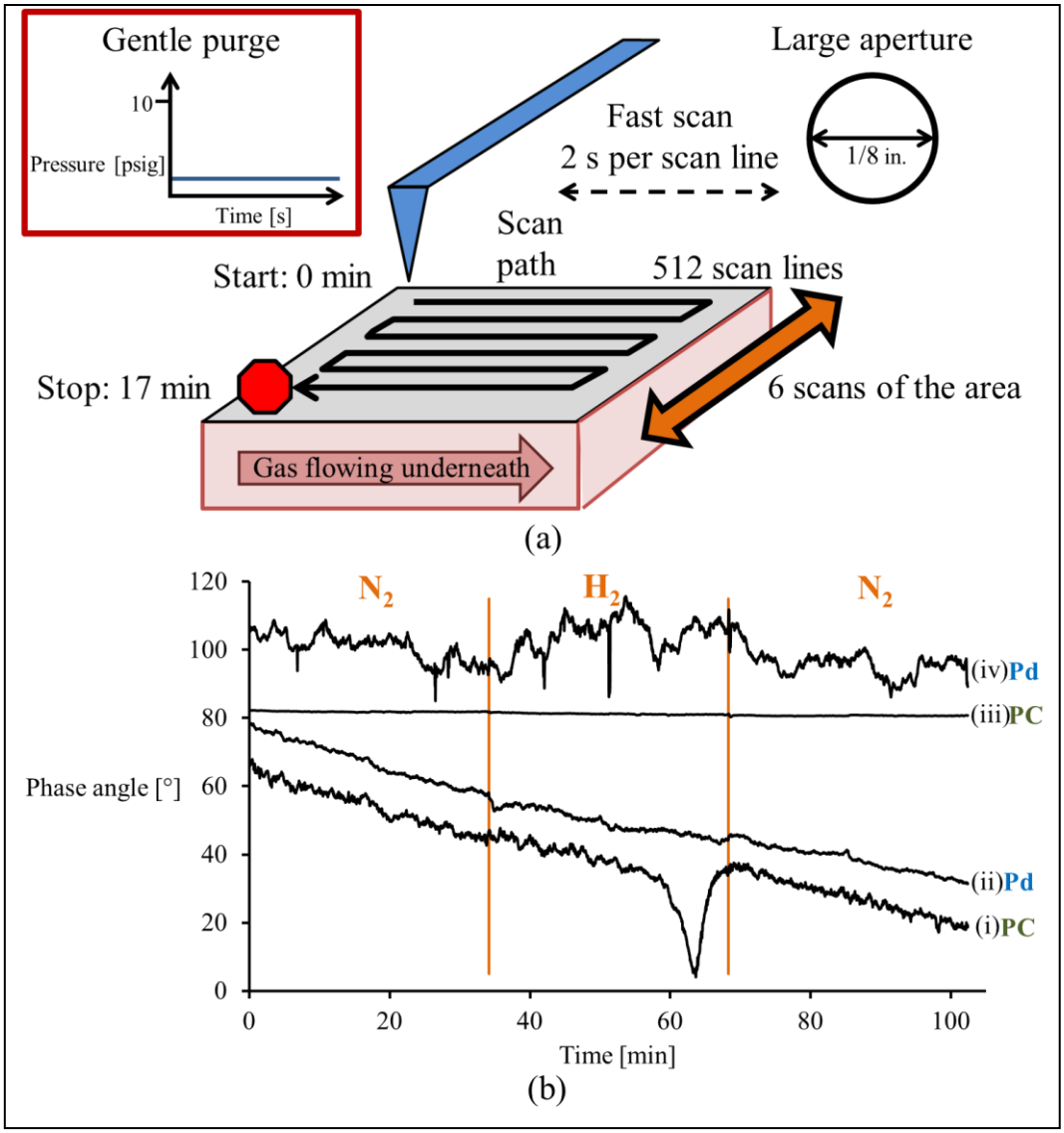

Figure 4.16 - (a) Schematic illustrating the experimental setup used (gentle purge, large gas-supply aperture, fast scan, $N_2 \rightarrow H_2 \rightarrow N_2$) and (b) the resulting phase angles. The surface material (Pd or PC) of the sample is labeled to the right. Unmodified PC experiment (iii) yielded the expected featureless phase-angle result. Both (i) and (ii) showed sloping baselines for the full duration of the experiments. (iv) was dominated by noisy responses throughout.

4.3.5 Gas Sequence

The final distinguishing feature of the under-liquid AFM experiments was the sequence of gases. It was initially decided that a simple nitrogen-to-hydrogen-to-nitrogen cycle ($N_2 \rightarrow H_2 \rightarrow N_2$) would be used. Next, another segment with ambient air under the sample was

added to this sequence (ambient air→N_2→H_2→N_2). This allowed for a direct comparison between results during periods of high-purity gas availability and ambient conditions. The next cycle included additional nitrogen and hydrogen segments (ambient air→N_2→H_2→N_2→H_2→N_2). Finally, a similar cycle without the initial ambient-air segment was used (N_2→H_2→N_2→H_2→N_2).

The addition of an ambient air segment was to test whether the mechanical effects of the gas changed in phase angle. Similarly, the additional hydrogen and nitrogen gas segments tested the reproducibility of changes in phase angle when the gas was switched. The sequence of gases did not seem to have an effect on the quality of phase-angle results through the mechanical effects of the gas. Furthermore, the expected reversibility of phase angle changes as a response to gas switching was observed for multiple experiments as shown in Figure 4.13.

4.4 Conclusions

Among the four aspects of the under-liquid AFM experiments that were changed, the scan speed seemed to have the largest impact on the quality of the results. The gas purge procedure and the size of the gas-supply aperture did not seem to affect the results significantly. It must be noted that slow-scan experiments were conducted using only pulse purge and the smaller gas-supply aperture, so the impact of a gentle purge and larger aperture could still be explored. Still, the slow scans yielded phase-angle results that are useful for analysis.

- The slow-scan procedure yielded the most successful scans.
- The gas purge procedure and gas supply aperture size had minimal effect on quality.
- The effect of a gentle purge and larger gas supply aperture combined with a slow scan remains unexplored.

Chapter 5 of this dissertation will focus on the slow-scan results (including those shown in Figure 4.13) to demonstrate the usefulness of AFM phase angle for assessing the presence or absence of adsorbed hydrogen on Pd.

4.5 References

[1] Zaera, F. Probing Liquid/Solid Interfaces at the Molecular Level. *Chem. Rev.* **2012**, *112*, 2920-2986.

[2] Fuierer, R. (Asylum Research, Procedural Operation 'Manualette' Beta Version 10, Based on software version 080501, 2008).

5 Dynamic Detection of Adsorbed Hydrogen on a Catalytic Surface Under Liquid[2]

5.1 Motivation

Dynamic observation of hydrogen on catalytic metal surfaces is a challenging aspect of studying liquid-phase heterogeneous catalysis. Current methods suffer from one or more of the following limitations: the requirement to observe the surface in high vacuum, the inability to provide nanometer-level spatial resolution, the inability to deal with opaque catalysts and/or liquid phase, the lack of real-time scanning of the surface area, and the inability to assess pronounced topographies and mixed materials. Atomic force microscopy (AFM) provides an opportunity for direct observation of catalyst surfaces at or near actual reaction conditions and under opaque or transparent liquid.

Hydrogen was delivered to a palladium surface immersed in water by diffusion through a polycarbonate film supporting the palladium. The palladium surface was continuously probed by AFM. The theoretically predicted time-dependent appearance of hydrogen on the water-covered palladium surface matched the experimental observation reasonably well. The technique demonstrated here is unique in that the appearance of hydrogen is dynamically detected in real time on a catalyst surface immersed in water. Simultaneous observation of the nanoscale topography is an added benefit. The results presented here supply a new level of information for heterogeneous catalysis that is not available with existing techniques. The work presented here opens new avenues in the study of heterogeneous catalysis, a field of tremendous practical importance and serious analytical challenges.

5.2 Introduction

AFM at realistic conditions of high pressure and temperature for catalysis has recently attracted interest.[1] The use of tapping mode explored here, however, has not been reported for this problem and is currently not a well-known tool.[1] Continuing technological improvements may increase future prospects for tapping-mode AFM at realistic practical catalysis conditions of up to several hundred °C, and several atmospheres.[2]

[2] The majority of the material in this chapter will be used in a journal article to be submitted to *Ultramicroscopy*.

It is demonstrated here that AFM phase-angle data can be used to observe the dynamic adsorption of hydrogen on a Pd surface at room temperature and immersed in water (Figure 5.1). The magnitude of the phase angle between input (tip oscillation) and output (tip oscillation) will change when hydrogen appears on the surface. The technique demonstrated here may enable further insights into real-time mass transfer, kinetics, and directly observe appearance and disappearance of materials during heterogeneous catalyzed reactions. This may enable improved design of conventional catalysts and catalytic membranes.

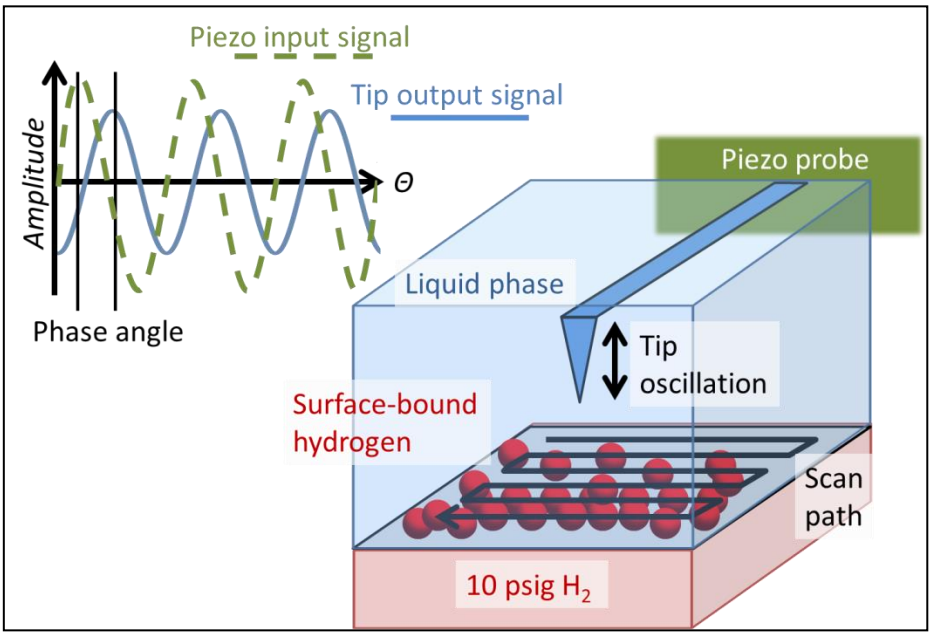

Figure 5.1 - Phase-angle AFM for detection of adsorbed hydrogen on a surface immersed in liquid.

5.3 Theory

The experiments described below were benchmarked against mass-transfer calculations based on the geometry and material-specific hydrogen diffusion- and sorption coefficients of the samples. These calculations shown below predict the time interval required for hydrogen to appear on the scanned area of the Pd surface and then to approach equilibrium. The solubility of hydrogen in polycarbonate (PC) and the permeability of hydrogen in water were calculated based on the equation relating permeability, diffusivity, and solubility[3]

$$P = DS \qquad \text{Equation 5.1}$$

where P [Barrer = 10^{-10} (cm^3(STP) cm)/(cmHg s cm^2] is permeability, D [cm^2/s] is the diffusion coefficient, and S [cm^3(STP)/(cm^3 cmHg)] is solubility. Table 1 shows the data used in these calculations. Mass transfer by diffusion governs the time from supplying hydrogen to the underside of the Pd-sputtered PC films to the first appearance of hydrogen at the Pd-water interface. The very high hydrogen permeability of Pd relative to PC or water suggests that any hydrogen thermodynamic activity at the PC-Pd interface is essentially the same at any time as the thermodynamic activity at the Pd-water interface.

Table 1 - The permeabilities, solubilities, and diffusion coefficients of PC, Pd, and water used for mass transfer calculations. References are given in square brackets. Where no reference is indicated, the parameter was calculated from literature values and Equation 5.1.

Material	H_2 permeability [Barrer]	H_2 solubility [cm^3(STP)/(cm^3 cmHg)]	H_2 diffusion coefficient [cm^2/s]
Polycarbonate	1.2×10^{1} [4]	2.6×10^{-4}	$4.35 \pm 2.65\times10^{-6}$ [5,6]
Palladium	3.3×10^{2}	1.2×10^{-1} [7]	$2.8 \pm 0.2\times10^{-7}$ [8,9]
Water	1.21×10^{2}	2.52×10^{-4} [10]	$4.80 \pm 0.52\times10^{-5}$ [10]

One-sided hydrogen diffusion through the sample can be analyzed in detail based on a second-order diffusion model.[11] This model is most useful for films with homogeneous compositions. However, the thickness of the PC layer is over 21,000 times greater than the thickness of the Pd layer while the two layers' diffusion coefficient differ only by one order of magnitude (Figure 5.2a). The time for one-sided diffusion through a plane is proportional to the square of its thickness, so the PC layer would be the dominant barrier to hydrogen diffusion. This dominance is reflected in the estimated times for the appearance and the saturation of hydrogen at the surfaces of the PC and Pd layers when considered separately (Figure 5.2b). Therefore, for this estimate the sample was treated as a homogeneous PC layer with a thickness of 2.54×10^{-2} cm. According to this model, the time at which hydrogen would appear at the Pd-water interface after 61 ± 38 s. Thus, the phase angle should begin increasing about 61 after hydrogen was supplied to the sample. The same model also predicts hydrogen saturation of at the Pd-water interface after$1.5 \pm 0.9\times10^{3}$ s (25 ± 15 min). Therefore, the phase angle should achieve an apparent equilibrium about 25 min after hydrogen was first supplied to the sample.

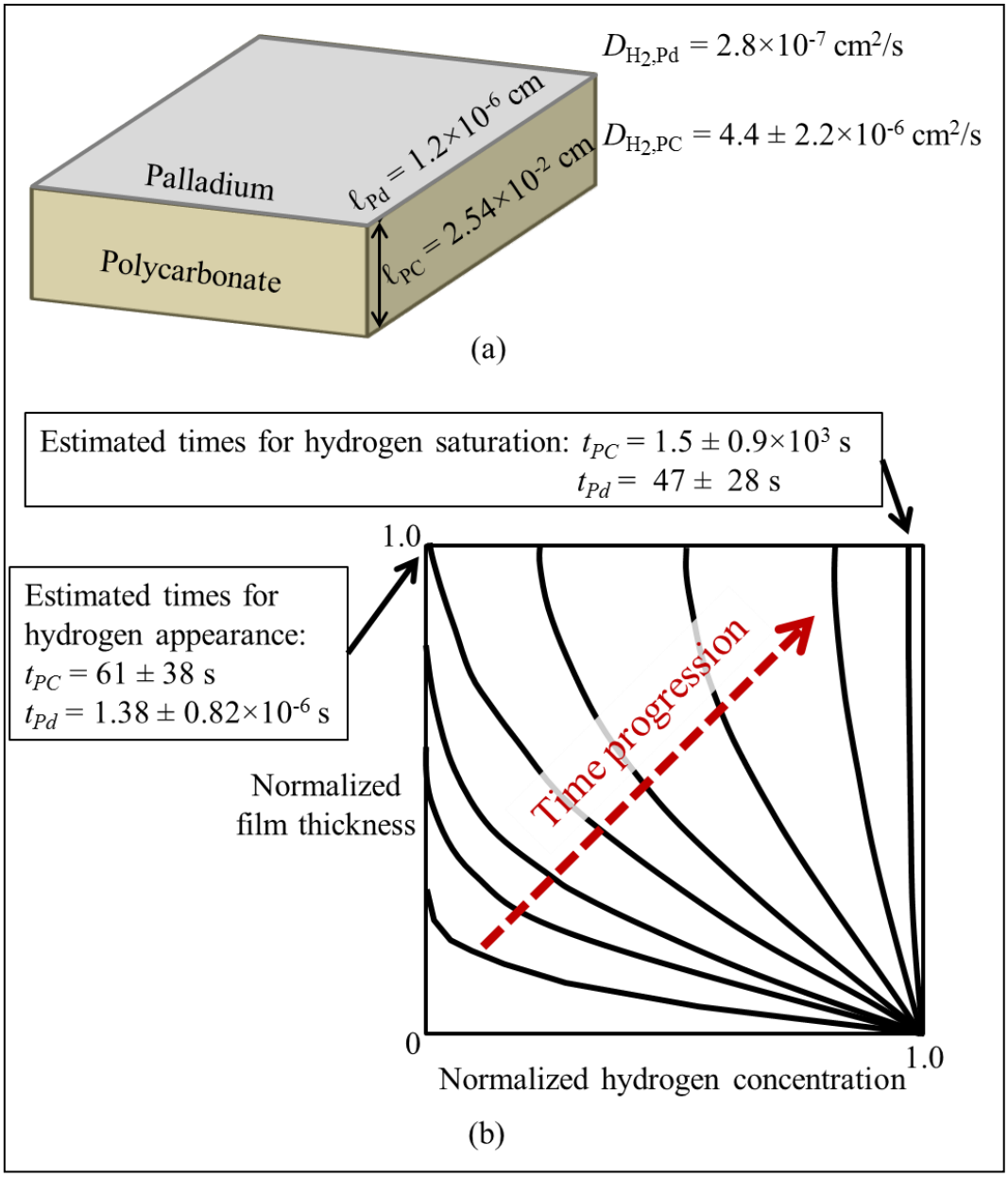

Figure 5.2 - (a) The dimensions and diffusion coefficients for the PC and Pd layers of the Pd-sputtered PC samples that were used for diffusion estimates. The diffusion coefficients differ by one order of magnitude, but the thicknesses differ by four orders of magnitude. (b) This significant difference in thicknesses is reflected in the estimated times for the appearance and saturation of hydrogen at the interface opposite from the hydrogen supply (schematic after Crank[11]). The PC layer is a much more significant barrier to hydrogen diffusion. Thus, the sample can be reasonably considered as only as a homogeneous PC film.

At infinite time, and assuming there is no path for hydrogen to escape, the PC, Pd, and water layers will be saturated with hydrogen according to the temperature and hydrostatic hydrogen pressure throughout the PC-Pd-water composite. However, due to the relatively thick water layer, this would be estimated to take about 17 hours assuming the water is not mixed (diffusion only). This far exceeds the experimental times reported below. However, a near-steady state situation near the Pd surface will prevail since the water near the surface would quickly saturated by hydrogen and the hydrogen sorption of water is relatively low (Table 1).

The above considerations suggest that first appearance of hydrogen at the Pd-water interface should occur about 61 s after hydrogen is applied, with perhaps a slow change of the surface hydrogen population as the water continues to absorb hydrogen. This process should end after about 1,500 s when the Pd is saturated with hydrogen, although hydrogen would still diffuse into the water layer in the approach to saturation. When the hydrogen under the film is exchanged for nitrogen, hydrogen would continue diffusing through the water layer and simultaneously diffuse back through the faster bulk Pd and PC layers. This creates a complex non-steady state diffusion problem. Qualitatively, although the solubility of hydrogen in water is low compared to Pd, the thickness of the water layer makes it a significant hydrogen reservoir. The H_2-N_2-H_2-N_2-H_2 experiment shown below may therefore not quickly return to the pre-H_2 situation, especially because the Pd surface's H_2 population may be leaving the system last due to the its strong sorption.[12]

5.4 Experimental

5.4.1 Materials and Instrument Specifications

The AFM was an Asylum Research (Asylum Research, Santa Barbara, CA 93117) MFP-3D instrument operated in AC mode using WaveMetrics Igor Pro 5.0.5.7 software (WaveMetrics, Inc., Portland, OR 97223). Olympus (Olympus Corporation, Center Valley, PA 18034) BL-AC40TS cantilever probes (rectangular geometry with a radius ~9 ± 2 nm) were used throughout. Ethanol (Sigma-Aldrich, ACS reagent, ≥99.5 wt%), toluene and chloroform (both Fisher Scientific, Certified ACS, 99.9 wt% assay) were used for cleaning. HPLC-grade water (Fisher Scientific, Submicron Filtered) was used to cover the sample. Static charge on samples and probes was removed by exposure to a 500 μCi polonium-210 source (NRD LLC, Model

3C500) for about 10 s immediately prior to installation.[13] Samples were attached to the aluminum sample holder using LocTite Quick Set epoxy (Henkel Corp., Rocky Hill, CT 06067). PC samples were cut from sheets of Lexan PC film with a nominal thickness of 254 μm (ePlastics, San Diego, CA). Some of these samples were sputtered using a 99.95 wt% Pd sputter target (Ted Pella, Redding, CA) using a DESK II magnetron sputter coater (Denton Vacuum, Moorestown, NJ) for three 15 s intervals with a current of 45 mA in 100 mTorr of ambient air. Hydrogen, nitrogen (99.999 vol% purity) were supplied by Matheson Tri-Gas, Manhattan, KS. 316 stainless steel valves and tubing were used (Swagelok, Kansas Valve and Fitting, Kansas City, KS). A custom sample holder allowed for pressurized gas to be supplied beneath the film sample while the AFM scanning took place on the top surface of the film that was immersed in water. A 2-mL reusable glass syringe with metal Luer lock nozzle and attached 10-cm long stainless steel tip was used to transfer degassed HPLC water to the area between the sample and AFM probe holder.

5.4.2 Experimental Procedures

Time and position	Topography	Amplitude	Phase angle	Z-sensor
Time = 0, (x,y) = (1,1)	123	158	845	845
Time = 1, (x,y) = (1,2)	241	534	548	125
Time = 2, (x,y) = (2,2)	235	568	548	456
Time = 3, (x,y) = (2,1)	265	568	165	156

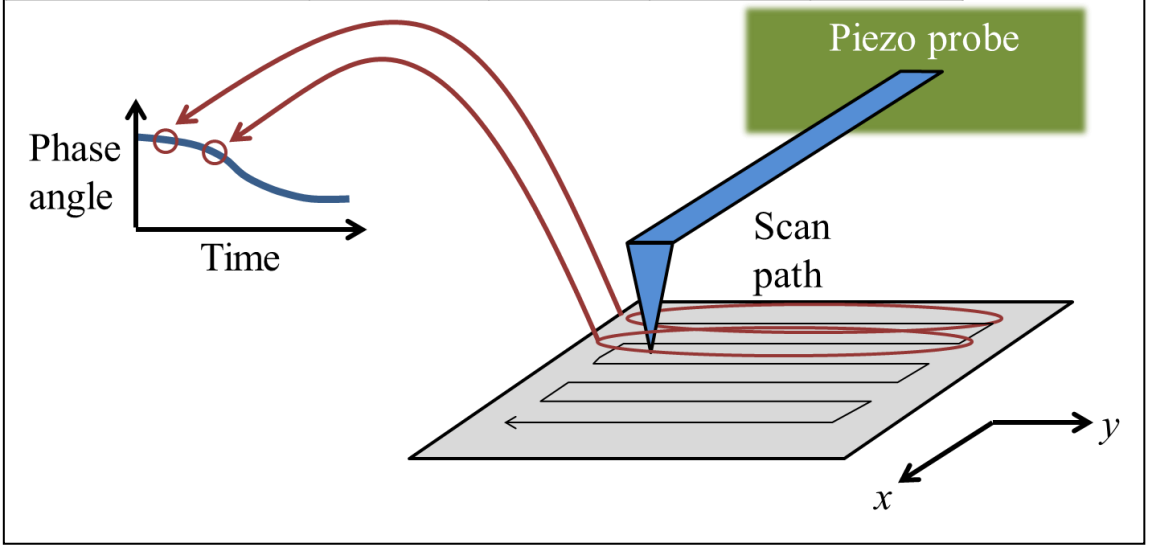

Figure 5.3 - Schematic illustrating the process of data acquisition by AFM and light processing used to produce phase angle vs. time plots of the same data.

5.5 Results and Discussion

Nitrogen adsorption and absorption in or on Pd and PC at room temperature and pressure is negligible.[5] Hydrogen, in contrast, has been shown to interact with bulk Pd to form Pd hydride (PdH) by dissociative chemisorption into the Pd at ambient conditions.[14,15] The hydrogen atoms diffuse into the Pd lattice until reaching equilibrium concentrations of adsorbed and absorbed hydrogen, which is dependent upon the hydrogen partial pressure and temperature.[7,16] Hydrogen adsorption on PC surfaces, in contrast, is limited at ambient conditions to comparatively low equilibrium surface coverage.[17] Equilibrium sorption is three orders of magnitude lower in PC than in Pd (see Table 1). Therefore, phase-angle AFM of bare PC surfaces is expected to show little or no change when hydrogen is present or not, while Pd surfaces are expected to show appreciable differences, both in the gas phase as previously shown[18] and here demonstrated in

the liquid phase. In the work presented here, the water layer contacting the Pd surface is essentially isolated from the PC layer supporting the Pd due to negligible permeation of water through Pd.

A PC sample immersed in water but not sputtered with Pd was studied for reference. Little to no change in phase angle was expected due to the low ab- and adsorption of hydrogen in PC. The phase angle vs. time plot for the unmodified PC sample (Figure 5.4) showed no significant changes in phase angle as scanning progressed and hydrogen was admitted. Because the unmodified PC sample was produced from the same sheet of Lexan as the Pd-sputtered samples, the nominal thickness and the resulting hydrogen diffusion time scale estimate were the same for both sample types. However, at the times when significant changes in phase angle would be expected due to increasing hydrogen concentration, the phase angle remained largely unchanged.

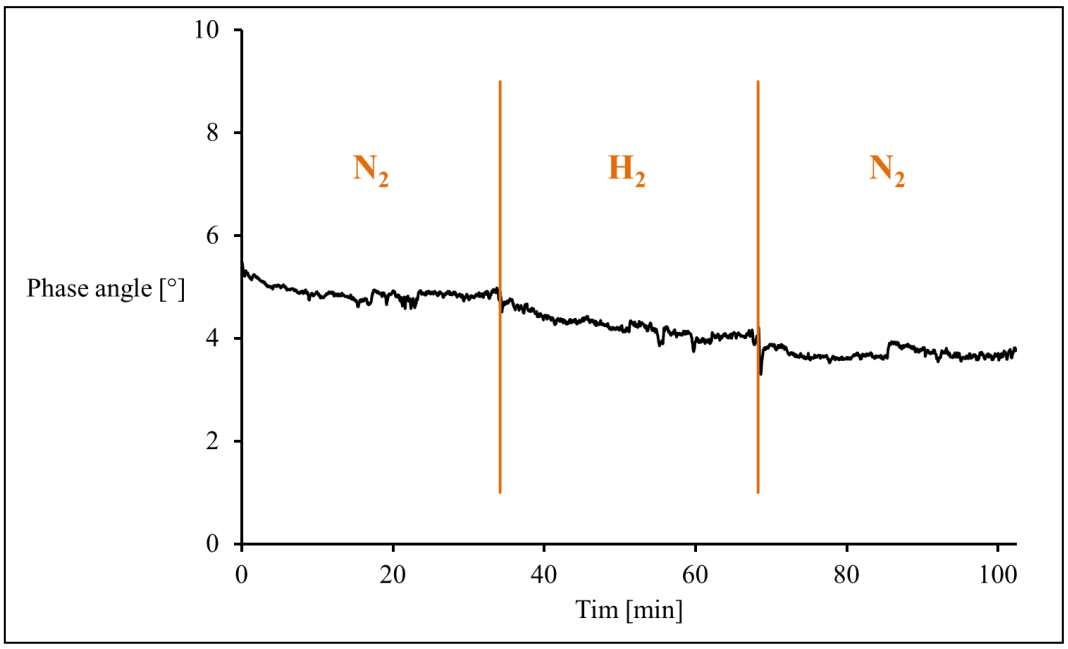

Figure 5.4 - AFM phase-angle results of an unmodified PC film immersed in water. Only a minor change in phase angle occurred due to non-interaction of hydrogen with PC.

Figure 5.5 shows phase angle vs. time plots from five experiments with PC films sputter-coated with Pd. The topography was confirmed to be generally featureless within a 25-nm range with an RMS roughness (R_{RMS}) of 5.335 nm. The phase angle of the Pd surface after switching from nitrogen to hydrogen at the underside of the Pd-sputtered PC film exhibited a gradual increase that correlates with an increasingly repulsive interaction[19,20] attributed to dominant long-

range (non-contact) forces between the probe and a stiff material. The phase angle stabilized about 14 min after the switch from nitrogen to hydrogen (indicated in Figure 5.5 by the dashed red line) which correlates well with the diffusion-based estimate for non-steady state hydrogen transport through the PC/Pd/water composite (subchapter 5.3). 61 ± 38 s was predicted for the first appearance of hydrogen on the Pd, with steady state expected after 25 ± 15 min (see above). This agreement between the diffusion-based calculation and the observed change from higher to lower phase angle provides validation of the phase-angle AFM approach to observe the dynamics of hydrogen appearing on a Pd surface under water.

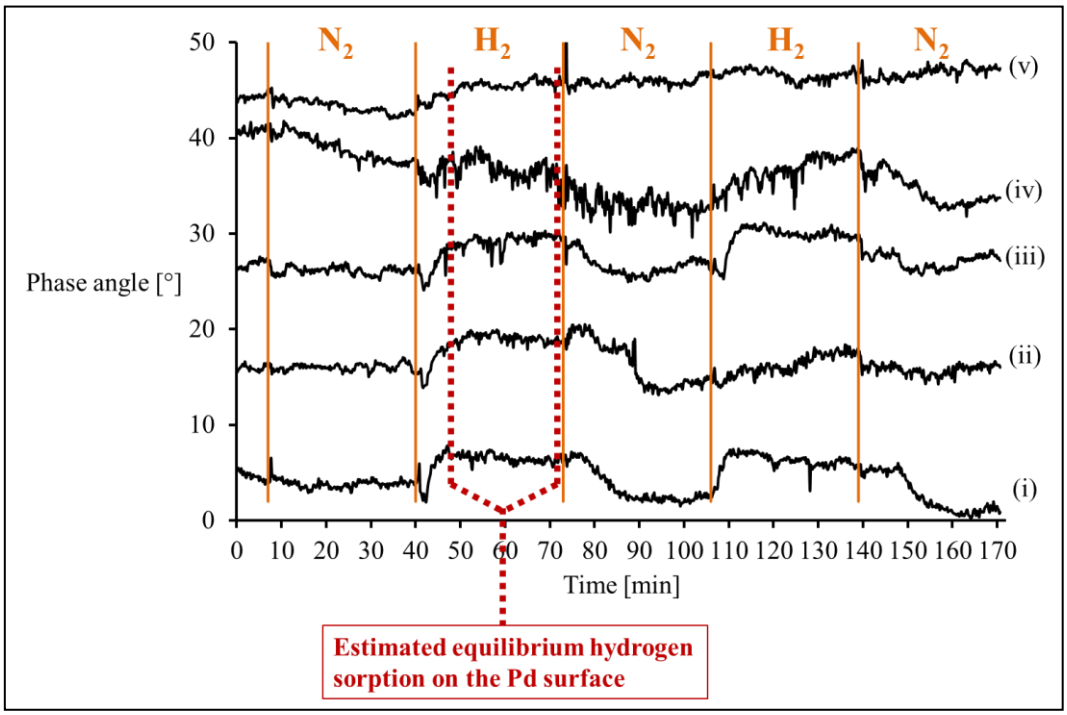

Figure 5.5 - AFM phase-angle results of Pd-sputtered PC films immersed in H_2O. The dashed red lines indicate the estimated range of time for the saturation of the PC-Pd composite film with hydrogen based on diffusion modeling (subchapter 2.4.3). Additional under-liquid scans are shown in Appendix 8.2, but are not shown here due to criteria 2b (subchapter 4.2).

In the first hydrogen segment of experiments (i), (ii), and (iii) shown in Figure 5.5, a decrease in phase angle was observed after about 30 s, which was the time when the first hydrogen was expected to appear on the surface (based on diffusion estimates). During the second hydrogen segment of experiment (iii), this decrease in phase angle was smaller in magnitude while for experiments (i) and (ii) it did not occur at all. This combined with the time

delay indicate that the temporary decreases in phase angle were not due to mechanical disturbances caused by switching the gases. It is possible that the decreases were caused by the hydrogen appearing on the surface reacting with the chemisorbed monolayer of oxygen to form water.[21]

Figure 5.6 summarizes the change in phase angle schematically as a response to increasing presence of adsorbed hydrogen on the Pd surface. The increase in phase angle after the first exposure to hydrogen showed a close correlation to the calculated time scale for hydrogen diffusion to the surface.

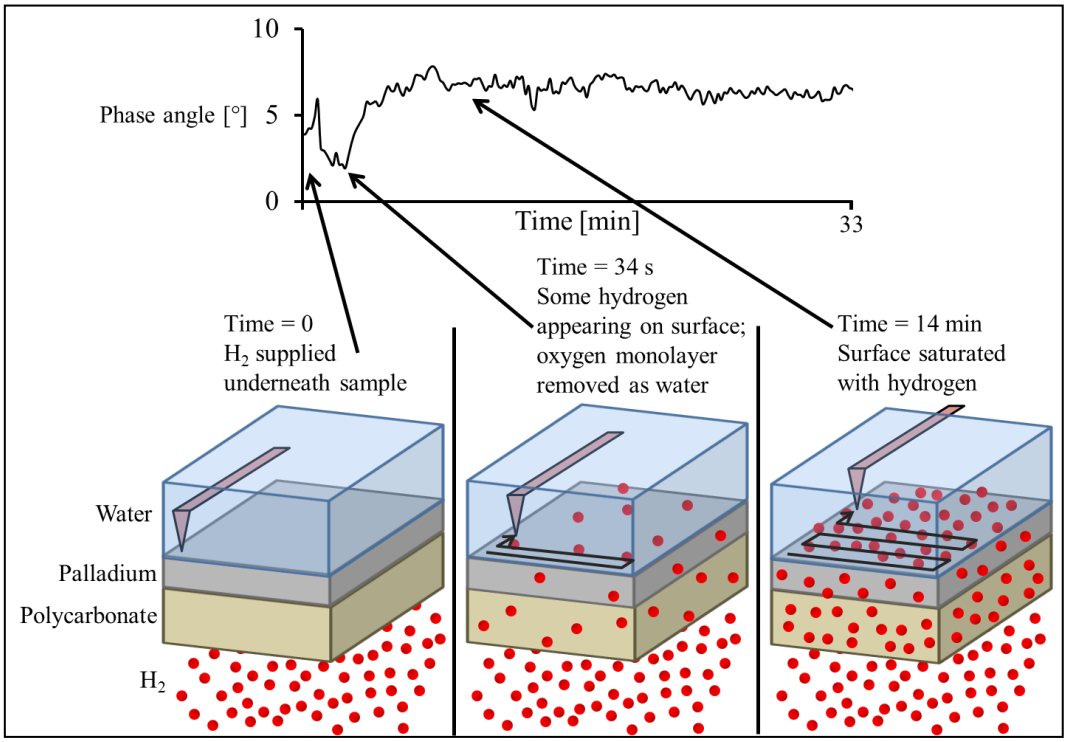

Figure 5.6 - Diffusion of hydrogen through the three-layer system compared to the first hydrogen segment of experiment (i) from Figure 5.5.

Once the gas supplied to the underside of the sample has been switched to nitrogen, the hydrogen sorbed by the PC, Pd, and water layers will begin diffusing back out of the sample. However, some hydrogen will initially continue diffusing further into the unsaturated water layer. This combined with the strong sorption of the surface hydrogen to Pd[12] would alter the dynamics of the hydrogen diffusion in experimental segments subsequent to the initial introduction of hydrogen. Specifically, more time would be required to evacuate hydrogen from

the Pd surface due to the residual availability of hydrogen in the water layer above and the bulk Pd and PC layers below. Furthermore, the nitrogen supply under the sample was the only completely hydrogen-free part of the system. As hydrogen diffused towards the nitrogen gas phase through the Pd and PC layers, hydrogen from the water layer near the Pd surface could re-adsorb at the Pd-water interface. In Figure 5.7, this delay is reflected in the phase-angle results for the second nitrogen segment of experiment (i) from Figure 5.5.

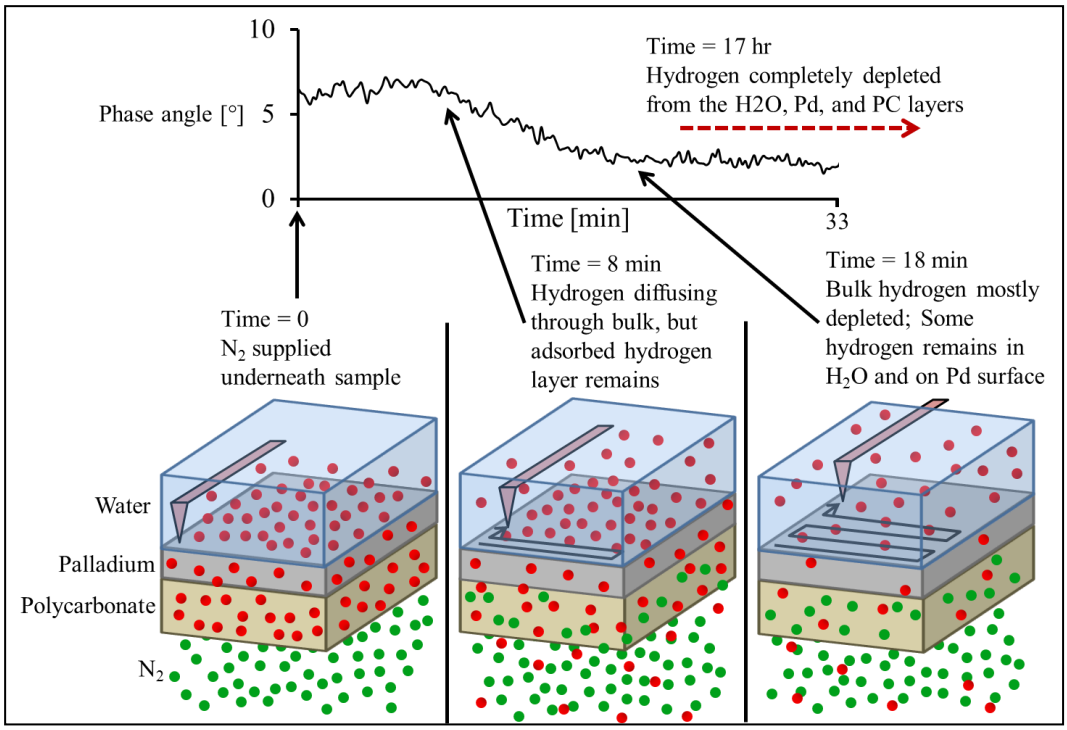

Figure 5.7 - Diffusion of hydrogen through the three-layer system compared to the second nitrogen segment of experiment (i) from Figure 5.5.

The phase angle remained nearly constant for the first 8 min of the scan during the second nitrogen segment. During this time, hydrogen would have been diffusing downward toward the nitrogen supply and upward through the water, but the hydrogen concentration at the surface remained unchanged. This is significantly longer than the 61 ± 38 s estimated for the appearance of hydrogen at the Pd surface indicating that the process of hydrogen removal is not simply the reversal of hydrogen appearing. After the first 8 min, the phase angle began to decrease until reaching an apparent equilibrium 10 min later (i.e., 18 min after the switch from hydrogen to nitrogen). This is not the time for which hydrogen could be expected to be completely removed from the PC, Pd, and water layers, but rather when the diffusion of hydrogen becomes negligible.

One might expect a similar step change on desorption of hydrogen as was observed in the gas phase experiments (Chapter 4). However, a small amount of hydrogen dissolved in the water layer may re-supply the adsorbed hydrogen near the palladium surface for some time perhaps on the order of hours (17 hours estimated for complete hydrogen removal).

The spatial resolution, the real-time nature of the observation, and the simultaneous topographic information, along with the conditions of room temperature and atmospheric pressure make this technique ideally suited to observe, for example, liquid-phase hydrogenation catalyst surfaces. Mass transfer issues (surface diffusion, bulk diffusion) coupled with geometry (islands of catalyst, catalyst layer thickness) and topography (flat vs. sculpted, or deliberately designed) are interesting targets for the technique demonstrated here since the presence and abundance of hydrogen over time impacts selectivity and catalyst lifetime. Other mass transport-dependent phenomena such as embrittlement of metals in the presence of hydrogen may also be successfully studied with phase-angle AFM.

5.6 Conclusions and Outlook

Phase-angle data from AFM imaging of water-immersed Pd surfaces dynamically detects the appearance of hydrogen on the Pd surface in real time and at room temperature as hydrogen gas diffuses through the substrate and appears at the immersed Pd surface. The experimental results correlate well with calculations based on one-sided diffusion of hydrogen through a PC-Pd-water composite. Comparison between the Pd-sputtered PC sample and the unmodified PC sample further confirm that hydrogen was detected. These results demonstrate the potential of phase-angle AFM to dynamically and spatially study hydrogen on catalytic materials in the liquid phase at ambient conditions in real time with nanometer-level resolution.

Techniques that can observe heterogeneous hydrogenation catalyst surfaces in the liquid phase at nanometer-level spatial resolution achieved here in real time are essentially not available. The technique shown here will be tested to observe reactions when the liquid phase contains molecules that can react with hydrogen. AFM hardware for high temperature and pressure conditions is under development by others. This hardware development together with the technique shown here would allow for the observation of heterogeneous catalyst surfaces in real time operating under truly realistic reaction conditions.

5.7 References

[1] Roobol, S. B.; Cañas-Ventura, M. E.; Bergman, M.; van Spronsen, M. A.; Onderwaater, W. G.; van der Tuijn, P. C.; Koehler, R.; Ofitserov, A.; van Baarle, G. J. C.; Frenken, J. W. M. The ReactorAFM: Non-contact atomic force microscope operating under high-pressure and high-temperature catalytic conditions. *Rev. Sci. Instrum.* **2015**, *86*, 033706.

[2] NSF Award Search: Award #1429545. http://www.nsf.gov/awardsearch/showAward?AWD_ID=1429545&HistoricalAwards=false (Accessed 18 August 2015).

[3] Barrer, R. M. *Diffusion In and Through Solids*, Cambrigde Press, London, 1951.

[4] Hacarlioglu, P.; Toppare, L.; Yilmaz, L. Polycarbonate-polypyrrole mixed matrix gas separation membranes. *J. Membr. Sci.* **2003**, 225 (1-2), 51-62.

[5] Koros, W. J.; Chan, A. H.; Paul, D. R. Sorption and transport of various gases in polycarbonate. *J. Membr. Sci.* **1997**, 2 (2), 165-190.

[6] Costello, L. M.; Koros, W. J. Effect of Structure on the Temperature Dependence of Gas Transport and Sorption in a Series of Polycarbonates. *J. Polym. Sci.* **1994**, *32* (4), 701-713.

[7] Ackerman, F. J.; Koskinas. G. J. Permeation of Hydrogen and Deuterium Through Palladium-Silver Alloys. *J. Chem. Eng. Data* **1972**, *17* (1), 51-55.

[8] Hironori U.; Tatsuo N.; Isamu U. Electrochemical Measurements of Single Particles of Pd and LaNi5 with a Microelectrode Technique. *J. Electroanal. Chem.* **1995**, 396, 169-173.

[9] Brass, A. M.; Collet-Lacoste, J. The Influence of Surface on the Permeation of Hydrogen in Iron and Palladium. In *Proceedings of the Symposium on Electrochemical Surface Science of Hydrogen Adsorption and Absorption*; Jerkiewicz, G., Marcus, P., Eds.; The Electrochemical Society, Inc.: Pennington, NJ, 1997; pp 200-210.

[10] Mazarei, A. F.; Sandall, O. C. Diffusion Coefficients for Helium, Hydrogen, and Carbon Dioxide in Water at 25°C. *AIChE J.* **1980**, *26* (1), 154-157.

[11] Crank, J. The Mathematics of Diffusion; Oxford University Press: Oxford, 1975; pp 45-68.

[12] Ohno, S.; Wilde, M.; Fukutani, K. Novel insight into the hydrogen absorption mechanism at the Pd(110) surface. *J. Chem. Phys.* **2014**, *140*, 134705.

[13] McBride. S. P. Surface Science Experiments Involving the Atomic Force Microscope. Ph.D. Thesis, Kansas State University, Manhattan, KS, 2012.

[14] Nowakowski, R.; Dus, R. Atomic Force Microscopy Studies of Thin Pd Film Response to Palladium Hydride Formation and Its Reaction with Oxygen. *Langmuir* **2003**, *19*, 6750-6758.

[15] Johansson, M.; Skúlason, E.; Nielsen, G.; Murphy, S.; Nielsen, R. M.; Chorkendorff, I. Hydrogen Adsorption on Palladium and Palladium Hydride at 1 bar. *Surf. Sci.* **2010**, *604*, 718-729.

[16] Wicke, E.; Brodowsky, H. Hydrogen in Palladium and Palladium Alloys. In *Hydrogen in Metals II*; Alefeld, G., Völkl, J., Eds.; Topics in Applied Physics; Springer-Verlag: Berlin, 1978; Vol. 29, pp 73-155.

[17] Battino, R.; Clever, H. L.; Wiesenburg. D. A. *Solubility Data Series*; Young, C. L., Ed.; Pergamon Press Ltd.: Oxford, UK, 1981; p. 2.

[18] Young, M. J., Pfromm, P. H., Rezac, M. E., Law, B. M., "Analysis of Atomic Force Microscopy Phase Data To Dynamically Detect Adsorbed Hydrogen under Ambient Conditions", *Langmuir*, **2014** ,*30* (40), 11906-11912.

[19] Tamayo, J.; García, R. Relationship between Phase Shift and Energy Dissipation in Tapping-mode Scanning Force Microscopy. *Appl. Phys. Lett.* **1998**, *73*, 2926-2928.

[20] Martínez, N. F.; García, R. Measuring Phase Shifts and Energy Dissipation with Amplitude Modulation Atomic Force Microscopy. *Nanotechnology* **2006**, *17*, S167-S172.

[21] Petersson, L.-G.; Dannetun, H. M.; Lundström, I.; The Water-forming Reaction on Palladium. *Surf. Sci.* **1985**, *161*, 77-100.

6 Recommendations and Outlook

6.1 Addressing Issues with Current Liquid/Solid Interface Experiments

Improving the setup used for phase-angle AFM experiments is a non-trivial part of future work. As detailed in Chapter 4, the setup that proved most reliable of those attempted was the small-aperture sample holder with the slower scan rate. The method used to install samples in the sample holder also needs to be addressed. A new method is needed which allows for the sample to be easily, reproducibly, and non-destructively secured in the sample holder while minimizing the impact of gas delivery on the sample's positioning.

6.2 Expanding to In-situ Studies of Chemical Reactions

6.2.1 Gas-phase Hydrogenation

For studying gas-phase heterogeneous catalytic hydrogenation reactions, it would be best to use a setup similar to that used for liquid-phase experiments detailed in Chapters 4 and 5. Specifically, hydrogen would be supplied by diffusion through the substrate to a catalytic surface with a gas reagent above it. A flow-through cell would be needed to contain the gas reagent while allowing the AFM probe to scan the surface. As in experiments described in this dissertation, the AFM phase-angle data would be examined to understand the dynamic interactions of hydrogen with the surface. Of particular interest would be phenomena related to live catalytic reactions such as catalyst coking.

6.2.2 Phenylacetylene Hydrogenation and Catalyst Coking at Room Temperature

Although a wide range of liquid-phase heterogeneous catalytic hydrogenation experiments could be studied using phase-angle AFM, many would require elevated temperatures for the reaction to proceed. However, phenylacetylene hydrogenation over a Pd catalyst can be performed at room temperature. Phenylacetylene has been used as a model reagent for alkyne hydrogenation and catalyst coking experiments.[1] Catalyst coking occurs when unsaturated hydrocarbons polymerize on the surface of a hydrogen-deficient catalytic surface.[2] Similar to other under-liquid experiments presented in this dissertation, the hydrogen gas would be supplied by diffusion through the substrate to the catalytic surface immersed in the liquid reagent.

However, because phenylacetylene readily dissolves polycarbonate, it is recommended that a polytetrafluoroethylene film be used instead.

During the hydrogenation experiments, the phase angle would be used to identify coking nucleation and topography would be used to monitor its buildup over the surface. Coking and phenylacetylene hydrogenation rates would be determined for different hydrogen fluxes through the substrate and Pd layers. Different hydrogen fluxes would be achieved by varying the gas mixture supplied to the substrate and/or using substrates of different thicknesses. Furthermore, the structure and composition of the deposited catalyst could be varied. Clusters of deposited catalyst of different morphologies could be used, as well as other precious or base metals that are not hydrogen permeable. In this case, hydrogen would diffuse through the exposed polymer regions of the imperfect metal layer before adsorbing to the catalyst clusters.

6.3 References

[1] Gamas, E. D.; Schifter, I. Influence of the Support on the Deactivation of Nickel Zeolite Catalysts During the Conversion of Phenylacetylene. In *Catalyst Deactivation*; Bartholomew, C. H., Fuentes, G. A., Eds.; Elsevier Science B.V.: 1997, Vol. 111, p 119.

[2] Trimm, D. L. Catalyst Design for Reduced Coking (Review). *Appl. Catal.* **1983**, *5* (3), 263-290.

7 Conclusions

Atomic force microscopy (AFM) was used to study Pd surfaces sputtered on polycarbonate (PC) substrates to dynamically detect the presence of hydrogen on the Pd surface through changes in phase angle.

1. In the gas phase, on a Pd surface, AFM phase angle was found to *decrease* with the appearance of hydrogen (subchapter 3.3).
2. In the liquid phase, on a Pd surface, AFM phase angle was found to *increase* with the appearance of hydrogen (subchapter 5.5).
3. The decrease or increase matches predicted changes in the properties of Pd in presence of hydrogen (subchapter 2.1.2).
4. Dynamic, real-time changes in phase angle approximately match mass transfer estimates for transport of hydrogen through the samples investigated here based on well-established, simplified second-order diffusion models (subchapters 3.3 and 5.3)
5. The phase-angle data experimentally corroborates gas-phase fundamental studies of Pd-hydrogen interaction where a more strongly retained hydrogen population within a few atomic diameters of the metal surface was found by methods other than AFM (subchapter 3.3)
6. The spatial phase-angle resolution of the work described here was around 20 nm (subchapter 2.1.1).
7. AFM offers a temporal resolution up to 0.5 s for phase angle (subchapter 2.1.1)
8. AFM phase angle successfully overcomes many technical limitations that often hinder in-situ catalyst studies especially in the liquid phase (subchapter 2.1)

8 Appendices

8.1 Appendix A - Additional AFM Results of Pd-gas Interface Experiments

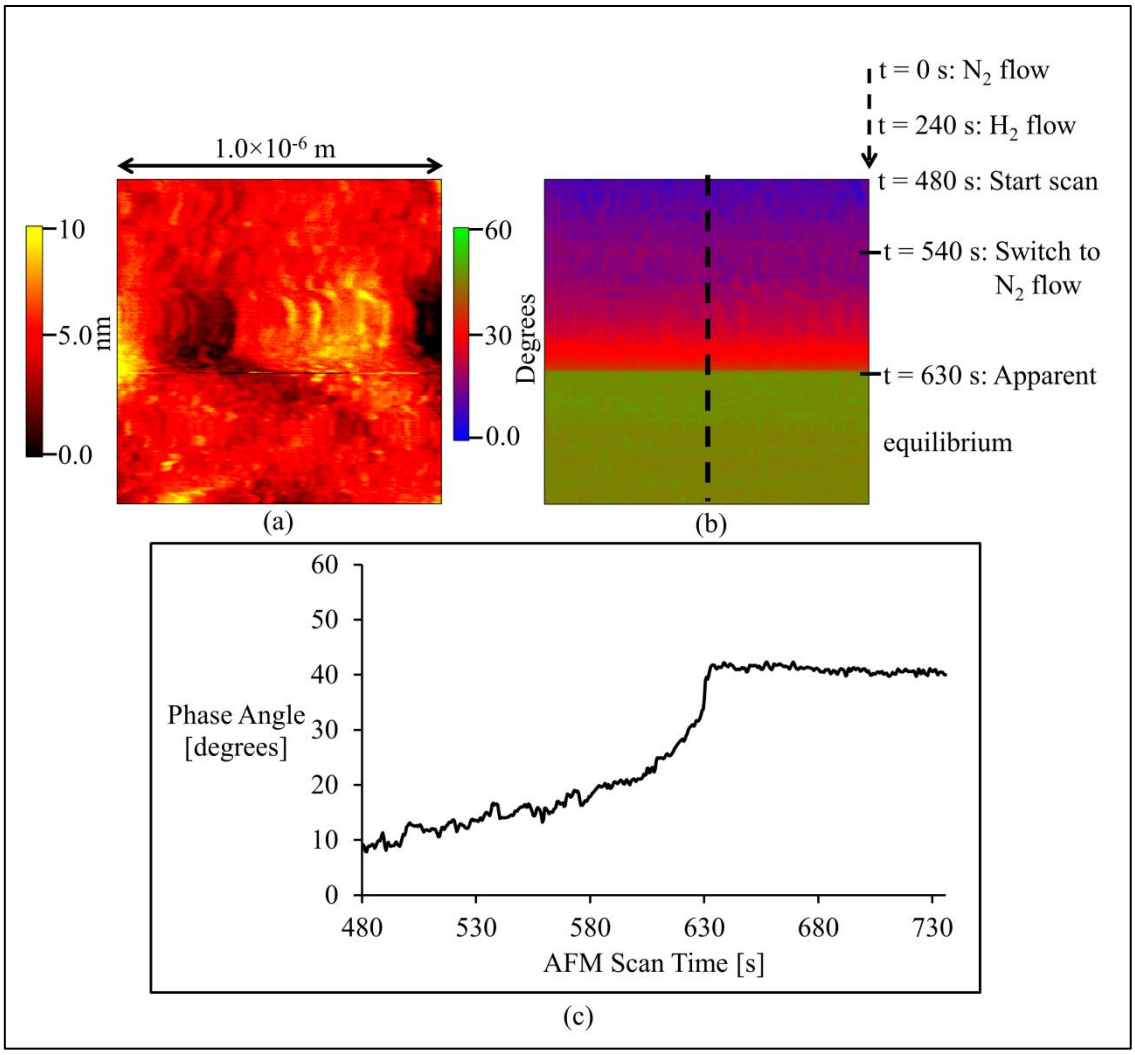

Figure 8.1 - Tapping-mode images of a PC surface sputter-coated with Pd prepared in similar manner as the one used for Figure 4: (a) topography image (RRMS = 1.575 nm); (b) phase-angle image; (c) phase-angle data along the dotted line shown in panel b. The scan was initiated with hydrogen gas flowing over the sample before switching to nitrogen flow at ~540 s. The gradual phase-angle shift from ~540 s to ~630 s indicates a diminishing amount of adsorbed hydrogen coinciding with depleting hydrogen in the bulk culminating in a hydrogen-vacated surface at ~630 s.

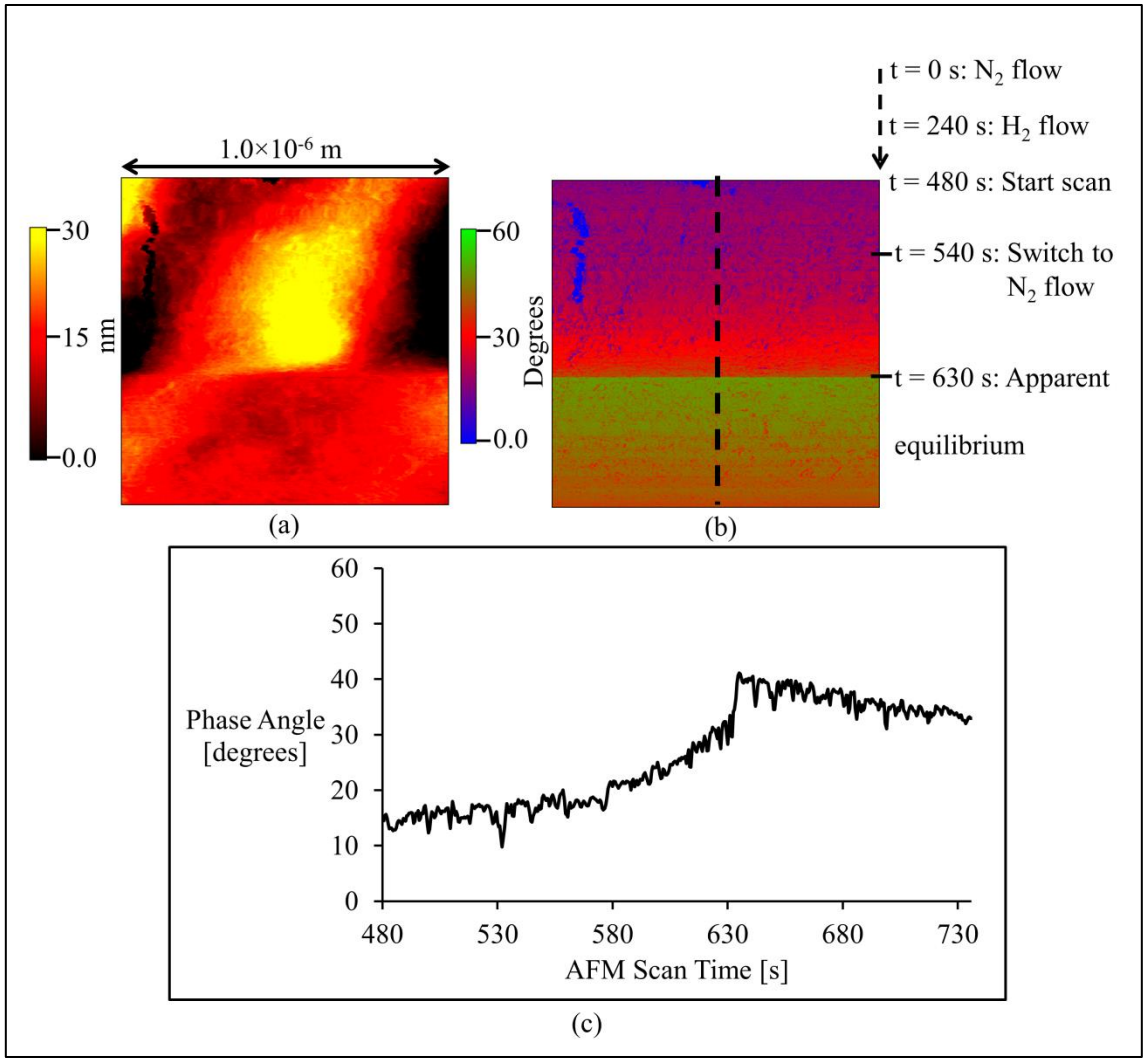

Figure 8.2 - Tapping-mode images of a PC surface sputter-coated with Pd prepared in similar manner as the one used for Figure 4: (a) topography image (RRMS = 7.915 nm); (b) phase-angle image; (c) phase-angle data along the dotted line show in panel b. The scan was initiated with hydrogen gas flowing over the sample before switching to nitrogen flow at ~540 s. The gradual phase-angle shift from ~540 s to ~630 s indicates diminishing adsorbed hydrogen coinciding with depleting hydrogen in the bulk culminating in a hydrogen-vacated surface at ~630 s.

8.2 Appendix B - Compiled Atomic Force Microscopy Phase-angle Data Graphs for Experiments under H_2O

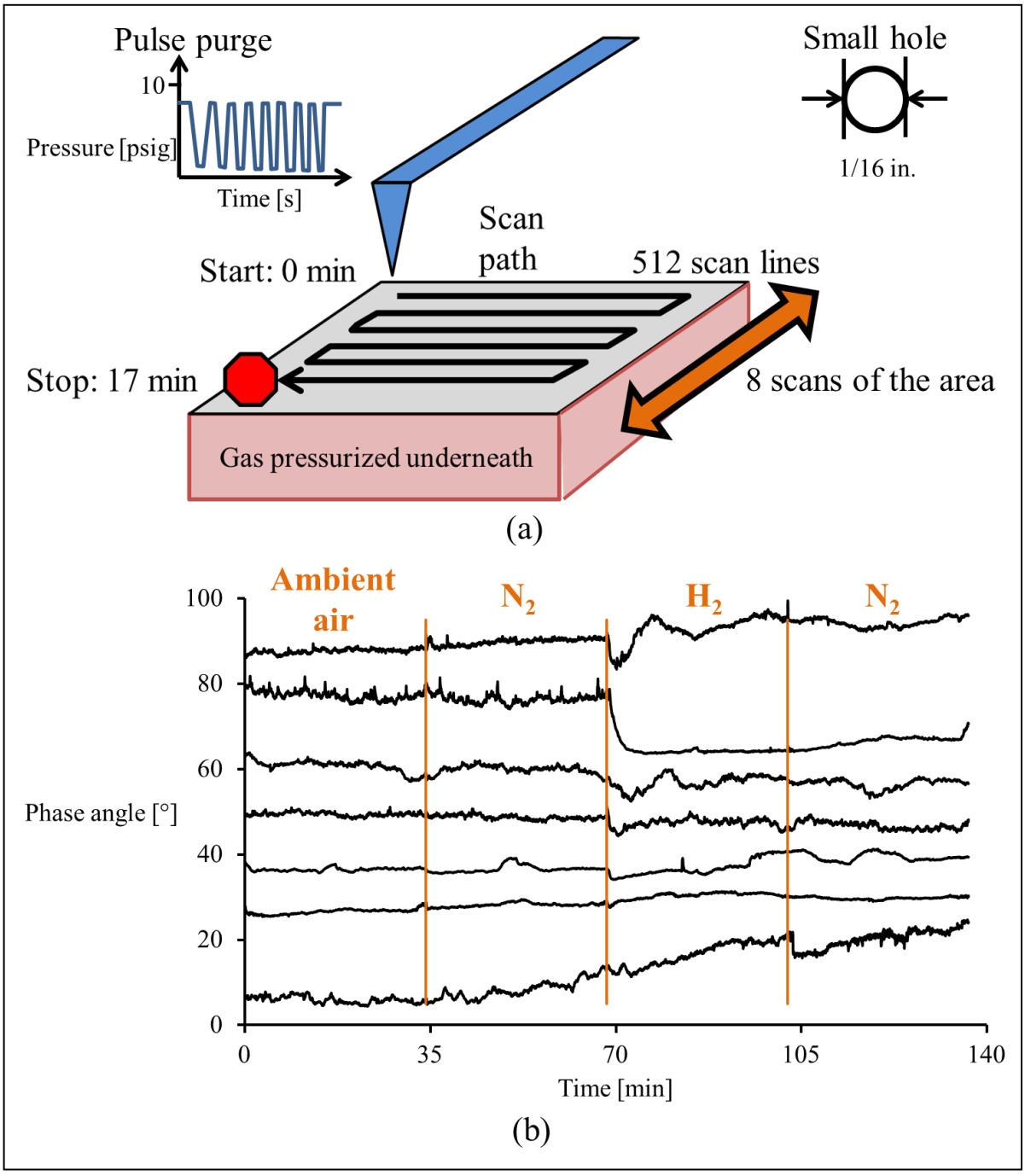

Figure 8.3 - Compiled phase-angle results of hydrogen diffusion experiments conducted with PC films (l = 0.010 in.) sputtered with Pd for 45 s.

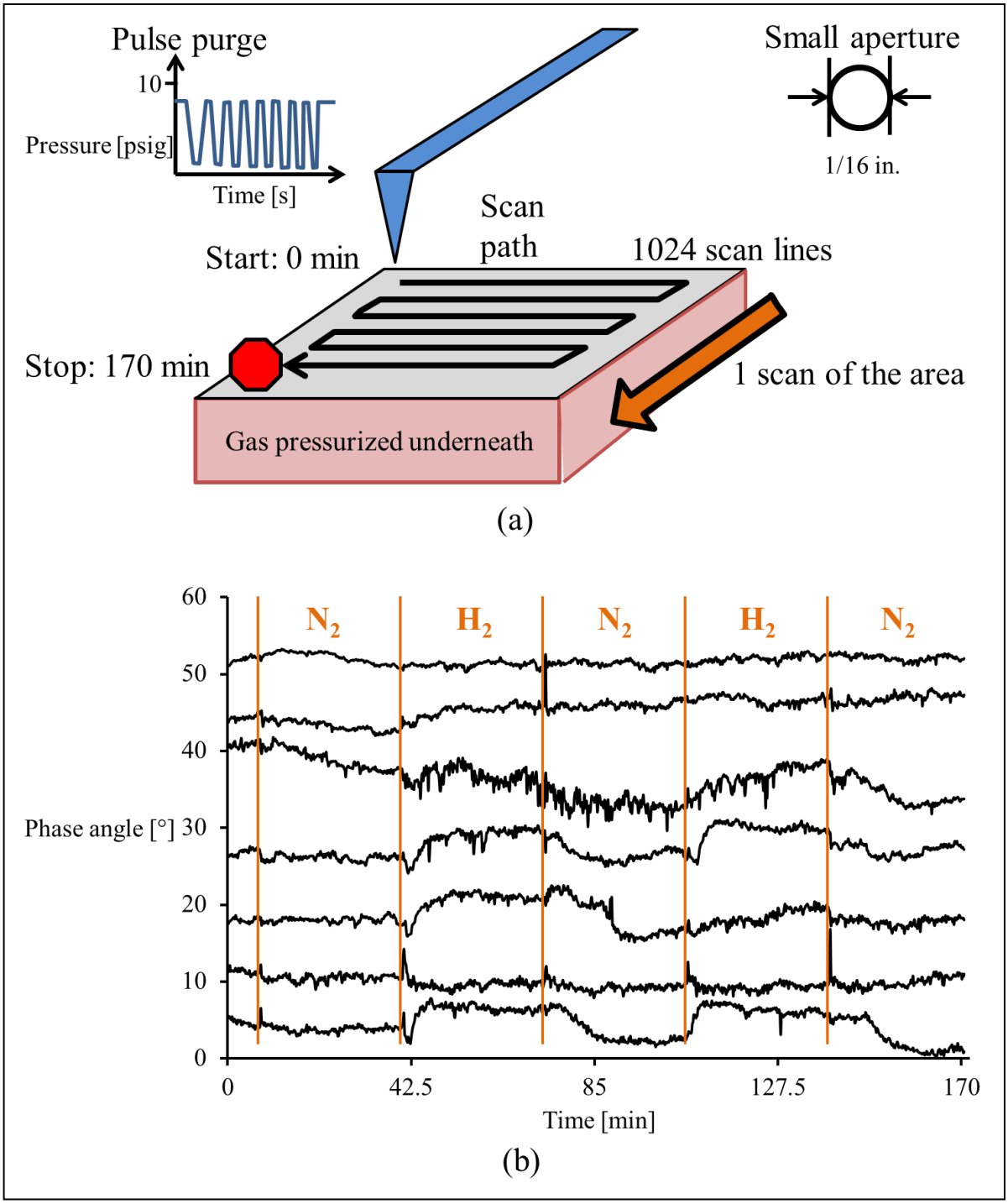

Figure 8.4 - Compiled phase-angle results of hydrogen diffusion experiments conducted with PC films (l = 0.010 in.) sputtered with Pd for 45 s.

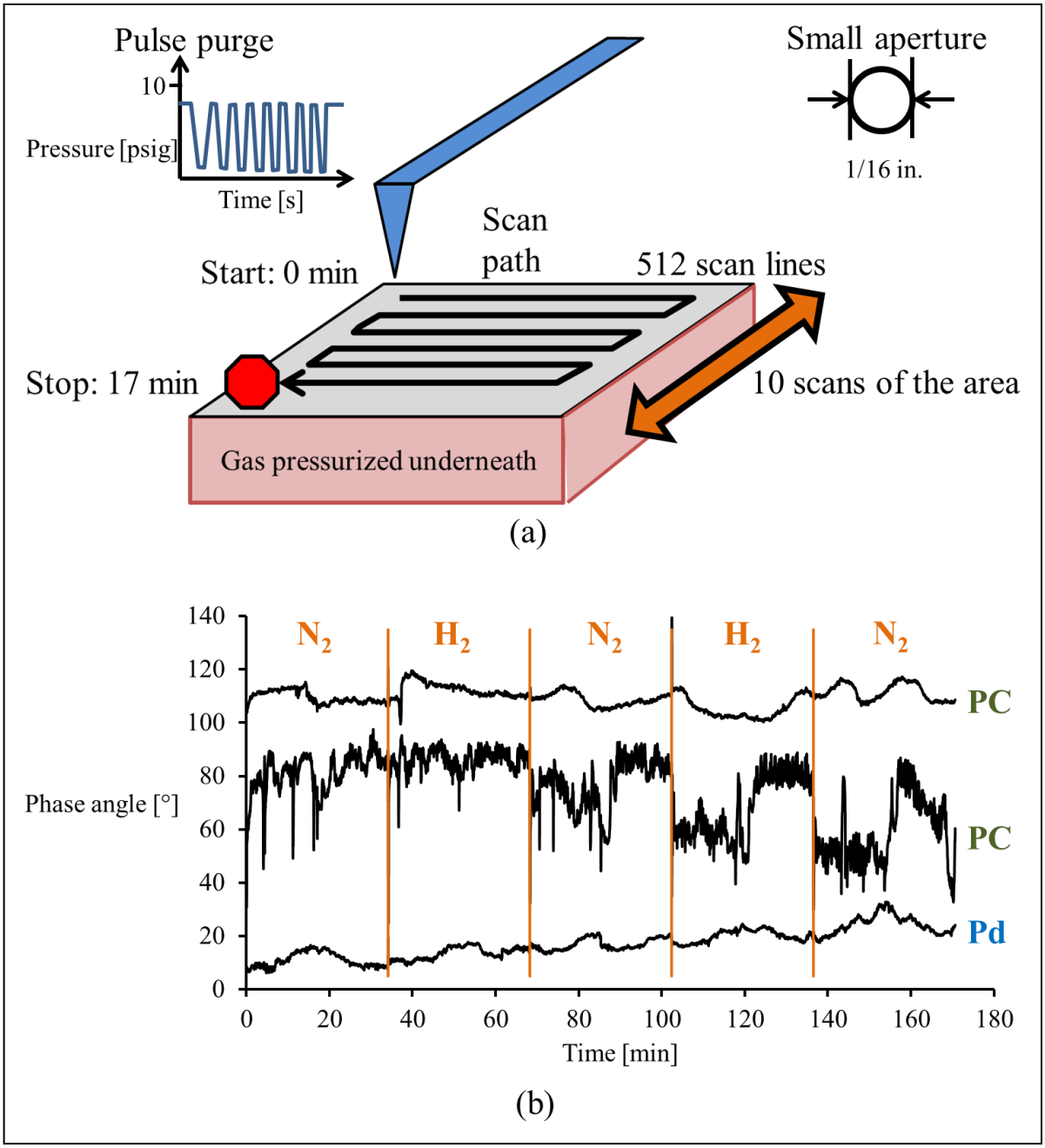

Figure 8.5 - Compiled phase-angle results of hydrogen diffusion experiments conducted with PC films (l = 0.010 in.) sputtered with Pd for 45 s or unmodified PC films (l = 0.010 in.).

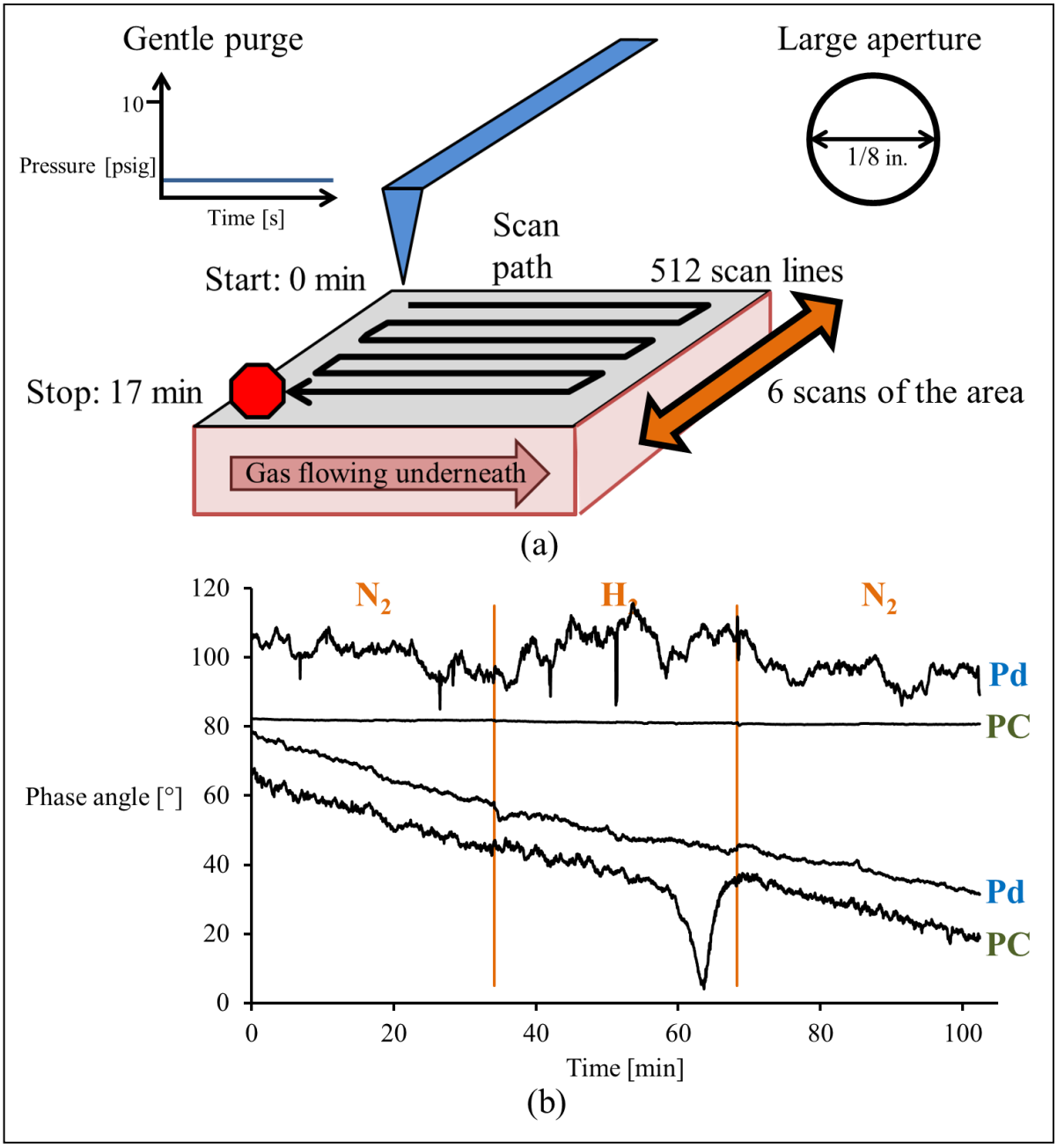

Figure 8.6 - Compiled phase-angle results of hydrogen diffusion experiments conducted with PC films (l = 0.010 in.) sputtered with Pd for 45 s or unmodified PC films (l = 0.010 in.).

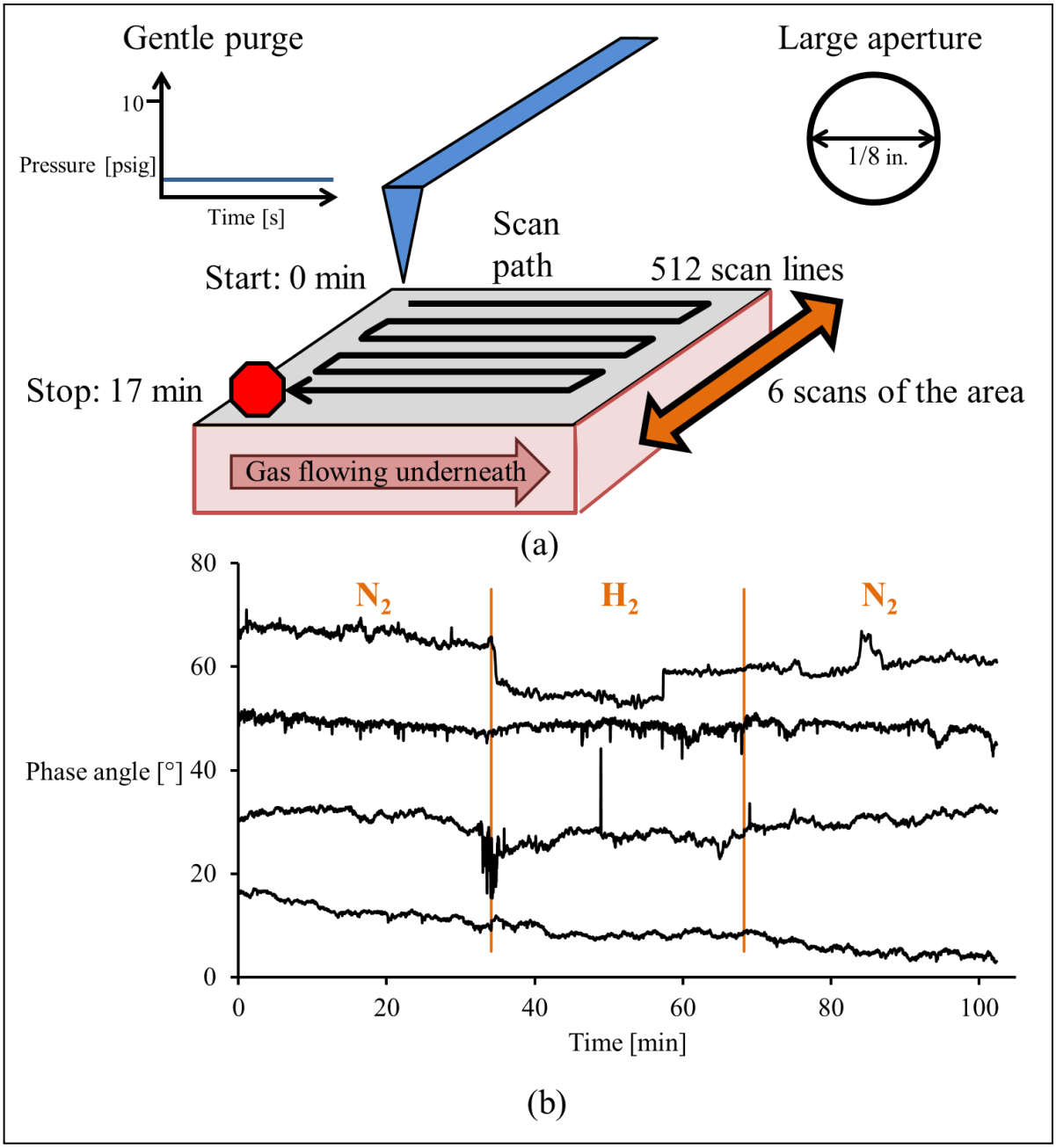

Figure 8.7 - Compiled phase-angle results of hydrogen diffusion experiments conducted with PC films (l = 0.010 in.) sputtered with Pd for 45 s.

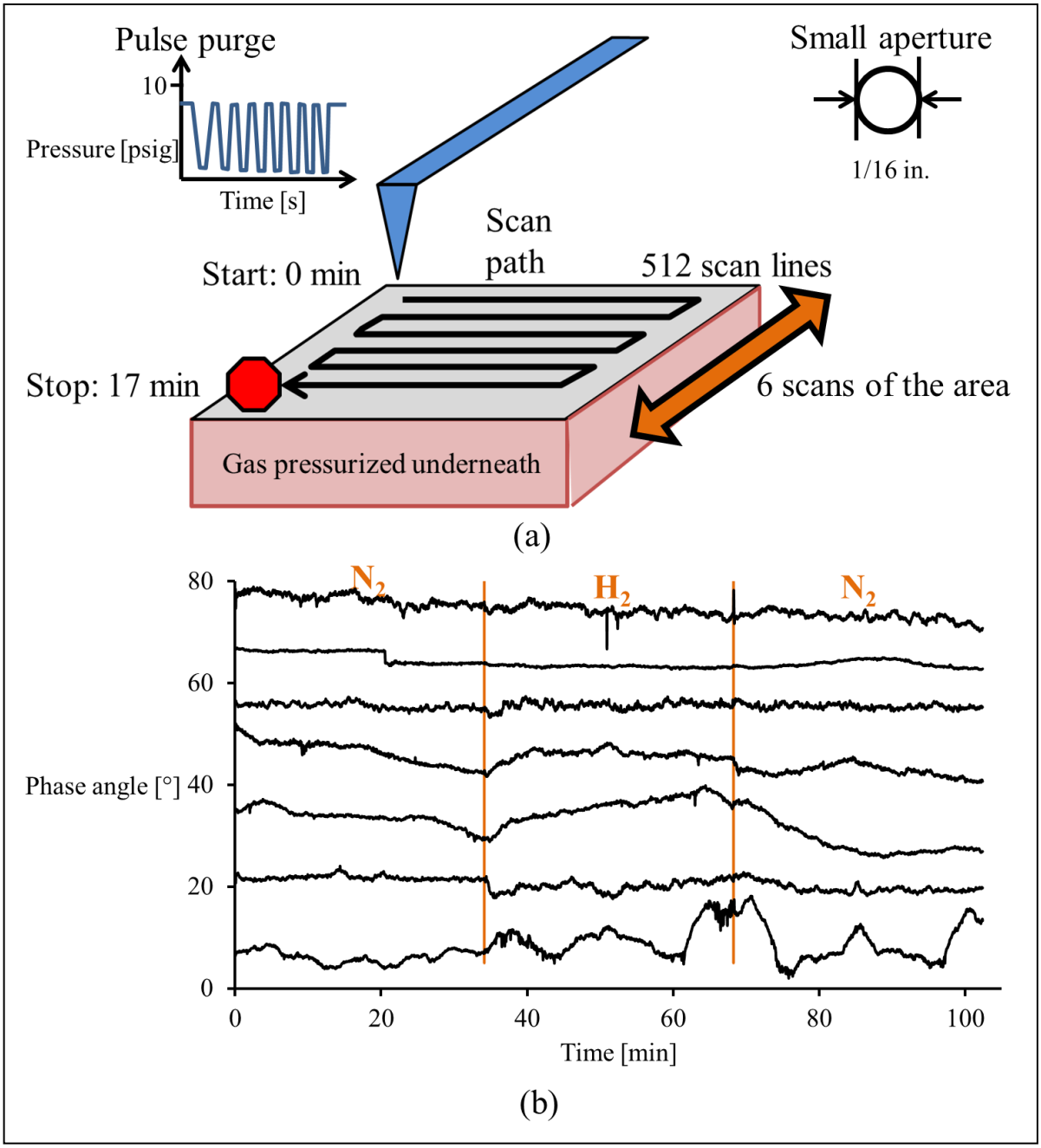

Figure 8.8 - Compiled phase-angle results of hydrogen diffusion experiments conducted with PC films (l = 0.010 in.) sputtered with Pd for 45 s or unmodified PC films (l = 0.010 in.).

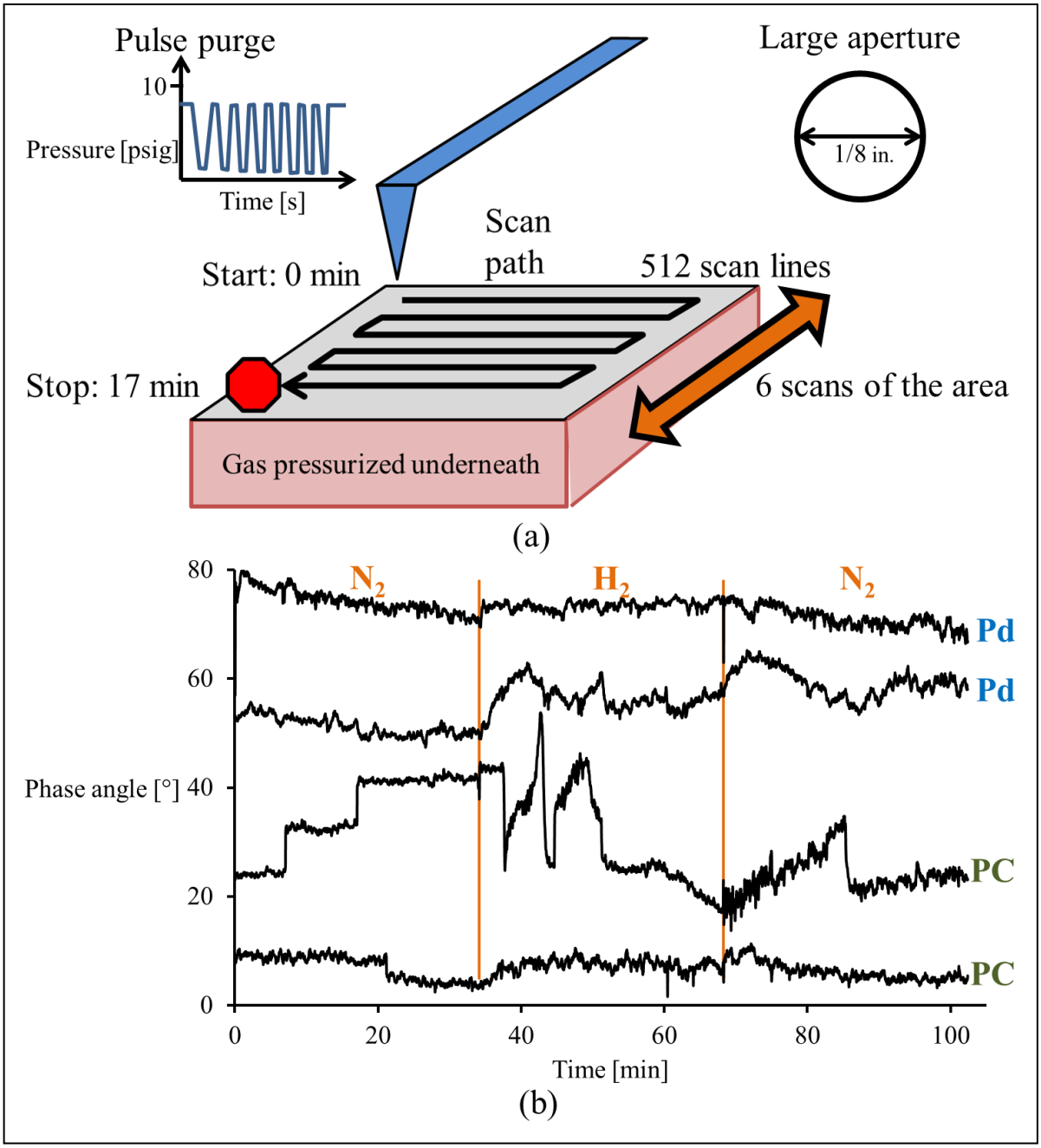

Figure 8.9 - Compiled phase-angle results of hydrogen diffusion experiments conducted with PC films (l = 0.010 in.) sputtered with Pd for 45 s.

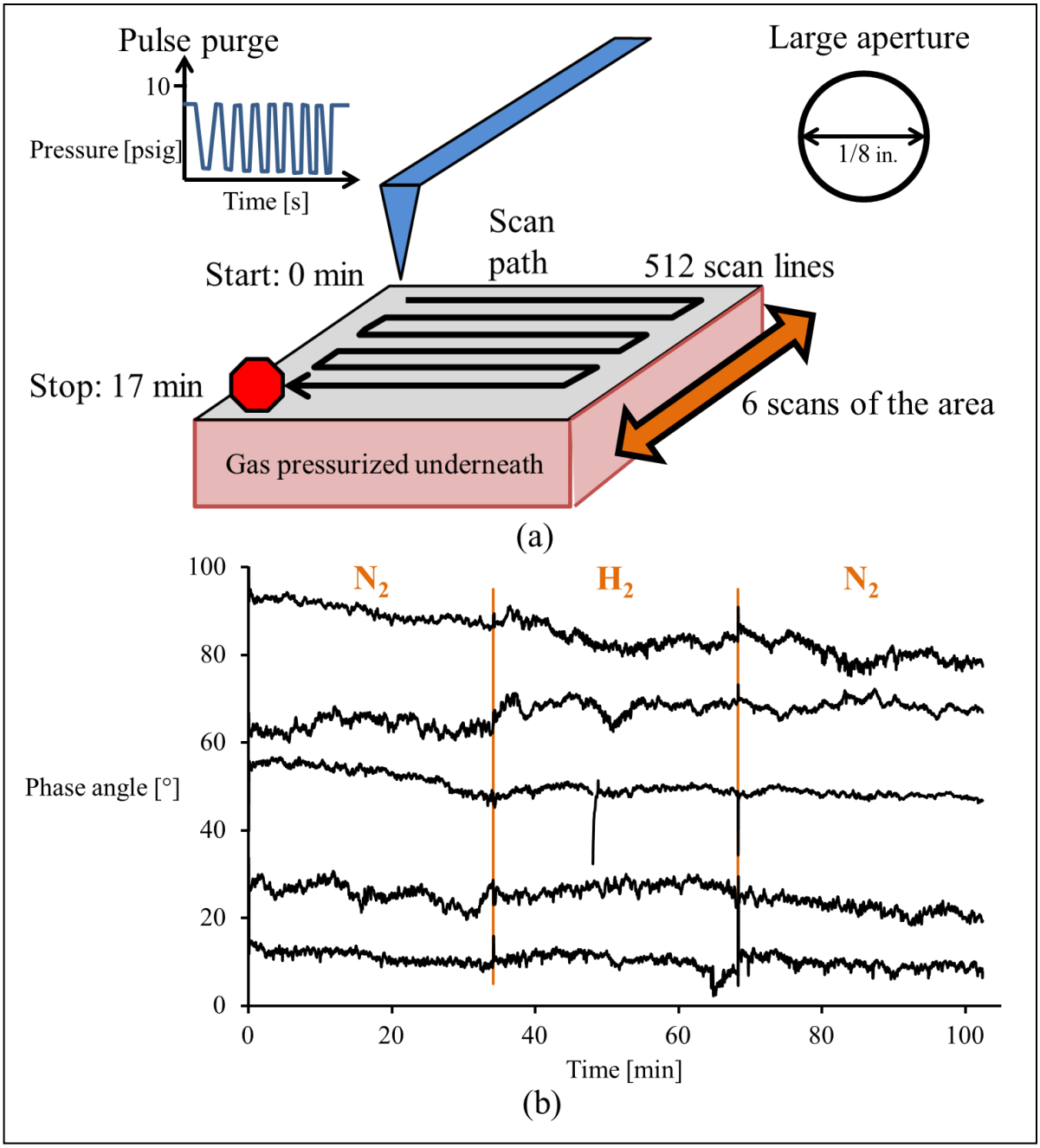

Figure 8.10 - Compiled phase-angle results of hydrogen diffusion experiments conducted with PC films (l = 0.010 in.) sputtered with Pd for 45 s.

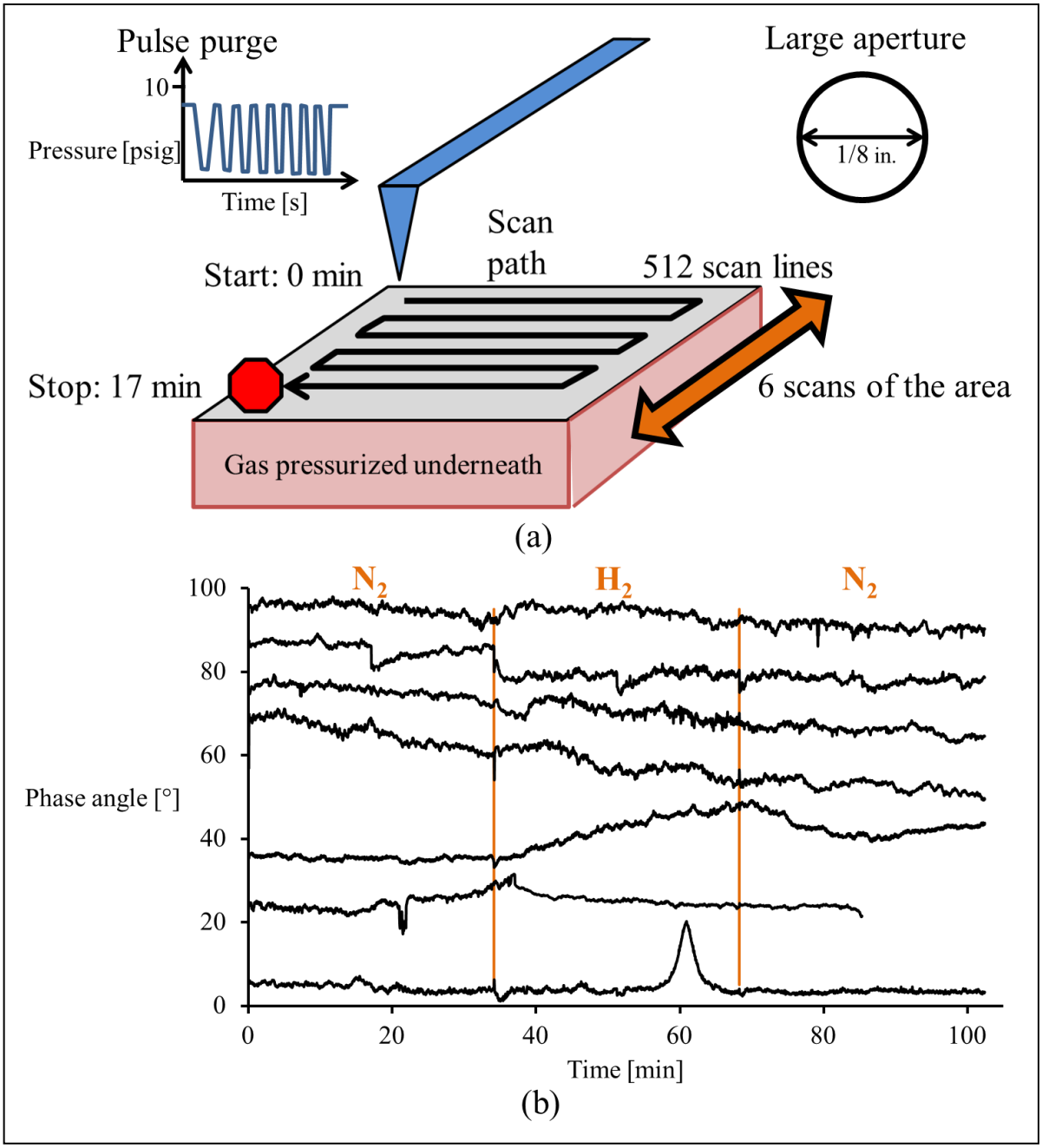

Figure 8.11 - Compiled phase-angle results of hydrogen diffusion experiments conducted with PC films (l = 0.010 in.) sputtered with Pd for 45 s.

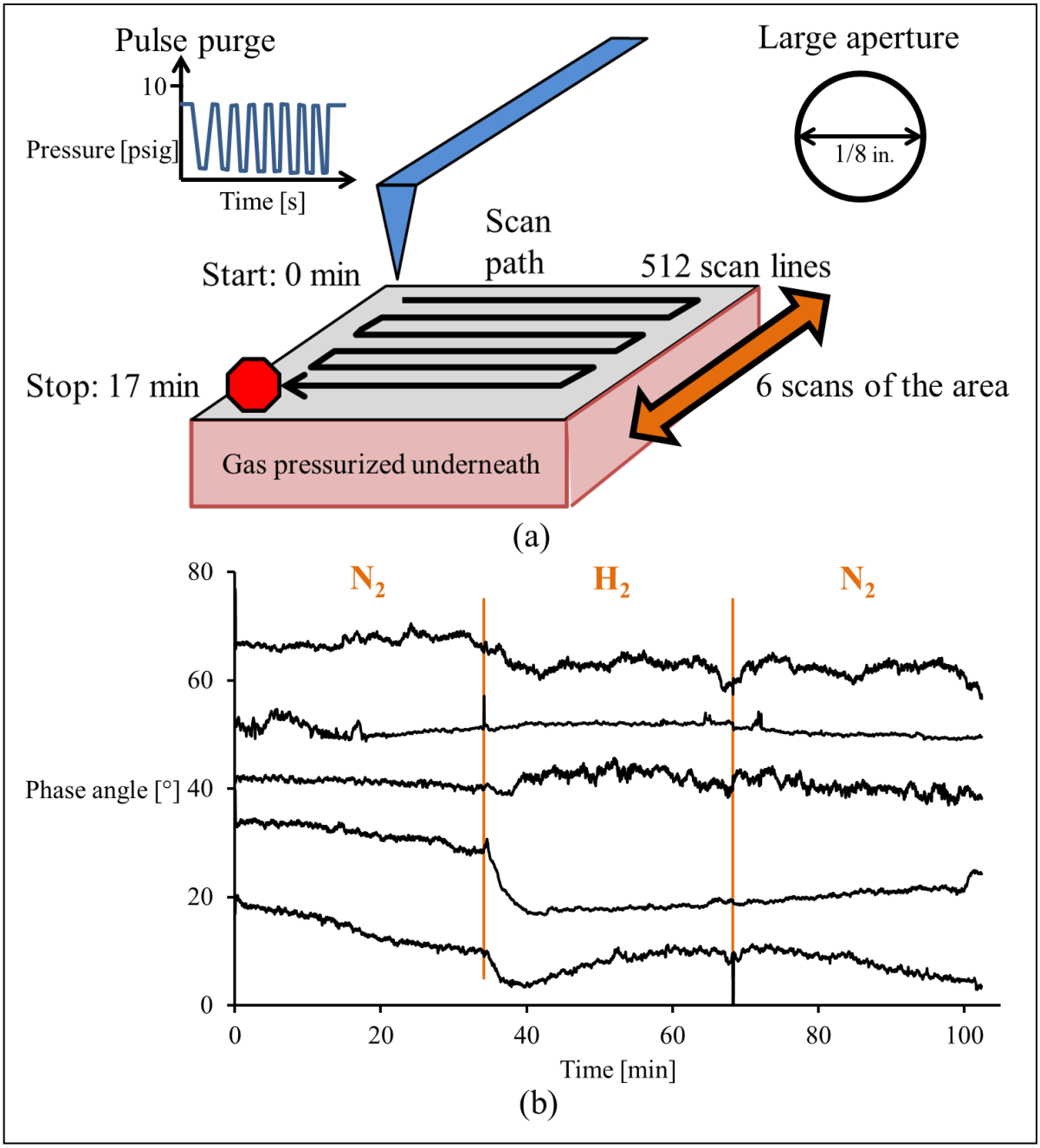

Figure 8.12 - Compiled phase-angle results of hydrogen diffusion experiments conducted with PC films (l = 0.010 in.) sputtered with Pd for 45 s.

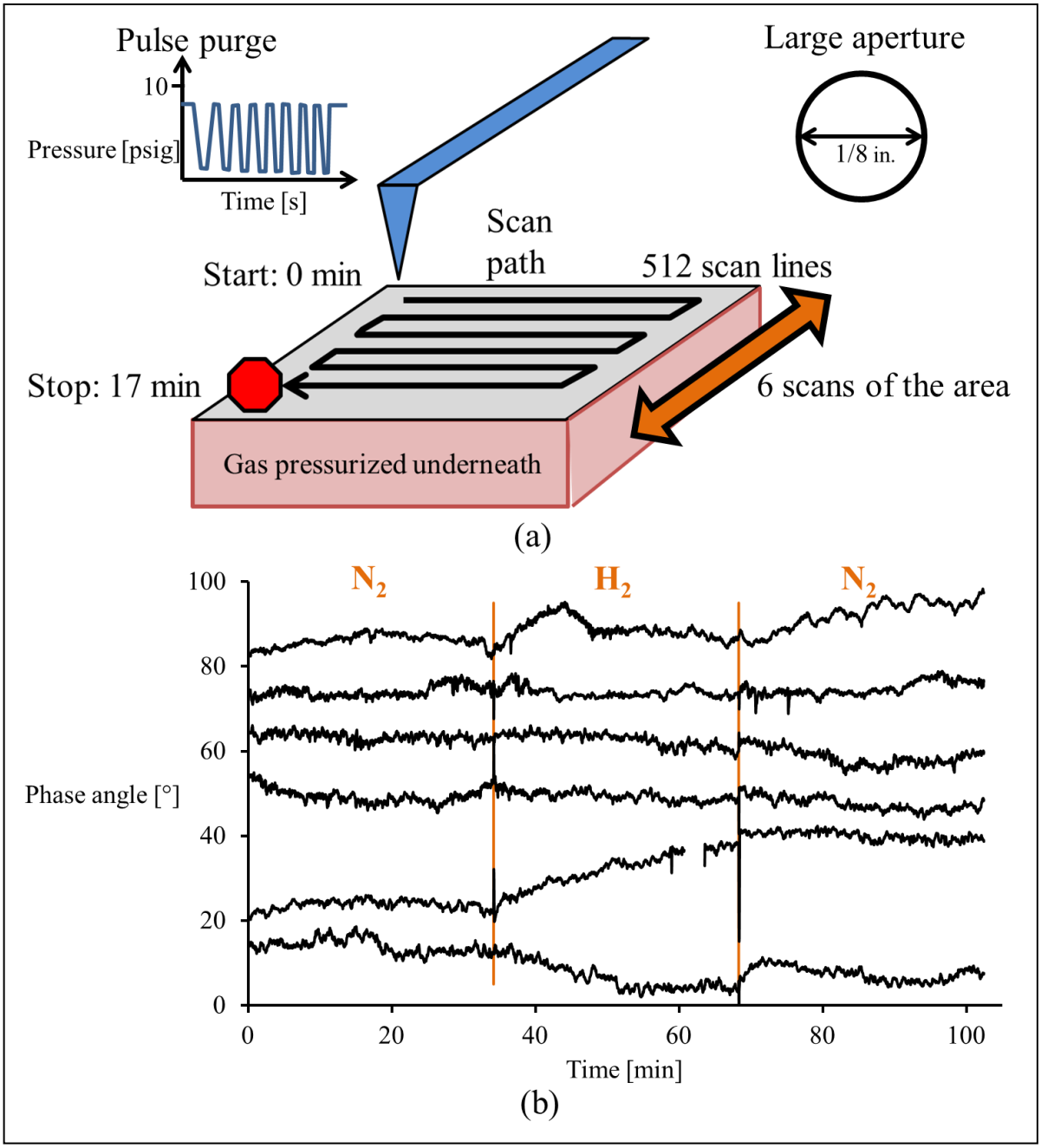

Figure 8.13 - Compiled phase-angle results of hydrogen diffusion experiments conducted with PC films (l = 0.010 in.) sputtered with Pd for 45 s.

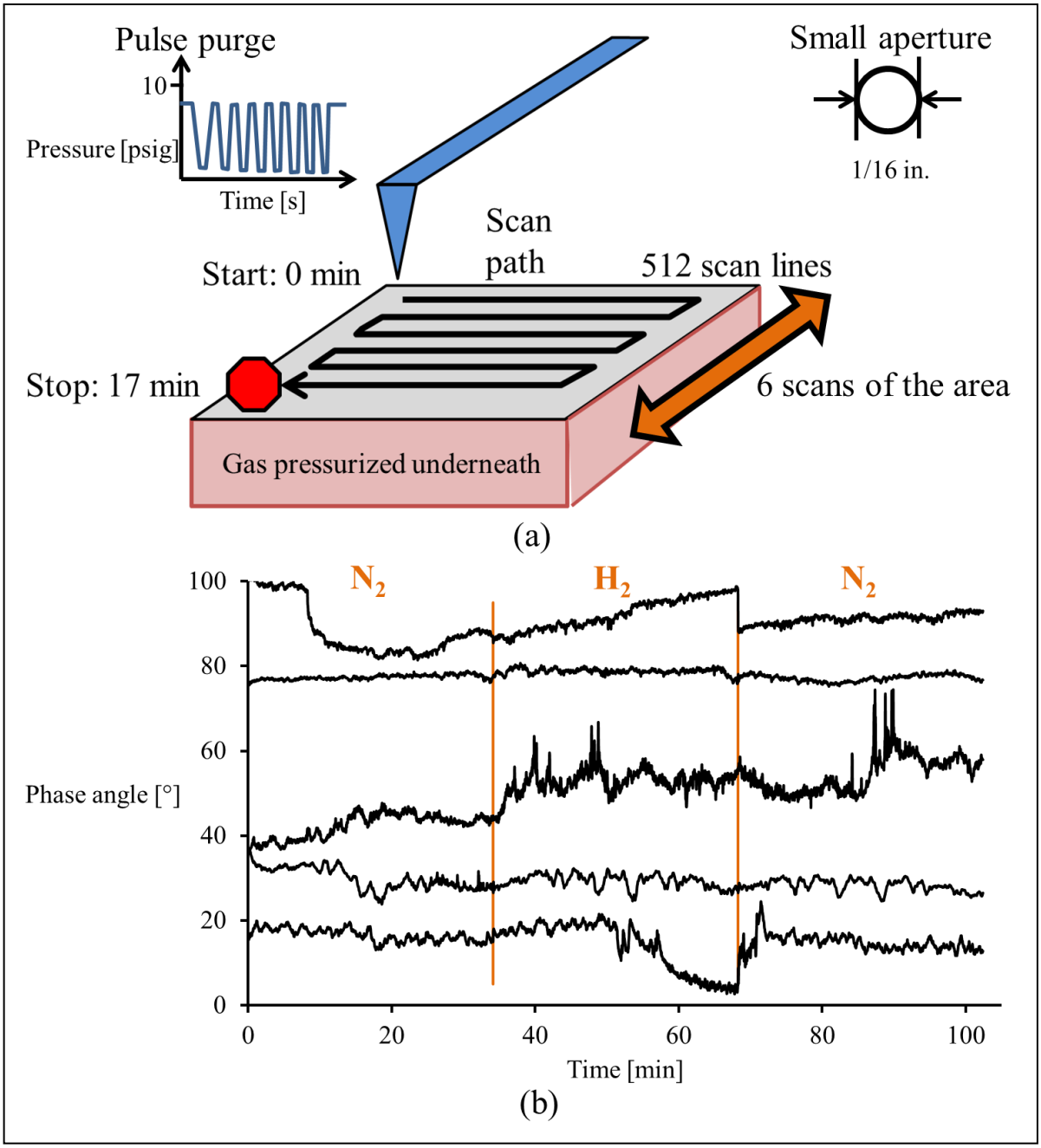

Figure 8.14 - Compiled phase-angle results of hydrogen diffusion experiments conducted with PC films (l = 0.010 in.) sputtered with Pd for 45 s.

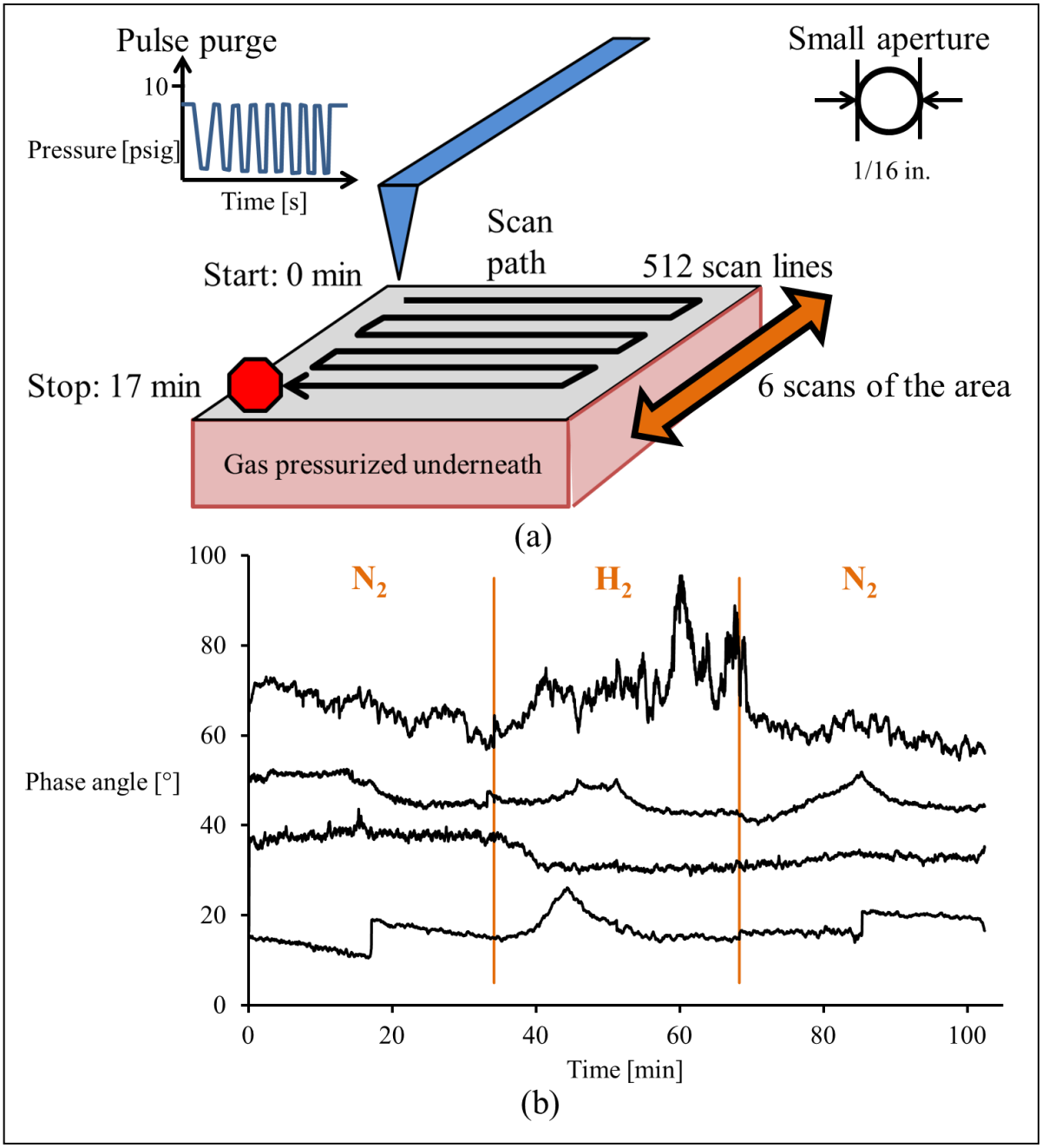

Figure 8.15 - Compiled phase-angle results of hydrogen diffusion experiments conducted with PC films (l = 0.010 in.) sputtered with Pd for 45 s.

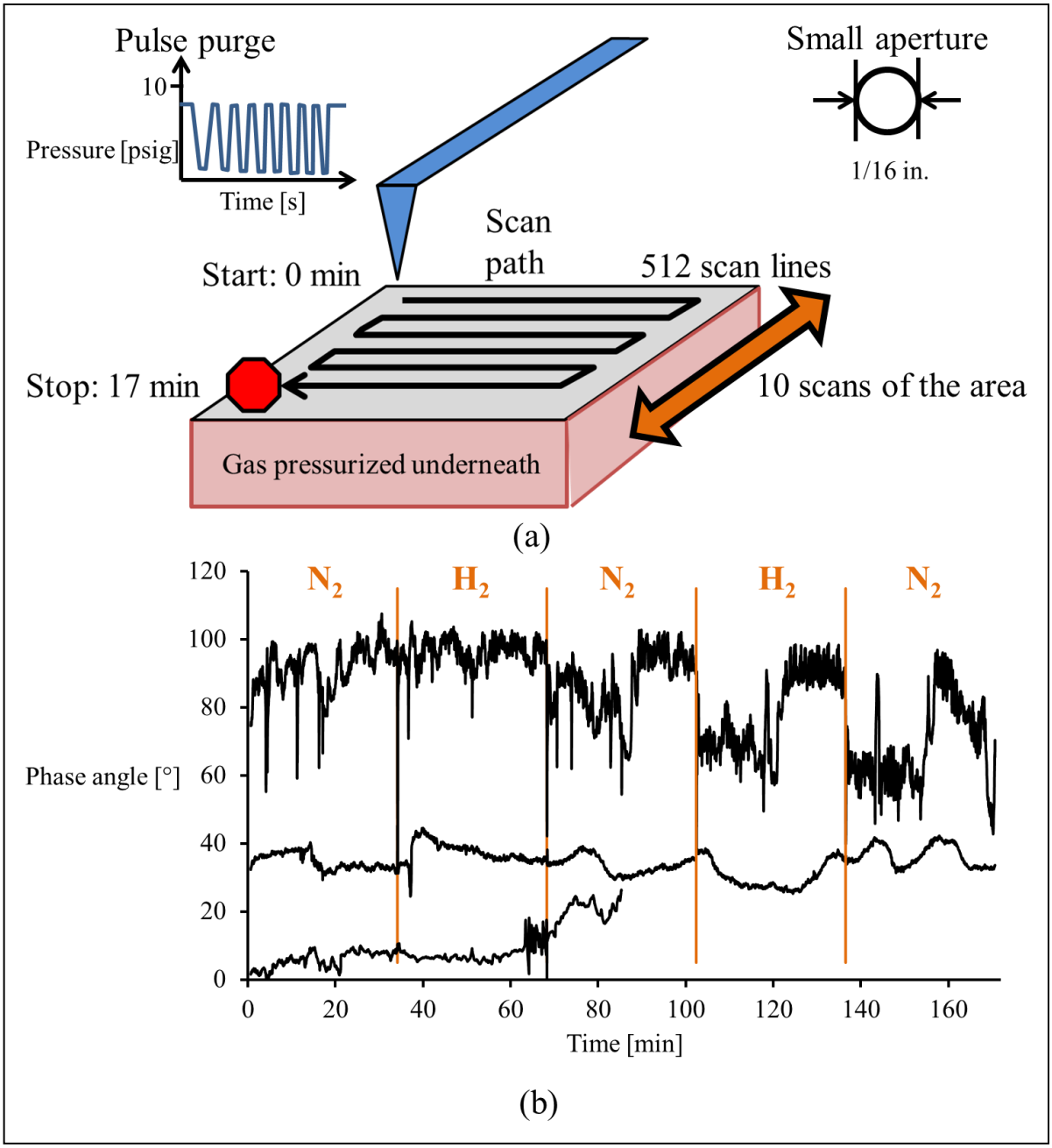

Figure 8.16 - Compiled phase-angle results of hydrogen diffusion experiments conducted with unmodified PC films (l = 0.010 in.)

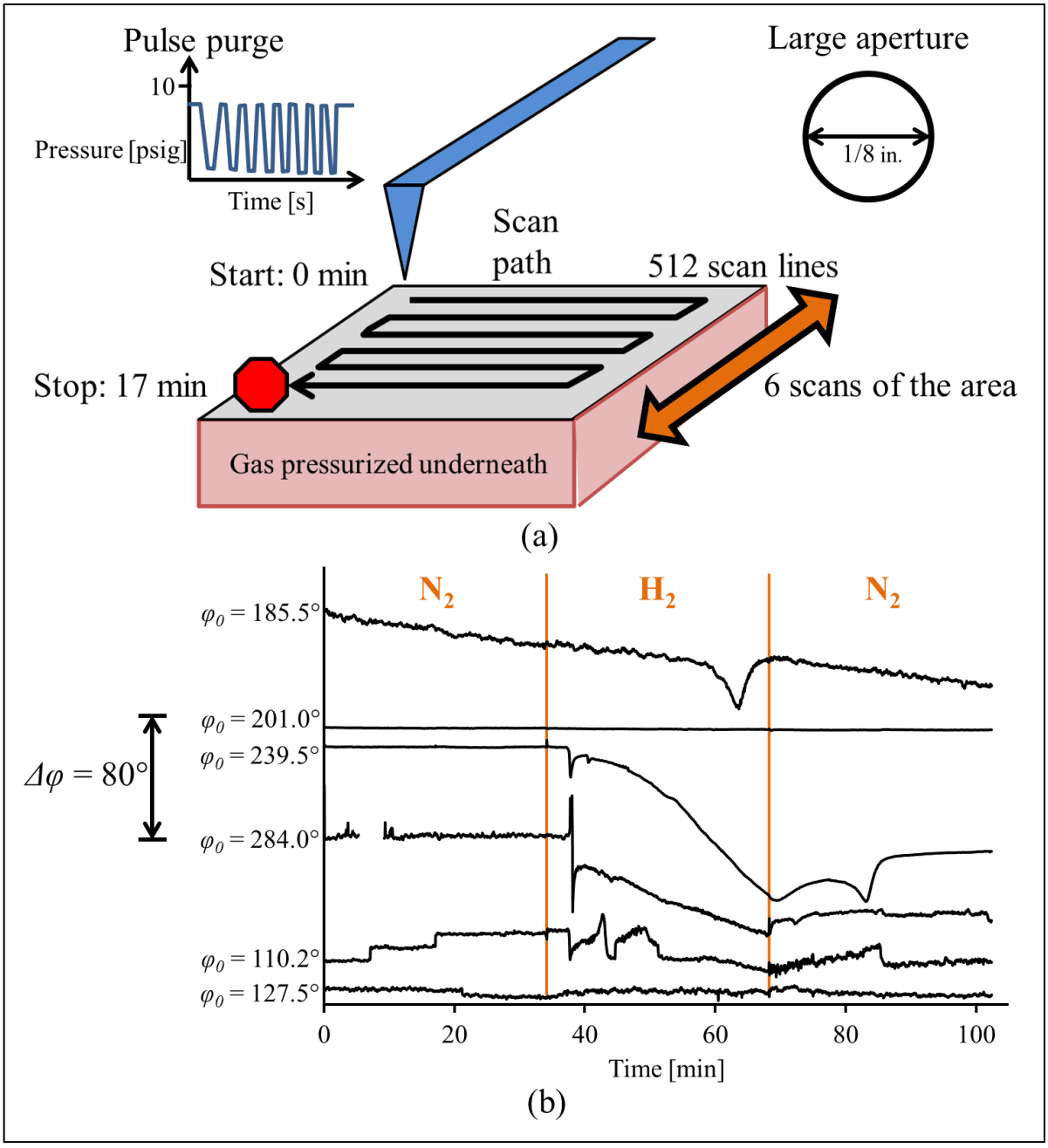

Figure 8.17 - Compiled phase-angle results of hydrogen diffusion experiments conducted with unmodified PC films (l = 0.010 in.).

8.3 Appendix C – Integrally Skinned Asymmetric Polyetherimide Membrane Production, Testing, and Treatment by Plasma Sputter Coating

Production of Integral Asymmetric Polyetherimide Membranes

The identities and amounts of components used to produce approximately 285 mL of polyetherimide (PEI) solution are shown in Table 2. This is based on solution A from a method produced and patented by Peinemann.[3]

Table 2 - The components of the PEI solution used to make integrally skinned asymmetric PEI membranes.

Compound	Amount	Purpose
para-xylene	69.6 mL	Non-solvent/swelling agent
dichloromethane	139.6 mL	Solvent
acetic acid	23.0 mL	Pore-forming agent
1,1,2,2-tetrachloroethane	10.2 mL	Solvent
PEI	54.06 g	Polymer matrix

These materials are added to a glass jar in the order they are shown. They are stirred with a magnetic stir bar until the polymer beads have been dissolved completely.

For the casting process, float-glass plates with dimensions of 8.5 in. by 11 in. are used. An adjustable casting knife with a gap thickness of 350 μm is used. With the casting knife at one end of the glass plate, polymer solution is poured out in a line in front of the knife. The knife is then drawn over the glass plate to create an even sheet of polymer. The glass plate with the polymer sheet is then immersed in a bath of acetone. The membrane sheets are kept in the acetone bath for a minimum of 30 minutes. The membrane sheets are then removed from the acetone bath and the glass plate and allowed to dry for 24 hr in ambient air.

Testing the membranes consists of measuring the fluxes of hydrogen and nitrogen and calculating the ideal hydrogen-nitrogen selectivity, $\alpha_{H2/N2}$. Permeances are usually expressed in gas permeation units (GPU). One GPU equals 1×10^{-6} $cm^3(STP)cm^{-2}s^{-1}cmHg^{-1}$.

[3] Peinemann, K.-V. Method for Producing an Integral Asymmetric Membrane and the Resultant Membrane. U.S. Patent 4,673,418, June 16, 1987.

Fluxes are calculated using the following equation.

$$P/\ell\,[GPU] = \frac{\Delta V}{\Delta P \times A_{membrane} \times \Delta t} \times 10^6 \qquad \text{Equation 8.1}$$

Where: P/ℓ ≡ permeance in GPU

ΔV ≡ Ideal gas volume that permeates the membrane

P_{feed} ≡ Pressure upstream of the membrane

$A_{membrane}$ ≡ Area of the membrane available for flux

Δt ≡ Time interval of flux

Hydrogen permeances and ideal hydrogen-nitrogen selectivities for membranes produced using the above method are shown in Figure 8.18.

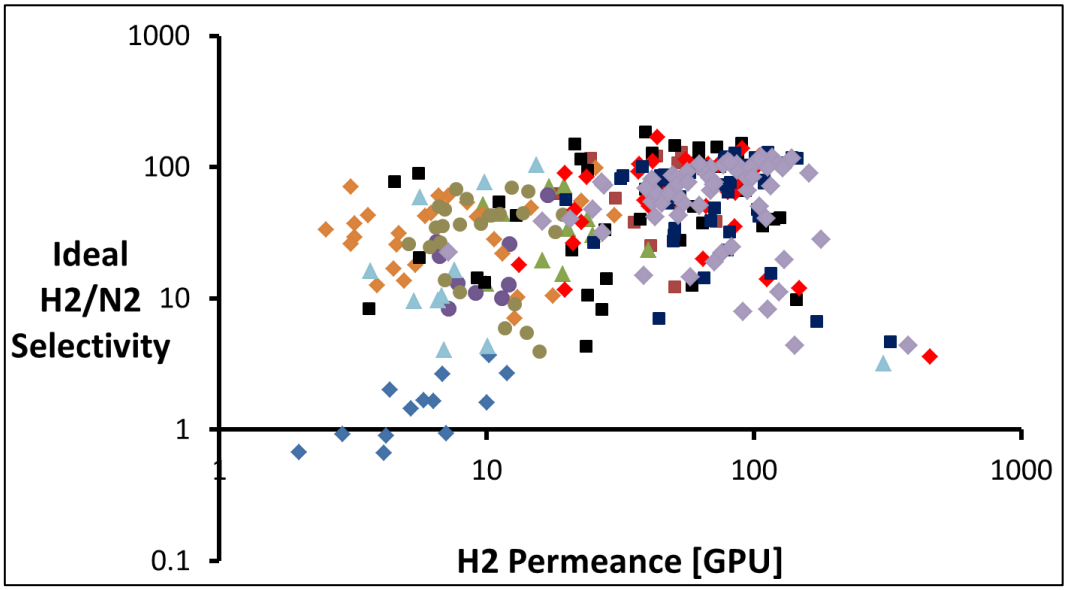

Figure 8.18 - Hydrogen permeances vs. ideal H_2/N_2 selectivities of PEI membranes produced by the author. The performance data of membranes produced from the same polyetherimide solution are represented by the same symbol.

PEI membranes were often sputter-coated with Pd using a DESK II magnetron sputter coater (Denton Vacuum, Moorestown, NJ) for 9 s with a current of 45 mA in a 100 mTorr ambient air atmosphere for use in catalytic membrane reactors. This was to deposit an imperfect layer of Pd

on the selective skin of the membrane. The sputtering process always caused a decrease in the hydrogen permeance and ideal hydrogen-nitrogen selectivity of the membrane as shown in Figure 8.19.

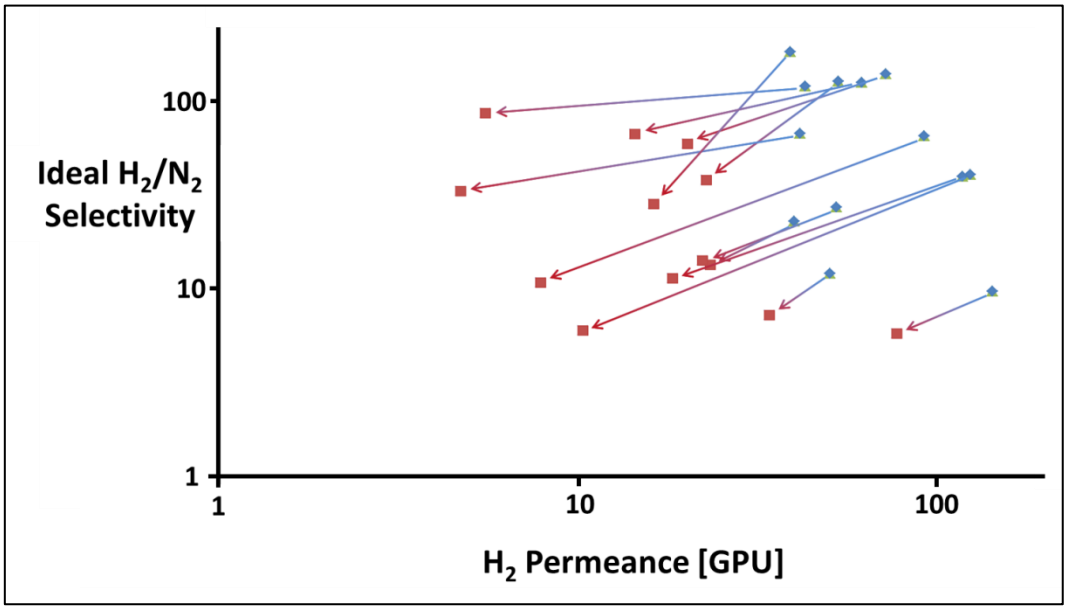

Figure 8.19 - Hydrogen permeances vs. ideal H_2/N_2 selectivities of polyetherimide membranes produced by the author before (blue diamond) and after (red square) treatment by sputter coating with Pd in 100 mTorr ambient air with a current of 45 mA for 9 s.